Thesis Report

Detection of Icy Particles in the Experimental Research on Enceladus' Plumes

Delft University of Technology
Keiya Iwamida

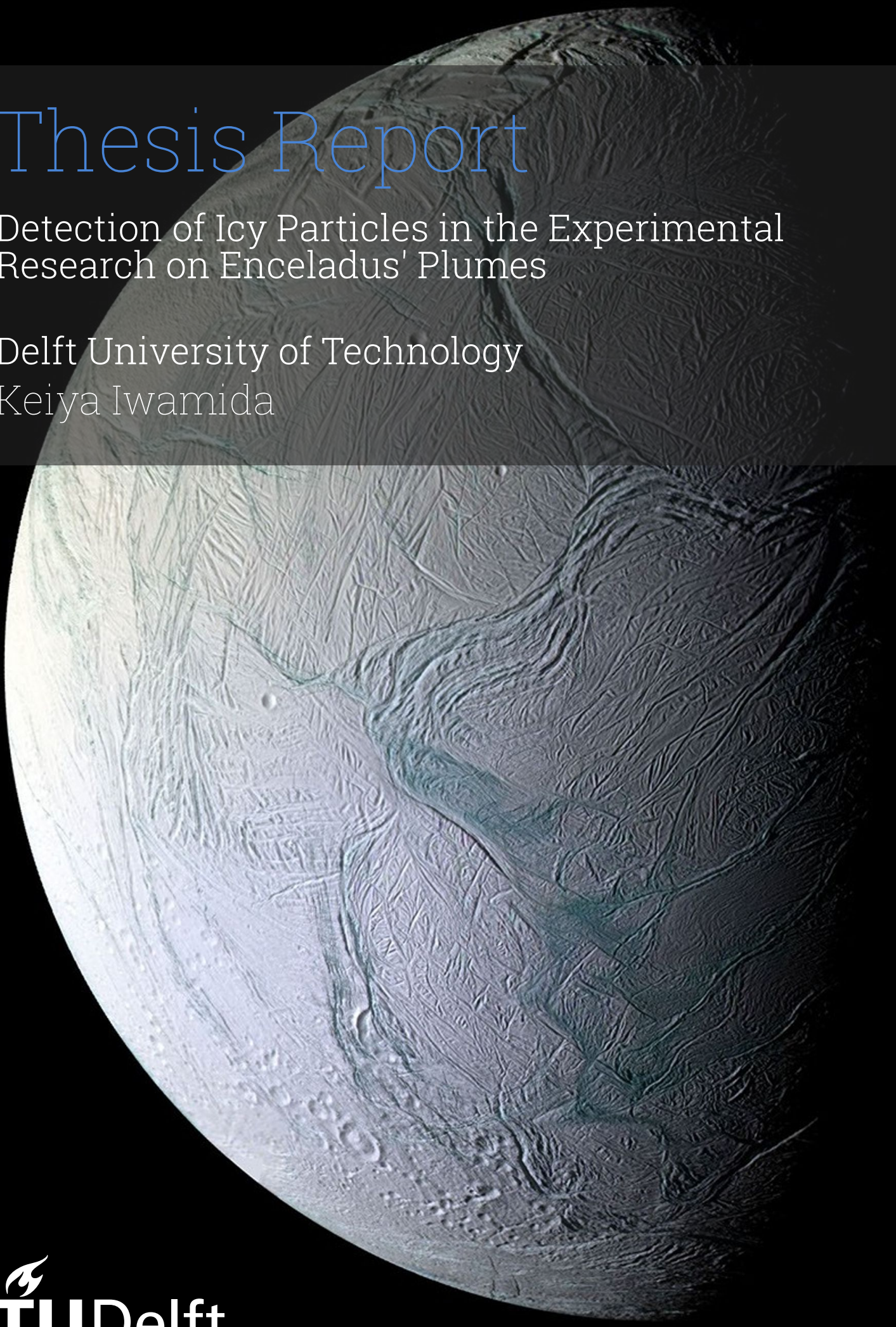

Delft University of Technology

TU Delft

Thesis Report

Detection of Icy Particles in the Experimental Research on Enceladus' Plumes

by

Keiya Iwamida

Student Number: 4773047
Instructor: Dr. S.M. Cazaux
Faculty: Faculty of Aerospace Engineering

Cover: NASA/JPL/Space Science Institute
Style: TU Delft Report Style, with modifications by Daan Zwaneveld

TU Delft

Preface

As I wrap up my time in TU Delft as a student, I would like to express my sincere gratitude for those who have supported me on this journey. First and foremost, I would like to thank Stéphanie and Yaël for their supervision and incredible support in making this thesis project possible. They have taught me everything essential in making this master's thesis a success, from the theoretical aspects of Enceladus to the presentation of complex technical information to an audience. I would also like to mention Sebastian for his help in the computational simulation of the plume models, as well as other members of the Plumes group for their insights into our common research topic from different perspectives. With the master's thesis being a rather solitary adventure in contrast to group projects done in the first year, the presence of my friends truly supported me in many ways; they gave me words of encouragement during tough times, inspired me with their wisdom and motivated me to strive further and enhance my understanding into my own field of expertise. Finally, I cannot thank my family enough for their support, not only throughout this master's program, but throughout my whole academic career. Their support and effort are what brought me to where I am today. Completing this thesis and this master's program was a challenging journey, but I would like to make the best use of what I have learned here and continue to strive further as I start a new chapter in my life.

Keiya Iwamida
Delft, July 2025

Abstract

The Cassini mission discovered the existence of plumes on the surface of Enceladus. These plumes have been recreated in a laboratory to experimentally investigate the properties of the plumes. This research project focuses on the detection of solid ice particles ejected from an experimental model of the Plumes of Enceladus. The research begins by establishing a baseline experiment in which the detection technique is to be applied. The results from the preliminary investigation, including both the experimental and simulation models, indicate several possibilities of nucleation occurring within the channel. The concept generation phase yielded two general detection principles to be assessed for trade-off analysis: optical methods and impulse-based methods. As a result of the trade-off, an impulse-based method using piezoelectric sensor – a method based on the measurement of impulse caused by the impact of solid particles onto the sensor surface – was selected to be the most appropriate technique for this application. To test the selected detection method, the test campaign was conducted in two phases: drop test and plume model test. The drop test was conducted to investigate the response of the sensor using grains of known masses and variable drop height. A linear relationship between the grain impulse and the voltage response was identified, and this result allowed the impulse of an incident particle to be extrapolated given a voltage response. The second phase of the test campaign integrated the detection system into the plume mode in the vacuum chamber. Several waveforms were detected throughout the experiment: damped wave, attributed to solid particles ejected from the model, turbulent wave, attributed to an unsteady flow of vapor during the initial boiling phase, and low-amplitude periodic waves, attributed to a flock of small particles ejected from the plume model. These results indicate the presence of solid particles in the plume model, and given a particle velocity, the particle size may be determined. A noise analysis of the sensor in the plume model was performed, yielding a plot of the minimum detectable particle size to the particle velocity.

Contents

List of Figures

List of Tables

Nomenclature

Abbreviations

Abbreviation	Definition
CAT	Chemical Analyzer Target
CIRS	Composite Infrared Spectrometer
CCD	Charge-coupled device
CDA	Cosmic Dust Analyzer
DA	Dust Analyzer
DC	Direct Current
EG	Entrance Grid
ESA	European Space Agency
EUV	Extreme Ultraviolet
FIR	Far-infrared
FUV	Far Ultraviolet
FP	Focal plane
HDAC	Hydrogen-Deuterium Absorption Cell
HRD	High-Rate Detectors
HSP	High-Speed Photometer
IIT	Impact Ionization Target
INMS	Ion and Neutral Mass Spectrometer
ISS	Imaging Science Subsystem
MIR	Mid-infrared
NASA	National Aeronautics and Space Administration
PISCES	Plumes and Ices Simulation Chamber for Enceladus and other moonS
PLA	Polylactic acid
RF	Radio Frequency
RQ	Research question
SPT	South Polar Terrain
UVIS	Ultraviolet Imaging Spectrograph
VIMS	Visible and Infrared Mapping Spectrometer
WP	Work package

Symbols

Symbol	Definition	Unit
a	Acceleration	$[m/s^2]$
A	Cross sectional area of channel	$[m^2]$
b	Cantilever beam width	[m]
c_p	Specific heat capacity	[J/K/kg]
$c_{p,inlet}$	Specific heat capacity at inlet	[J/K/kg]
$c_{p,vent}$	Specific heat capacity at vent	[J/K/kg]
d	Droplet diameter	[m]
E	Young's modulus	[Pa]
f	Solid fraction	[-]
F	Cantilever beam load	[N]

Symbol	Definition	Unit
$F_{i,solid}$	Force attributed to an individual solid particle	[N]
F_{solid}	Total force attributed to solid particles	[N]
F_{vapor}	Force attributed to vapor flow	[N]
h	Specific enthalpy	[J]
h_b	Cantilever beam height	[m]
Δh	Enthalpy change	[J]
J	Impulse	[Ns]
Kn	Knudsen number	[-]
L	Cantilever beam length	[m]
L_v	Latent heat of fusion	[J/kg]
$\dot{m}_{solid}$	Mass flow of solid particles	[kg/s]
$\dot{m}_{vapor}$	Mass flow of vapor flow	[kg/s]
m	Mass	[kg]
M	Mach number	[-]
n_{solid}	Number of solid particle ejected per time	[/s]
N	Number of solid particle ejected per mass	[/kg]
p	Static pressure	[Pa]
p_{eq}	Saturated vapor pressure	[Pa]
p_{gas}	Vapor pressure	[Pa]
p_0	Total pressure	[Pa]
P	Flow pressure	[Pa]
P_{static}	Static pressure	[Pa]
P_{dif}	Differential pressure	[Pa]
$P_{chamber}$	Chamber pressure	[Pa]
P_{mbar}	Converted chamber pressure	[mbar]
P_{res}	Reservoir pressure	[Pa]
r	Particle radius	[m]
R_{sp}	Specific gas constant	[J/kg/K]
S	Saturation degree	[-]
t_0	Start time of temperature and pressure data	[s]
Δt	Contact time	[s]
T	Temperature	[K]
T_{flow}	Flow temperature	[K]
T_{inlet}	Inlet temperature	[K]
T_{res}	Reservoir temperature	[K]
T_{vent}	Vent temperature	[K]
u	Initial velocity	[m/s]
V	Flow velocity	[m/s]
V_{max}	Maximum voltage amplitude	[mV]
V_{out}	Pressure sensor output voltage	[V]
V_{max}	Peak-to-peak voltage amplitude	[mV]
V_{solid}	Solid particle velocity	[m/s]
V_{vapor}	Vapor flow velocity	[m/s]
V_{vent}	Flow velocity at vent	[m/s]
We	Weber number	[-]
γ	Heat capacity ratio	[-]
ϵ	Strain	[-]
ρ	Density	[kg/m^3]
ρ_{ice}	Ice density	[kg/m^3]
σ	Surface tension	[N/m]

1

Introduction

As the second-largest planet in the solar system, Saturn has a significant number of natural satellites. Among them, Enceladus is the sixth largest, measuring about 498 km in diameter and orbiting roughly 240,000 km from Saturn with a period of about 33 hours (Schubert et al., 2007). Due to the presence of key elements necessary for life, Enceladus is considered a candidate for harboring life, which has led to heightened scientific interest. Both the Voyager missions and the Cassini spacecraft have observed Enceladus, with Cassini providing particularly detailed insights.

The moon's south pole displays elevated temperatures and contains traces of water and ice particles (Spencer et al., 2006). Distinctive tectonic structures known as "tiger stripes" — linear depressions about 130 km long, 500 m deep, and 2 km wide — are in this region (Porco et al., 2006). Cassini detected vapor plumes emanating from these stripes, pointing to the existence of a global subsurface ocean (Porco et al., 2006) (Thomas et al., 2016). These plumes are believed to feed Saturn's E-ring (Showalter et al., 1991). The composition of the ejected material indicates contact between the liquid water and Enceladus' rocky core (Waite et al., 2009). It is theorized that the heat driving these features comes from tidal dissipation — the friction from tidal forces deforming the moon's core — which generates thermal energy that fuels its geological activity (Porco et al., 2006).

In addition to theoretical modeling of these plumes, experimental approaches have been employed to better understand the phenomenon. Sklavenitis, 2021 recreated an analog of the Enceladus plume in a vacuum chamber using a plexiglass setup with a reservoir and nozzle. The reservoir, filled with liquid water to mimic the underground ocean, released vapor through the nozzle when pressure in the chamber was reduced, simulating surface fissures. Visual monitoring through chamber windows and the use of tracer particles allowed observation of the vapor flow. Giordano, 2023 conducted similar experiments, focusing on the effect of temperature on flow behavior. The study found that wall temperature significantly affects the flow's thermal properties due to convective and radiative heat transfer.

Cassini has also observed solid particles being ejected from the plumes of Enceladus, revealing some key information about the internal structure of Enceladus. Likewise, the detection of solid particles from the experimental plume model is crucial to creating the analog of the plumes. This thesis project addresses the creation and detection of solid particles in the experimental plume model. The following research question was formulated.

How can the plume's ejecta from an icy moon's subsurface ocean be visualized, and what can these reveal about the origin of the plumes?

The main research question can be further divided into several sub-questions.

1. How can Enceladus' plumes and the flow of gas and icy particles be recreated in a laboratory?
2. What is the ideal method to visualize plume ejecta from an icy moon?
3. What can be concluded from the grain velocities and sizes measured using the selected detection technology?

The first sub-question is addressed to establish a baseline experiment in which a consistent plume with solid particles is generated. The second sub-question is addressed to conduct a trade-off between various methods to detect solid particles in the plume model. The third sub-question addresses the findings from the implementation of the selected detection method.

This report is structured as follows. Chapter 2 serves as a literature review, addressing the current progress into the research of Enceladus, including a brief introduction on the Saturnian system, an overview of the observations made by the instruments onboard Cassini and an elaboration on the current theoretical and experimental research of the plumes on Enceladus. Chapter 3 introduces the planning of this research, including a breakdown of the research question as well as the work packages correlated to each sub-question. Chapter 4 provides the details on the plume model that is used in this experimental research as well as its test environment and the measurement equipment. Chapter 5 elaborates on the results of the initial particle generation experiments aimed to create solid particles in the experimental model. Chapter 6 presents the trade-off conducted to select the ideal detection method for the purpose of the research question. Chapter 7 presents the results of the implemented detection method. Chapter 8 concludes on the findings from this research project and provides recommendations for future research into this topic.

2

Literature Review

This chapter serves as an introduction into the plumes of Enceladus as well as the current advancements of the research into Enceladus.

2.1. The Saturnian System

With Saturn being the second-largest planet in the solar system, it is known to host a large number of satellites. The Saturnian system has at least 146 confirmed satellites as of September 2024 (Sheppard et al., 2023), and the characteristics of these moons such as its size and geological features have extensive variation. Saturn's rings is composed of water ice particles, and are split into subdivisions. Rings A, B and C are known as the main rings and are the densest part of the system of rings. The rest of the ring system, namely D, E, F and G rings are known as the tenuous dusty rings. The material of the E rings was determined to be supplied from the plumes on Enceladus. An analysis of the E ring showed a density peak at the location of Enceladus' orbit, with a difference in the radial direction of less than 3000 km (Showalter et al., 1991). The vertical thickness increases with distance from the Saturn, ranging from 6000 km at its inner bound to nearly 40000 km at its outer bound.

2.2. Enceladus

Enceladus is the sixth-largest moon of Saturn with a diameter of 498 km. It is situated approximately 240,000 km away from Saturn with an orbit period of approximately 33 hours (Schubert et al., 2007). It is a moon with a possibility to host lifeforms as it possesses many ingredients that are essential to support life. This has fueled great interest and research into this moon. It has been visited by the Voyager spacecrafts and the Cassini spacecraft for observations. The latter has made extensive progress into what is known about this moon. This section will highlight the findings on Enceladus, with respect to its internal structure and the surface characteristics.

2.2.1. Internal Structure of Enceladus

Heat mechanism

Enceladus is characterized as one of the most geologically dynamic bodies in the solar system, as derived from the data retrieved by the Cassini spacecraft. Enceladus is currently thought to be a differentiated body with a large rock-metal core of radius ranging from 150 km to 170 km (Schubert et al., 2007). The research before Cassini mission suggested that the estimated density implied a composition consisting mostly of water ice (Campell and Anderson, 1989) (Peale, 1999). This core is likely surrounded by a liquid water - ice shell.

Plumes on Enceladus

Assuming a hydrostatic equilibrium, it was determined that Enceladus' shape is inconsistent with a fully differentiated body (Porco et al., 2006). The south polar region of the satellite has shown higher temperatures as well as traces of water and ice particles (Spencer et al., 2006). Plumes of vapor has been observed by the Cassini spacecraft, and evidence implies that the jets originate from a liquid

reservoir rather than from active melting (Porco et al., 2006) (Thomas et al., 2016). The E-ring of Saturn has been observed to originate from the plumes of Enceladus (Showalter et al., 1991). The salinity of the jets suggested that the liquid reservoir in which the droplets originate were in contact with a rocky core (Waite et al., 2009).

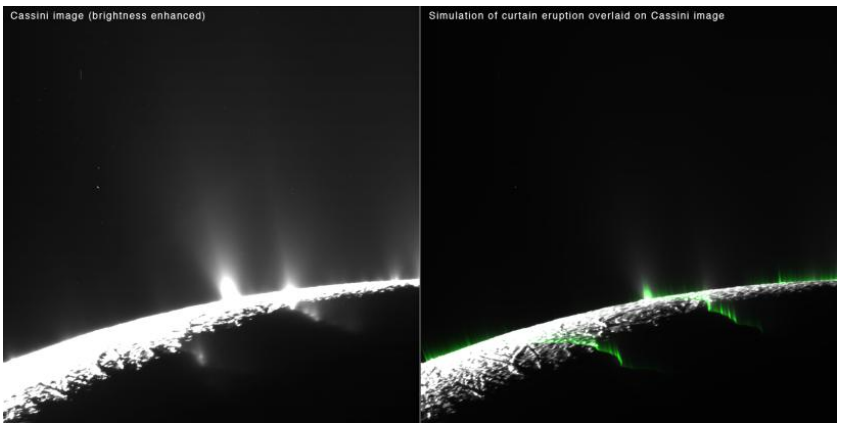

Figure 2.1: Plumes as observed by Cassini (Cassini Imaging Team, n.d.-a).

It has been suspected that the origin of the heat source is in tidal dissipation. Enceladus is in a 2:1 orbital resonance with Dione, in which Enceladus completes two orbits around Saturn while Dione completes one. As a result of this resonance, the orbital eccentricity of Enceladus is forced to be 0.0047 (Porco et al., 2006). This eccentricity results in tidal deformation of Enceladus, and the heat that is produced from the friction of the core's deformation is thought to be what powers the geological activities (Porco et al., 2006). Before the Cassini mission, it was suspected that radioactive decay was the origin of the heat within Enceladus, however it has been concluded that while it may have been a major heat source in the earlier phase of the moon's life, it would not have contributed to the present-day's energy budget (Efroimsky, 2018).

While the subsurface environment of Enceladus is not directly observable, the initial question arising with the observation of plumes is whether if the subsurface reservoir is a localized polar sea or a global ocean. The gravity models of Enceladus showed consistency with a mass anomaly at southern latitudes, and this initially suggested that there is at least a regional subsurface sea (Thomas et al., 2016). Further interpretation of the gravity data then suggested a possibility of a global subsurface ocean (Thomas et al., 2016). Ultimately, it was determined that the physical liberation of Enceladus is too large for a rigid connection between the core and the crust (Thomas et al., 2016). Hence the source of water in the south pole was determined to be part of a global ocean.

Porosity of the core

The porosity of Enceladus' core may be implied through its inferred density. Enceladus' core is considered to be porous with the pores filled with water (Rovira-Navarro et al., 2022). The porosity enables a more significant tidal dissipation that would cause the hydrothermal activities. Moreover, the permeability of the core allows for hydrothermal convection to transport heat (Czechowski, 2014). Several observations point towards a core of porous silicate matrix, in which water can permeate (Rovira-Navarro et al., 2022). Compared to the early life of Enceladus, the permeability and the porosity has decreased over time, nonetheless remains significant in the present days (Czechowski, 2014).

2.2.2. Surface of Enceladus

Age

The age of Enceladus' surface may be partly implied by the amount of craters that may be seen. Although there are some variations across the surface, there are several areas that are devoided of craters, suggesting a geologically young surface (Porco et al., 2006). This was especially the case in the southern polar region. In addition, a system of ridges, fractures and grooves have shown an indication of tectonic alteration, and some dark spots and pits indicate venting of subsurface volatiles (Porco

et al., 2006). Despite it being very trace, Enceladus also has an exosphere in which is concentrated towards the south polar region, comprising mostly of water vapor (Dougherty et al., 2006). This finding also points to a geologically active Enceladus as the gravity of Enceladus is too weak to maintain a sputtered atmosphere, in which photolized atmosphere particles are carried with solar wind.

Crystallinity

The crystallinity of the water ice is indicative of the process occurring on the surface. When water is condensed from vapor to solid below 150 K, amorphous ice forms. When this amorphous ice is heated to 150 K, it converts to crystalline ice (Brown et al., 2006). This process is only reversible when the crystalline structure is disrupted by bombardment of high-energy particles or photons. An analysis of the photometric and spectral data from Cassini showed Enceladus to be mostly crystalline, especially at the tiger stripes, with amorphous signature in areas between the tiger stripes (Brown et al., 2006). This is another implication of geological activity. Amorphous ice may be produced through radiative bombardment, flash-freezing of cryovolcanic liquid or rapid condensation of water vapor on the surface.

Tiger stripes

Tiger stripes are tectonic features of linear depressions with lengths of about 130 km, depth of about 500 m and a width of about 2 km (Porco et al., 2006). Observed for the first time on a flyby of Enceladus on 14 July 2005, the stripes were found near the south pole and up to a latitude of $55°S$. This is visible towards the south pole region in Figure 2.2.

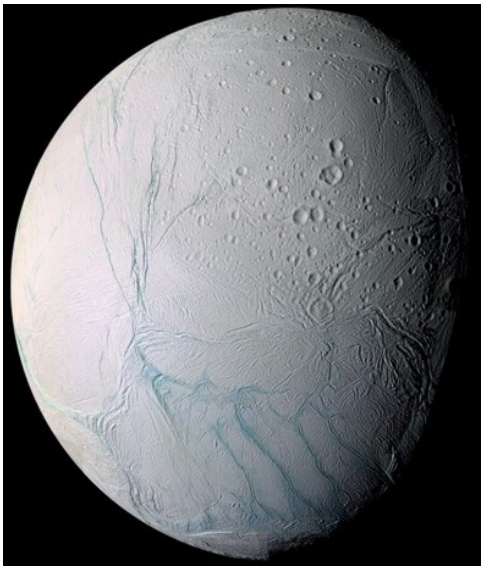

Figure 2.2: ISS image of Enceladus showing the tiger stripes in the south pole region (Cassini Imaging Team, n.d.-b).

Each stripes are separated by a distance of up to 35 km and generally have an orientation of 45 degrees offset from Saturn direction and usually terminating in hook-shaped bends (Porco et al., 2006). This is shown in Figure 2.3. The temperature corresponding to the region also showed higher values compared to other regions of the moon, as shown in Figure 2.4.

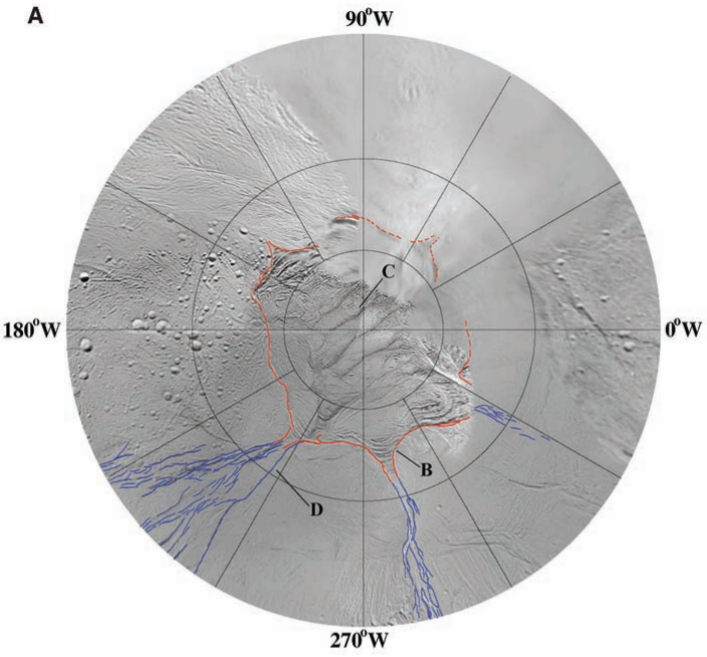

Figure 2.3: Polar stereographic basemap of the SPT covering latitudes from 0° to 90° S. The basemap also shows details obtained from the best ISS coverage of Enceladus' SPT to date. The circumpolar tectonic margin that encloses the SPT is marked as solid red lines where it is well resolved in high-resolution ISS images and as dashed red lines where it is interpreted from low-resolution coverage. Blue lines identify prominent, young tension fractures that extend from the Y-shaped discontinuities north to the equator (Porco et al., 2006).

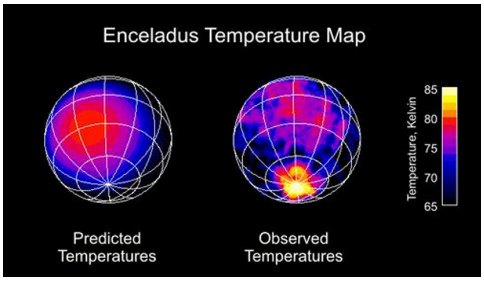

(a)

(b)

Figure 2.4: (a) temperature map of Enceladus. (b) temperature map of the tiger stripe region (Spencer et al., 2006).

Moreover, the plains in between the stripes are brighter by 10% compared to other parts of Enceladus

(Porco et al., 2006). This gives rise to implications for some geologic activity in this area, notably venting and particle fallout. It is thought that the age of this geological feature is young, mainly due to its sharp relief that cuts through other fractures in the path, in combination with its color and coarse grain size. The regolith layer, a blanket of loose, unconsolidated deposits, is absent in the tiger stripes (Porco et al., 2006). The regolith layer of Enceladus will be will be elaborated in 2.2.2.

Composition

The surface of Enceladus is mostly composed of nearly pure water ice, with the exception of the south pole region, in which light organics (e.g. methane, ethylene), carbon dioxide and amorphous and crystalline water ice are found (Postberg et al., 2018) (Brown et al., 2006). Other potential key substance such as carbon monoxide and ammonia were not detected. The grain sizes of the surface particles were observed to be more coarse in the southern region, indicative of geologic youth (Porco et al., 2006).

Regolith layer

Regolith is defined as loose, unconsolidated layer of deposits. In the case of Enceladus, the fall-back from plume eruptions accumulate on the surface as regolith layer (Porco et al., 2006). The pits as observed on Enceladus by Cassini is shown in Figure 2.5. The tectonic pit chains observed on the surface of Enceladus implies the existence of regolith, and its distribution gives some indication of the regolith's depths (Martin et al., 2023). A regolith layer of 700 m was determined by (Martin et al., 2023) with the use of Slope Angle Method, which makes use of the pit diameters and the sun angle at each pit. This is illustrated in Figure 2.6.

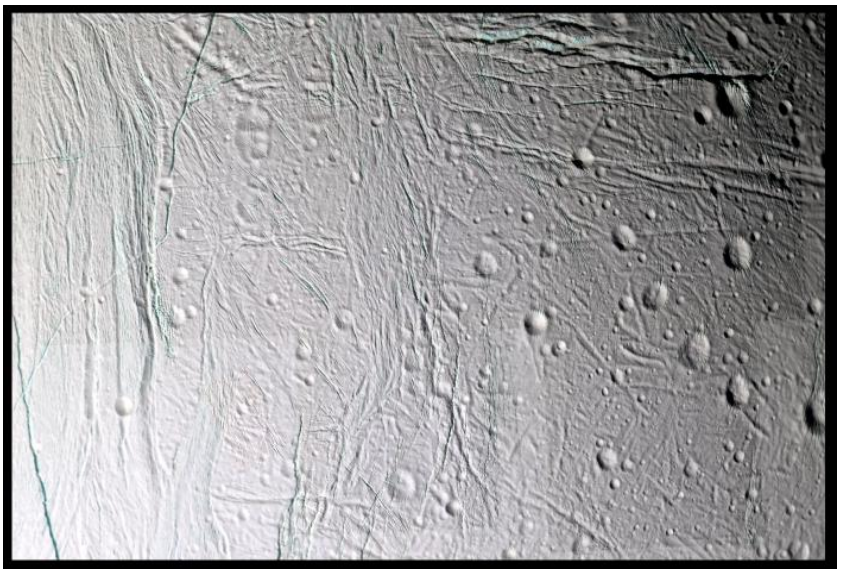

Figure 2.5: Pits as observed on Enceladus (NASA/JPL-Caltech, n.d.).

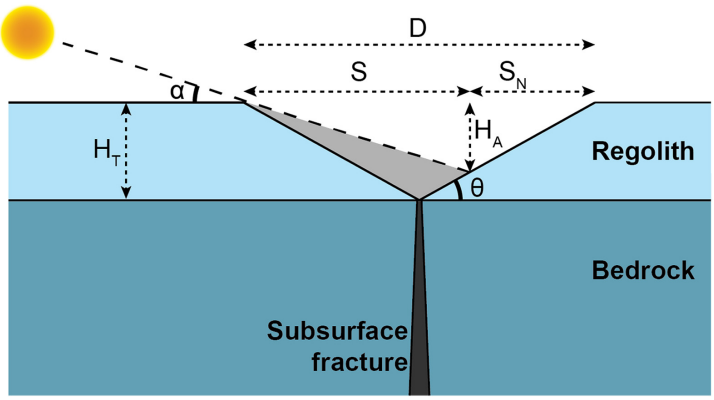

Figure 2.6: Schematic of the slope angle method (Martin et al., 2023).

The regolith thickness is represented in Figure 2.6 as H_T. In order to determine this thickness, pit diameter D, shadow length S, distance not in shadow S_N, and the sun angle α are needed. The sun angle is equal to the incidence angle subtracted from 90°. This technique can be modified to assume a slope angle of the pit θ, and use only the pit diameter to estimate regolith thickness.

As the porosity and the density of the regolith is unknown, (Martin et al., 2023) also explored different combinations of these parameters along with the deposition time. It was determined that only with a low density of $0.02 g/cm^3$ and a high porosity of 90% that it could reproduce the regolith thicknesses within the lifetime of Enceladus (Martin et al., 2023).

2.3. Cassini-Huygens Mission

Cassini-Huygens, commonly referred to as Cassini, was a mission to explore the Saturnian system as a joint effort between NASA and ESA. Launched in 1997, the spacecraft reached the Saturnian system in 2004 after multiple swing-bys around Venus, Earth and Jupiter. There have been a number of scientific research enabled by the Cassini mission, not only regarding Enceladus and Saturn but also insights into other satellites of Saturn such as Titan, Iapetus and Saturn's rings. This section describes the various instrumentation onboard Cassini.

2.3.1. Cosmic Dust Analyzer

The Cosmic Dust Analyzer (CDA) is a scientific instrument designed to detect and study dust particles with masses ranging from 10^{-19} kg to 10^{-9} kg (Srama et al., 2004). It measures various properties of these particles, including their electric charge, velocity, size, chemical composition, and direction of motion. The CDA is equipped with two types of sensor systems. The High-Rate Detectors (HRD), was specifically designed to investigate Saturn's rings by counting the number of dust particles encountered. These detectors utilize two separate polyvinylidene fluoride sensors. The Dust Analyzer (DA) provides detailed information about each particle's charge, speed, trajectory, mass, and chemical composition.

A technical drawing of the CDA is shown in Figure 2.7. The Entrance Grid (EG) system enables measurement of a particle's charge and velocity. The outermost and innermost grids are grounded, while the two intermediate grids are linked to a charge-sensitive amplifier. As a charged dust particle enters the CDA, it induces a signal in the amplifier corresponding to its electric charge. When the particle passes the first grid, the amplifier's output voltage rises. This voltage remains steady as the particle travels between the second and third grids, then decreases as it passes the third and approaches the fourth grid. By measuring the time it takes for the particle to traverse the known distance between the first and last grid, its velocity can be calculated. Additionally, because the two inner grids are tilted by 9 degrees, the path length between them varies with the particle's angle of entry, allowing for the determination of its flight direction.

Upon entering the CDA, particles may collide with either the Impact Ionization Target (IIT) or the Chemical Analyzer Target (CAT). These impacts generate fragments from both the particle and the target material, including neutral atoms, ions, and electrons. An electric field separates the resulting charged

particles, and charge-sensitive amplifiers measure the collected signals at the targets and grids.

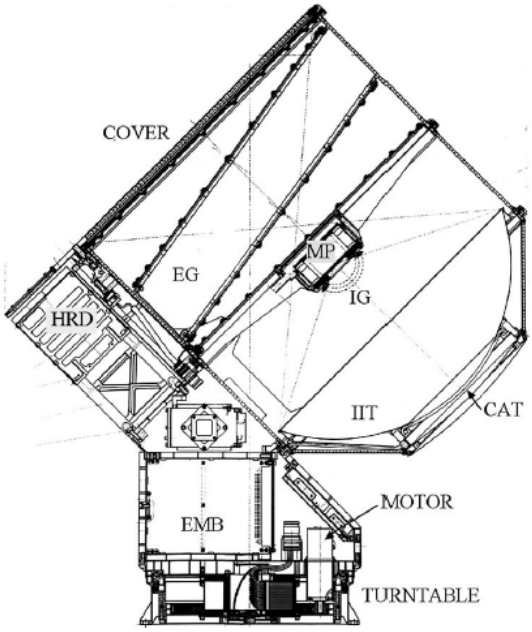

Figure 2.7: Technical drawing of the Cosmic Dust Analyzer (Srama et al., 2004).

The CDA has played a key role in discovering and characterizing the water plumes of Enceladus, including detecting organic compounds and evidence of hydrothermal activity, revealing the composition and origin of Saturn's rings, including the dynamic relationship between Enceladus and the E ring, studying interstellar dust, providing insights into particles from beyond the solar system, and measuring how micrometeoroids affect Saturn's rings and moons.

2.3.2. Ion and Neutral Mass Spectrometer

The Ion and Neutral Mass Spectrometer (INMS) is a quadrupole mass spectrometer designed to analyze the chemical, elemental, and isotopic composition of neutral gases and low-energy positive ions (Waite et al., 2004). Like the CDA, the INMS conducts in situ measurements, collecting data on the structure and composition of individual positive ions and neutral particles. It was used extensively to study the upper atmosphere of Titan and the magnetosphere of Saturn, as well as the ion and neutral particle environments around Saturn's rings and icy moons.

Mounted on the "Fields and Particles Platform" of the Cassini orbiter, the INMS was instrumental in measuring Titan's upper atmosphere above 950 km altitude and characterizing Saturn's inner magnetosphere. It analyzed the composition and structure of positive ions and neutral species during ring plane crossings and close flybys of icy moons. The instrument consists of several key components: an open ion source, a closed ion source, a quadrupole deflector and lens system, a quadrupole mass analyzer, and a dual detector system.

The open ion source generates ions by directly ionizing neutral gases in the ambient environment. It includes an ion trap/deflector that forms a directed ion beam, minimizing interactions between the ionized particles and the source surface. In contrast, the closed ion source also ionizes neutral gases but employs ram density enhancement — a method that increases measurement sensitivity and accuracy, especially for inert atomic and molecular species. This is achieved by directing a concentrated gas flow into an enclosed chamber, with an orifice controlling the gas outflow to maintain a high particle density.

Ion beams from either source are directed toward the mass analyzer using a 90-degree quadrupole deflector, which adjusts electrostatic potentials to sequentially switch between sources. Both beams then pass through a shared exit lens system into the quadrupole mass analyzer, which uses four precisely shaped hyperbolic rods. The mass-to-charge ratio, resolution, and ion throughput are controlled

by varying radio-frequency (RF) and direct-current (DC) electric fields between opposing rod pairs. Finally, the ions are detected and amplified using a dual detector system composed of two continuous dynode electron multipliers.

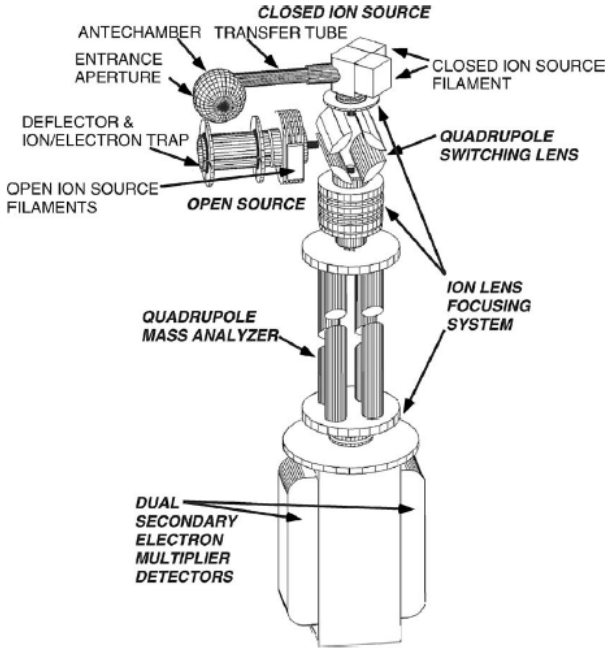

Figure 2.8: Schematic of the Ion and Neutral Mass Spectrometer (Waite et al., 2004).

The INMS played a pivotal role in understanding the chemical makeup of Saturn's system. Among its most significant findings were the discovery of water vapor plumes on Enceladus — suggesting a subsurface ocean that could harbor life — and the identification of complex organic molecules in Titan's atmosphere, offering valuable insight into its chemistry. The instrument also enhanced our understanding of Saturn's magnetospheric environment, particularly the plasma interactions with its rings and moons. During Cassini's Grand Finale, the INMS provided direct measurements of Saturn's upper atmosphere, yielding critical data about the gas giant's composition.

2.3.3. Composite Infrared Spectrometer

The Composite Infrared Spectrometer (CIRS) was designed to study infrared emissions from the atmospheres, surfaces, and rings within the Saturn system to determine their temperature and composition (Jennings et al., 2017). It utilizes dual interferometers and consists of two main assemblies: optics and electronics.

The optics assembly includes a telescope, a far-infrared (FIR) interferometer, a mid-infrared (MIR) interferometer, a reference interferometer, a moving scan mechanism, a cooler, thermal control components, an optics mount, protective covers, and a calibration shutter. The telescope itself uses a 50.8 cm paraboloid primary mirror and a hyperboloid secondary mirror, surrounded by a sunshade that also acts as a radiator. A cylindrical support tube extends from the primary mirror to the secondary, which has its own radiator.

CIRS collects scientific data using two of its three interferometers. Interferometers precisely measure wavelengths within the infrared spectrum. The FIR interferometer is a polarizing interferometer that uses substrate-mounted wire grid polarizers to polarize and modulate incoming radiation. Its moving mirror is mounted at one end of a shared scan mechanism. It uses roof mirrors and detects infrared signals via a matched pair of thermopile detectors with concentrators.

The MIR interferometer, a Michelson-type instrument, covers a spectral range of 600–1500 cm^{-1}. It mounts its moving mirror on the opposite end of the scan mechanism from the FIR. Cube corner mirrors are used, and the interferometer output is focused by a germanium lens onto focal planes FP3 and FP4.

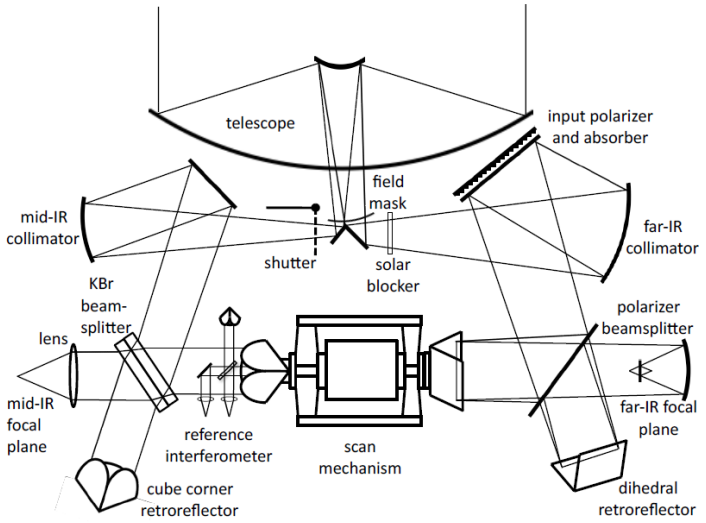

Figure 2.9: Conceptual diagram of the Composite Infrared Spectrometer (Jennings et al., 2017).

CIRS played a critical role in analyzing Saturn's thermal and chemical properties. It created detailed temperature maps, revealed atmospheric and surface compositions, and uncovered heat anomalies on Enceladus that hinted at subsurface oceans. This can be seen in Figure 2.4 Overall, CIRS helped to map the dynamic interplay between temperature, composition, and seasonal cycles across Saturn's system.

2.3.4. Imaging Science Subsystem

The Imaging Science Subsystem (ISS) served as Cassini's main imaging suite for capturing visual data of the Saturn system (ESA, 2019). It consisted of two digital cameras: a wide-angle camera for broad context views and a narrow-angle camera for high-resolution imaging of specific targets. Both cameras were sensitive to visible light and certain infrared and ultraviolet wavelengths. Each camera had multiple filter wheels to select specific wavelengths for scientific imaging. Figure 2.2 is an example of an image of Enceladus taken by the ISS.

The wide-angle camera used lenses to capture expansive scenes, such as Saturn with its ring system. The narrow-angle camera employed mirrors to focus on smaller features like moon craters or surface fractures. Both systems used charge-coupled devices (CCDs) to convert incoming light into digital images. The use of specific filters enabled researchers to target particular phenomena, such as the ultraviolet filters being employed to study high atmospheric hazes on Saturn and Titan, and infrared filters being employed to see through Titan's atmospheric haze and observe its surface.

ISS contributed to mapping Saturn's moons, monitoring weather patterns, analyzing ring structures, and capturing events like Enceladus's plumes and seasonal shifts on Titan. It was also instrumental in documenting Cassini's dramatic final descent into Saturn.

2.3.5. Visible and Infrared Mapping Spectrometer

The Visible and Infrared Mapping Spectrometer (VIMS) was used to analyze the composition and temperature of atmospheres, rings, and surfaces throughout the Saturn system (Brown et al., 2005). This imaging spectrometer separated light into different wavelengths, enabling identification of materials based on their reflected or emitted light across the 0.3 to 5.1 μm range.

VIMS included two channels. VIMS-VIS (Visible) operates from 0.30 to 1.05 μm, with 1.46 nm spectral resolution and 167 μrad spatial resolution. It used a Shafer telescope, a holographic spectrometer grating, and a cooled silicon CCD. Configured as a pushbroom imager, it scanned full lines of pixels across a scene to create 2D images. VIMS-IR (Infrared) covers the 0.85 to 5.0 μm range. This opto-mechanical subsystem used a Cassegrain telescope, a ruled spectrometer grating, and a 256-element linear array, also cooled by a passive radiator. It operated as a whiskbroom imager, scanning one pixel

at a time in a raster pattern using a two-axis mirror.

VIMS was key to identifying compounds such as water, methane, ammonia, and organics on Saturn's moons, rings, and atmosphere. Its spectroscopic capabilities provided critical insights into the chemistry and evolution of the Saturn system.

2.3.6. Ultraviolet Imaging Spectrograph

The Ultraviolet Imaging Spectrograph (UVIS) studied the ultraviolet properties of Saturn's rings, atmosphere, and moons (Esposito et al., 2005). It observed how sunlight and starlight passed through these components, revealing their composition and structure.

UVIS includes several channels. Extreme Ultraviolet (EUV) covers the 56–118 nm range, and it is equipped with a telescope, a three-position slit changer, a spectrograph, and a CODACON microchannel plate detector. It includes a solar occultation mechanism that admits solar flux even with the Sun 20° off-axis. Far Ultraviolet (FUV) covers the 110–190 nm range, and it is similar to the EUV but with different gratings, coatings, and detector specs. It includes an ion pump power supply. High-Speed Photometer (HSP) measures stellar occultations to analyze the density and structure of Saturn's rings. It uses a photomultiplier tube and dedicated electronics. Hydrogen-Deuterium Absorption Cell (HDAC) measures hydrogen and deuterium abundances using absorption cells and a channel electron multiplier to detect unabsorbed photons.

UVIS provided extensive data on the ultraviolet characteristics of Saturn's system. It observed Saturn's auroras, atmospheric composition, temperature profiles, and Enceladus' plumes — supporting the case for a subsurface ocean. It also used occultation techniques to probe the rings and atmospheric layers, offering a comprehensive view of the system's structure and dynamics.

2.3.7. Observations from Cassini Instruments

This section elaborates on the key observations made by the aforementioned instruments regarding Enceladus and its plumes.

In-situ analysis of plume ejectiles

For the in-situ analysis of plume particles, the CDA was employed to record the dusts' special distribution and composition. Three categories of composition were identified: type I composed of water ice, type II composed of simple organic compounds such as silica, and type III containing sodium salts (Perry et al., 2015). The results showed that type II and type III dusts showed an increase in fraction in the vicinity of the plumes. The presence of type III dust suggests that the ocean is salty, similar to Earth's oceans, and could potentially support life. In addition, the CDA detected organic molecules and other compounds like silica in the plume particles. The presence of silica grains, in particular, suggested that these particles were formed in hydrothermal environments at the ocean floor, where water interacts with the moon's rocky core.

INMS was another instrument to conduct in-situ analysis of the water vapor plumes erupting from the south polar region of Enceladus (Perry et al., 2015). Two complications of INMS were identified: the spurious measurements caused by ice grains entering the INMS aperture and an instrument effect causing time distortion of the INMS measurement of water (Teolis et al., 2010). As Cassini flew through the plumes, INMS directly sampled the material, discovering that it was primarily composed of water vapor, but also contained other gases, including molecular hydrogen, carbon dioxide, methane, ammonia, and simple organics, such as carbon monoxide and nitrogen-bearing molecules (Teolis et al., 2017).

2.3.8. Remote sensing of plume

For the observation of plume, CIRS helped determine the temperature of the water vapor plumes erupting from Enceladus' surface and contributed to understanding the composition of the material in these plumes, which included water vapor, organic compounds, and traces of other gases (Porco et al., 2006). CIRS detected 3 to 7 GW of thermal emission from the south polar troughs at temperatures of at least 145 K (Spencer et al., 2006).

UVIS made significant contributions to the study of Enceladus' water vapor plumes. As Cassini flew through these plumes, UVIS detected water vapor and organic molecules in the ultraviolet spectrum

(Hansen et al., 2020). This confirmed that Enceladus is actively spewing material from its subsurface ocean into space. UVIS data also helped estimate the total mass of material being ejected from the moon's surface. UVIS used stellar occultation, in which the Sun passes behind Enceladus and the composition of the rings and atmospheres may be studied by observing how the sunlight was absorbed by gases and particles. These occultation provided high-resolution data on ring particle density and atmospheric composition. For the observation of eruptive activity, UVIS is an ideal instrument as many gases absorb light at ultraviolet wavelengths. This is detectable by UVIS' Far Ultraviolet (FUV) and Extreme Ultraviolet (EUV) sensors, and the High Speed Photometer (HSP) also makes use of occultation to profile plume structure (Hansen et al., 2020).

The ISS has captured images of water vapor plumes erupting from Enceladus' south pole. This may be seen in Figure 2.1. These images, combined with data from other instruments, suggested the presence of a subsurface ocean beneath the moon's icy crust. The images captured the plumes backlit by the Sun, providing stunning visuals of the material ejected into space.

2.3.9. Remote sensing of Enceladus surface

Along with the observation of plumes, CIRS was also employed to measure heat from the surface of Enceladus. CIRS played a critical role in discovering the thermal anomalies at Enceladus' south pole, where it detected heat emanating from the tiger stripe fractures. The measurements showed that the region was much warmer than expected, providing evidence of ongoing geological activity and suggesting that a subsurface ocean existed beneath the moon's icy crust.

VIMS mapped the surface of Enceladus with information on the composition of the surface, the physical state including grain size and crystalinity, and the temperature of the surface (Robidel et al., 2020). It was revealed that Enceladus is mostly covered in clean water ice but also showing regions with different material, including organics. UVIS observations revealed the presence of water ice and other volatiles on Enceladus' surface (Hendrix et al., 2010). It also provided insights into the thin atmosphere (or exosphere) around the moon, confirming that it is primarily composed of water vapor, with trace amounts of other gases.

ISS mapped the tiger stripe fractures at Enceladus' south pole, the sources of the plumes. This may be seen in Figure 2.2. These features were shown in incredible detail, providing a deeper understanding of the geological activity on this icy moon.

Analysis of E-ring

One of the key discoveries was the relationship between Enceladus' plumes and Saturn's E ring. The CDA confirmed that material from Enceladus' plumes is continually feeding and replenishing the E ring, creating a dynamic system where the particles in the ring are constantly being replenished by the moon. UVIS was also used to observe Saturn's fainter rings, such as the G ring and E ring. It helped identify small, dust-sized particles that populate these rings, many of which are likely sourced from moons like Enceladus.

Analysis of magnetosphere of Saturn

INMS studied the composition of ions and neutral particles in Saturn's magnetosphere, providing key insights into the interactions between Saturn's magnetic field and its moons, rings, and atmosphere (Smith et al., 2008). The instrument detected charged particles, including hydrogen ions, water group ions (H_2O^+, OH^+, O^+) and molecular nitrogen. With nitrogen ions being the most abundant near the orbit of Enceladus, it was proposed that the moon was the source. INMS helped confirm that much of the plasma in Saturn's magnetosphere comes from the water vapor plumes of Enceladus. The INMS detected neutral particles with an atomic mass of 28 in the plumes, during a close fly-by of Enceladus, while this could have been either molecular nitrogen or carbon monoxide. As water molecules from the plumes escape into space, they are ionized by solar radiation and magnetic interactions, contributing to the charged particle environment around Saturn.

2.4. Theoretical Background and Research on Plumes

This chapter serves to provide a theoretical foundation of the plumes on Enceladus. A brief background was provided in subsection 2.2.1, and this chapter will further elaborate into this matter by reviewing past

research attempts to model Enceladus' internal structure, as several hypotheses have been suggested regarding the mechanism of the plumes. The chapter first reviews a shear heating model by Nimmo et al., 2007, hypothesizing it as the source of plumes. The chapter then focuses on the source of water supplying the plumes hypothesized by Postberg et al., 2011. Next, the transfer mechanism of heat and chemicals hypothesized by Matson et al., 2012 is reviewed. Finally, a physical model of the plume after vent developed by Yeoh et al., 2015 is reviewed.

2.4.1. Shear Heating as Source of the Plumes

Nimmo et al., 2007 shows that the most likely explanation for the heat and vapor production is shear heating by tidally driven lateral (strike-slip) fault motion. Figure 2.10 shows that the temperatures and temperature gradients near the strike-slip zone are significantly increased as a result of the brittle and viscous heating. In this figure, the bold dashed line represents a vertical fault along which lateral shear occurs. The energy generated by shearing will be partitioned principally between heating and vapor sublimation. A dimensionless free parameter, α, is adopted to describe this partitioning, where α = 0 implies that all the energy goes into vapor production, and α = 1 means all the energy goes into heating. The shear velocity here is $8 \times 10^{-6} ms^{-1}$ and α = 0.1.

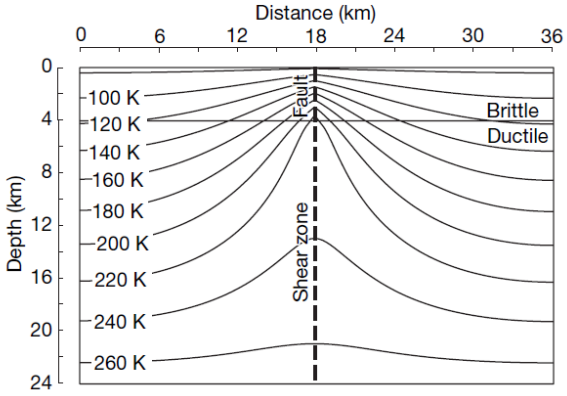

Figure 2.10: Cross-section of steady-state temperature structure (in kelvin) for a shear velocity of $8 \times 10^{-6} ms^{-1}$ and α = 0.1 Nimmo et al., 2007.

Vapor produced by this heating may escape as plumes through cracks opened by the tidal stresses. The ice shell thickness needed to produce the observed heat flux is at least 5 km.

The Love number, h_2, is defined as susceptibility of a body's shape to change in response to an external tidal potential. Figure 2.11 shows the Love number as a function of ice shell viscosity for spherically symmetric models with and without a subsurface ocean. A model with a global subsurface ocean can reproduce the shear velocities required for reasonable assumptions of ice viscosity. The shaded region in the figure shows the probable viscosity range for an ice shell with a grain size of 0.1 to 10 mm and a temperature of 250 to 270 K. Shear velocity is denoted as u in the figure.

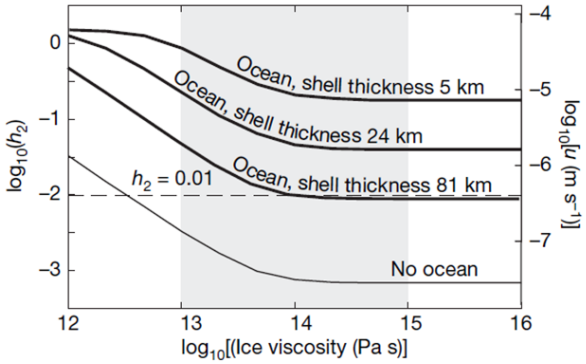

Figure 2.11: Effect of interior structure on mean shear velocity from Nimmo et al., 2007.

In the model from this research, the shear velocities required to match the observations imply a Love number greater than 0.01. A model with a global subsurface ocean can reproduce the shear velocities required fro reasonable assumptions of ice viscosity. In the absence of an ocean, unrealistically low ice shell (or silicate mantle) viscosities are required.

2.4.2. Source of Water Supplying the Plumes

Postberg et al., 2011 reports an analysis of the composition of freshly ejected particles from the plume. Salt-rich ice particles are found to dominate the total mass flux of particles above the detection threshold of the CDA by more than 99% but they are depleted in the population escaping into Saturn's E ring. Ice grains containing organic compounds are found to be more abundant in dense parts of the plume. Whereas previous Cassini observations were compatible with a variety of plume formation mechanisms, these data eliminate or severely constrain non-liquid models and strongly imply that a salt-water reservoir with a large evaporating surface provides nearly all of the matter in the plume.

As introduced in subsection 2.3.7, most plume mass spectra can be assigned to one of three compositional types. Type III (6% of E-ring detections) is particularly rich in sodium and potassium salts (0.5–2% by mass). The composition of these salt-rich grains closely resembles the predicted composition of an ocean that has been in prolonged contact with the rocky core of the moon. Shortly before closest approach of Cassini's E5 flyby, the proportion of salt-rich grains increases steeply from E-ring background levels, reaching 40% just after closest approach, followed by a shallower decrease towards the dense plume. Simultaneously, the proportion of salt-poor type I grains starts to decrease shortly before closest approach. The most plausible explanation for the simultaneous increase of type III and decrease of type I proportions is that salt-rich grains become more abundant close to the sources located in the south polar terrain.

A plume source dominated by salt-rich grains eliminates the possibility of significant contributions from dry, sodium-poor sources and severely constrains or rules out non-liquid models in their present form. In a clathrate decomposition scenario, a substantial part of the water vapor in the plume forms from the sublimation of ice grains entrained in a flow of initially released volatile gases (CO_2, N_2, CO, CH_4). However, sublimation of sodium-rich grains would lead to the release of sodium into both the plume's gas phase and the E ring, which is not observed. Models employing sublimation from warm ice currently cannot account for the predominant formation of salt-rich ice grains. As all sodium compounds should have been originally bound in rock after the moon's formation, the salt in plume grains must have been extracted from Enceladus' rocky material by water.

2.4.3. Transfer mechanism of heat and chemicals

Matson et al., 2012 hypothesized that a subsurface ocean is the heat reservoir for thermal anomalies on the surface and the source of heat and chemicals necessary for the plumes. Figure 2.12 schematically depicts six major components of an ongoing water circulation system below Enceladus' active south polar areas hypothesized by Matson et al., 2012.

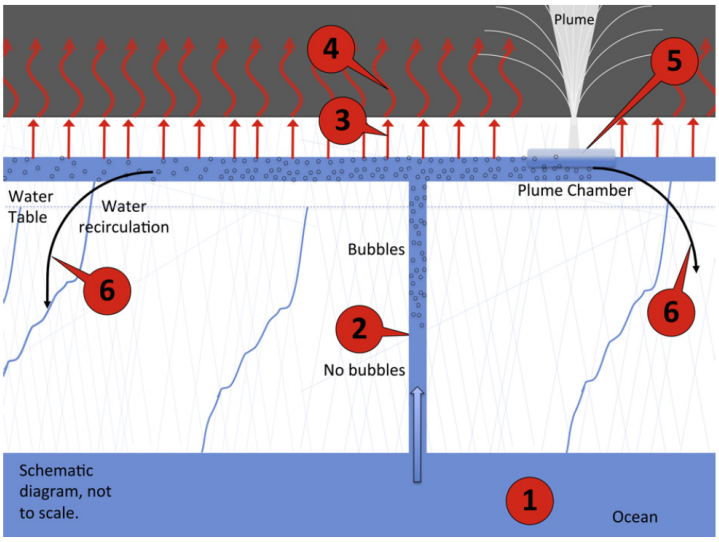

Figure 2.12: Notional sketch illustrating the hypothesis of ocean water circulation Matson et al., 2012.

At the bottom is the subsurface ocean (#1) that underlays the South Polar Region. The ocean is found to be relatively warm (0 °C). The seawater contains dissolved gases that exsolve as pressure falls below the saturation pressure for each gas species. The pressure reduction and exsolution occur as water rises toward the surface. Exsolved gases initially form tiny bubbles that reduce the overall density. With the exsolution of enough gas, the ocean water becomes buoyant with respect to the solid ice crust and rises towards the surface if fractures or fissures in the ice have provided conduits, shown schematically at #2. Near the surface, the water flows beneath a protective ice cap and spreads out laterally. A symbolic surface thermal anomaly is indicated by #3 where heat from the water is being conducted through the ice cap to the surface. These areas of anomalously high surface temperatures radiate heat to space, shown as #4. In the plume chambers at #5, ocean water and its contents are converted into vapor and aerosols. The flow of ocean water through a plume chamber replenishes the chemicals that have erupted as well as the energy. As the plumes erupt, pressures in the chamber are low and it is assumed that all of the carbon dioxide is exsolved from the ocean water and becomes part of the plume. As the water loses heat and gas it becomes colder and denser. It returns to the ocean, indicated by #6, via fissures or cracks in the icy crust.

When water emerges at Enceladus' surface it boils vigorously. The latent heat for the vaporization of water is large and is drawn from the remaining liquid water that rapidly cools and freezes. Evaporation stops when the weight of the forming ice cap exceeds the vapor pressure of water.

The problem in bringing volatile-free ocean water to Enceladus' surface is that the water column stalls before it reaches the surface. Equation 2.1 shows the height, h, in which water can rise in a vertical opening.

$$h = (\rho_{ice}/\rho_{oceanwater})h_c \tag{2.1}$$

Here, ρ_{ice} denotes the density of ice, $\rho_{oceanwater}$ denotes the density of ocean water and h_c denotes the thickness of the crust. Seawater has a density of 1020 kgm^{-3} whereas the density of ice is 920 kgm^{-3}, and the height to which water can rise in a vertical opening in the icy crust is proportional to the ratio of ice density to water density. Seawater can therefore rise approximately 90% of the way up to the surface in an open conduit. The energy required to lift seawater comes from expansion of the gas in the bubbles. As ocean water travels from below the crust and rises toward the surface, the exsolution of bubble-forming gas is governed by Henry's Law.

$$P_{CO_2}(X_CO_2) = H_{const}X_CO_2 \tag{2.2}$$

Here, P_{CO_2} is the pressure at which the liquid is saturated with the dissolved gas, X_{CO_2} is the mole fraction of carbon dioxide, and H_{const} is Henry's Constant. A CO_2 equivalent-gas molar fraction of 4 $\times$ 10^{-4} for the ocean is sufficient to support the circulation.

2.4.4. Physical Modeling of the Plume After Vent

Yeoh et al., 2015 investigated the physical processes and the interaction between the gas and the grains associated with the expansion process. The plume from the surface vents out into vacuum were simulated using the direct simulation Monte Carlo (DSMC) method, with two-way coupling between the gas and the grains, in which the gas and the grains affect each other. Only momentum and energy coupling are modeled between the gas and the grains. The grains are assumed to be made of ice, with a density of 920 kg/m^3 and a specific heat capacity of 2.11 kJ/kgK. Several conclusions about the flow expansion process from the vents into vacuum and the interaction between the gas and the grains were reached.

As the flow expands from the vents into vacuum, it passes through multiple regimes, from continuum (very collisional) near the vents to free-molecular (collisionless) at higher altitudes. Knudsen number Kn is defined as the ratio of the molecular mean free path length to a representative physical length scale. The different flow regimes are characterized by the local Knudsen number, from 10^{-3} near the vent (highly collisional) to >10 (collisionless) at an altitude of 10 km for a vent diameter of = 2.8 m. This is shown in Figure 2.13, in which Z represents altitude and R represents radial distance.

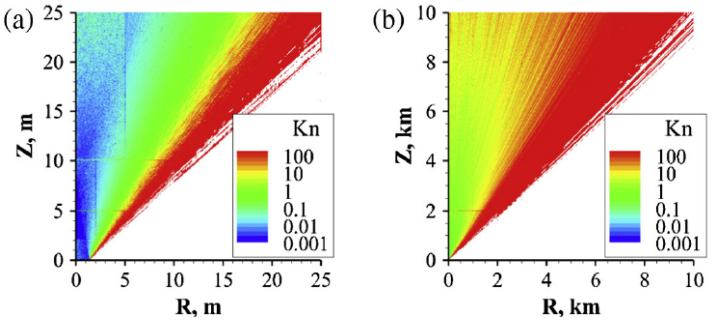

Figure 2.13: Contours of local Knudsen number, Kn, from (a) vent to 25 m and (b) vent to 10 km from Yeoh et al., 2015.

For a given set of vent conditions, the altitude at which this transition occurs, Z_{FM}, increases with vent diameter, D_{vent}. During expansion, the gas number density, n, drops rapidly across expansion waves emanating from the edges of the vent. As the flow expands, the random kinetic (thermal) energy and the rotational energy of the gas molecules are converted into the directed mean kinetic energy of the flow through collisions. As a result, the gas translational temperature and rotational temperature (measures of the molecular thermal and rotational energy respectively) drop as the bulk gas speed increases. As the flow expands, Mach number increases rapidly mainly due to the rapid drop in temperature rather than the increase in bulk gas speed. The gas speed only increases slightly over that distance (<10%).

The effects of collisions at the vent on molecular velocities are characterized by the Knudsen number at the vent. The molecular velocity is decomposed into three mutually orthogonal components, as shown in Figure 2.14.

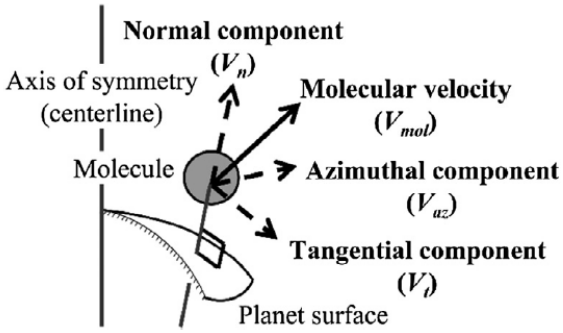

Figure 2.14: Decomposition of molecular velocity Yeoh et al., 2015.

For all Kn_{vent} considered, the flow has become collisionless at an altitude of 10 km. The altitude at which the flow first becomes collisionless varies with Kn_{vent}. The results are shown in Figure 2.15a-e, showing distributions of molecular velocities at 10 km altitude for several Kn_{vent} values. Collisions in the near-field have a strong influence on the distribution of molecular speeds in the far-field as the flow becomes free-molecular. As Kn_{vent} decreases, the spread of molecular velocities (thermal spread) shrinks and the molecular speeds, approximated by the distance from the origin (because V_{az} is small), approach the ultimate speed of adiabatic expansion. For the triple-point of water, this speed is approximately 1005 ms^{-1}. This is because a more collisional flow at the vent can convert a larger fraction of the molecular thermal and internal energy into the directed mean kinetic energy of the gas before the flow becomes free-molecular. Once Kn_{vent} is sufficiently small, the flow is collisional enough to convert nearly all molecular thermal and internal energy into directed mean kinetic energy and any further decrease in Kn_{vent} only changes the velocity distribution slightly.

There is a larger spread of velocities near the top part of the distribution even for very small Kn_{vent}. Figure 2.15f explains this phenomenon by color-coding the velocity samples used to construct the velocity distribution for the nominal case. The color-coding shows the initial radial position of the molecules in the vent. There is a clear correlation of velocity with initial position. As a result, the molecules originating from the edge of the vent maintain their initial thermal spread of velocities.

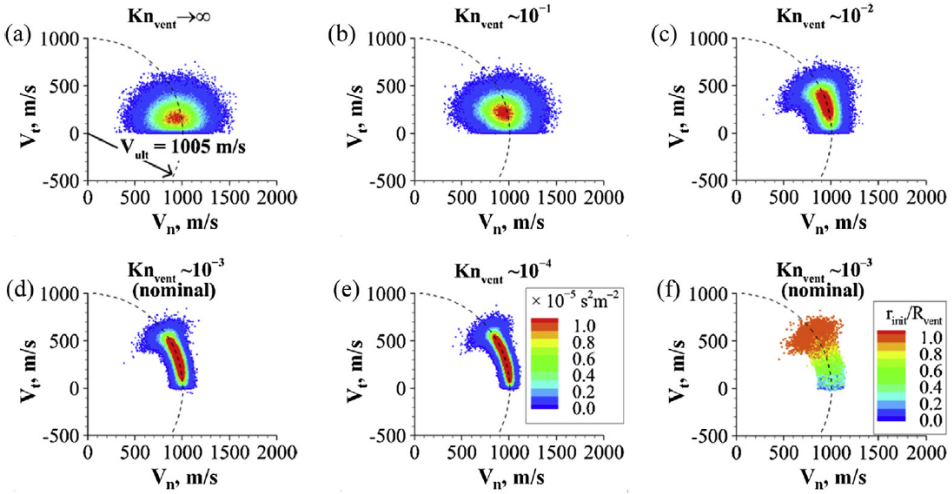

Figure 2.15: (a-e) Distributions of molecular velocities at altitude of 10 km for several values of Kn_{vent}; (f) Distribution of molecular velocities at altitude of 10 km for nominal case colored by initial radial positions of molecules in vent Yeoh et al., 2015.

The flow is highly supersaturated just as it emerges from the vents, as the supersaturation ratio between local gas pressure, p, and equilibrium vapor pressure, p_{vap}, near the vent is approximately 10^{40}. Thus, condensation grain growth is very likely. This is shown in Figure 2.16a. On the other hand, the collision rate, ζ, must also be sufficiently high for condensation and grain growth to actually occur. The ζ value

drops by several orders of magnitude from the vent value within only 25 m of the vent, as shown in Figure 2.16b. thus most of the condensation and growth must occur within several D_{vent} of the vent.

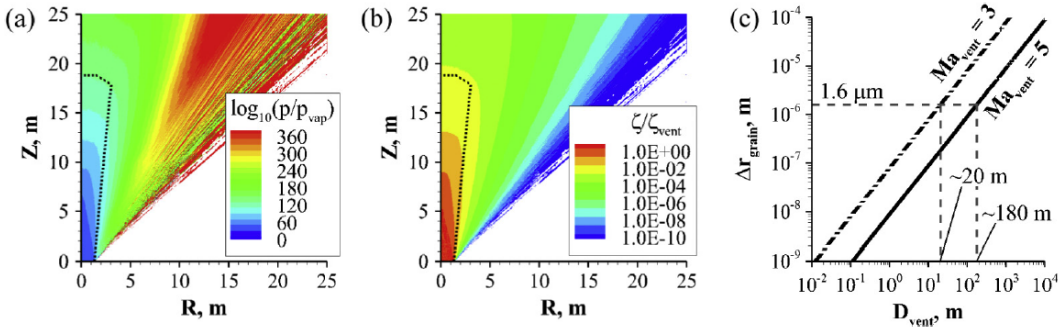

Figure 2.16: Contours of (a) $log_{10}(p/pvap)$ and (b) collision rate normalized by vent value, ζ_{vent}, from vent to 25 m for Mach-5 vent conditions; (c) maximum possible increment in grain radius due to condensation as function of vent diameter for Mach-3 and Mach-5 vent conditions Yeoh et al., 2015.

Considering heterogeneous nucleation, the maximum possible increment in grain radius due to condensation above the vents was estimated. Grain growth is defined to be the difference between the final and initial grain radii, as $\Delta r_{grain} = r_f - r_0$. For a given vent Mach number M_{vent}, it was determined that Δr_{grain} is a linear function of vent diameter. This is shown in Figure 2.16c. For a given M_{vent}, the altitude at which the first expansion wave crosses the center line and the density drops from the vent value is proportional to D_{vent}. Consequently, a larger vent leads to a greater growth because the grain travels a longer distance and spends more time in a region of higher density and collision rates. Vents with diameters above 20 m for a Mach number of 3 would be required to produce the grains detected by CDA ($rgrain \geq$ 1.6 μm) via condensation if the grains emerge from the vent with a negligible initial size. Likewise, diameters above 180 m would be required for a Mach number of 5 to produce grain sizes detected by CDA. As a result, the detection of smaller vents would suggest that condensation alone could not account for these grains.

The vent mass flow rate ratio, ϕ, is proportional to the total mass ratio of ice grains to vapor in the plume. When ϕ = 0.1, grains barely affect the gas flow, regardless of the grain size as there is minimal exchange of momentum and energy between the gas and the grains. The coupling is effectively one-way, from the gas to the grains. Meanwhile, the effects of the grains are more significant when ϕ = 1.0. Near the center line where the grains are concentrated, the gas number density and translational temperature are noticeably higher, and the gas speed is noticeably slower. A higher ϕ results in more grains in the gas flow, leading to a greater exchange of momentum and energy between the gas and the grains. Moreover, the more numerous grains form a thicker column over the vent and trap the gas in the column. As a result, the gas can no longer expand freely into vacuum but is constrained by the column of grains. The larger grains have a greater and more widespread effect on the gas flow than the smaller grains. Additionally, the larger grains track the gas flow better. Furthermore, the larger grains have a larger total surface area, which leads to a higher overall rate of heat transfer, and a larger total cross sectional area, which results in a larger overall drag on the gas flow.

Nanometer-sized grains are accelerated close to gas speeds while micron-sized grains tend to retain their initial speeds at the vent due to their greater inertia. Consequently, the speeds of the smaller grains provide a better constraint on the gas speeds while the ejection (initial) speeds of the larger grains can be better constrained from measurements.

2.5. Experimental Research on Enceladian Plumes

Along with the theoretical models of the Enceladian plume, experimental models are also a focus of the research regarding this topic. The goal of the experimental models is to investigate how the plume mechanisms proposed from the theoretical models compare with the results of the experimental model. The research at TU Delft experimentally simulates the topology of ice crevasses and the subsurface ocean with a narrow channel mounted on top of a water reservoir in a vacuum chamber. The objec-

tive here is to determine if crevasse geometry may be constrained from temperature, pressure and velocity measurements from the experimental model. This chapter serves to elaborate on the current experimental research on the plumes of Enceladus.

2.5.1. Plexiglass Model

Sklavenitis, 2021 simulated the liquid water reservoir lying under the ice crust of Enceladus with a liquid water reservoir. The setup takes place inside a vacuum chamber. The model is made from cylindrical plexiglass, and its role is to simulate the underground ocean, crust and fissures in the crust of Enceladus. The model may be divided into the reservoir, nozzle and exit. The reservoir is partly filled with liquid water or ice to simulate the underground ocean. The nozzle channels the gas from the reservoir to external space to simulate the crevasses. The exit represents the vent of the plumes. As pressure is reduced in the vacuum chamber, liquid water boils at a lower temperature, creating vapor that will exit the model through the channels. The heating foils placed inside the reservoir controls the temperature of liquid water and the amount of latent heat provided to the water undergoing vaporization. The heat capacity of the underground ocean on Enceladus may be assumed to be infinite as a few minutes of plume activity should have negligible influence on the stored energy of Enceladus. A picture of the model and a schematic of the model is shown in Figure 2.17.

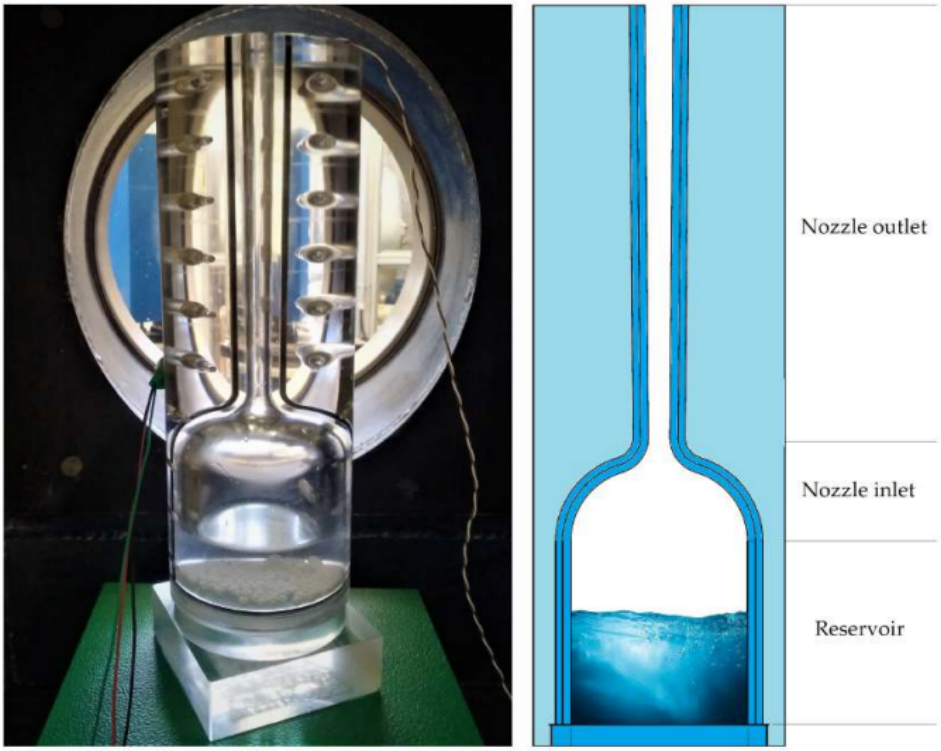

Figure 2.17: Left: Photograph of the manufactured model in side the test section of the vacuum chamber from Sklavenitis, 2021. Right; A vertical cross-section schematic of the plume model from Sklavenitis, 2021.

Sklavenitis, 2021 makes use of a small reservoir and a large reservoir design. Both of these models use the same nozzle, but have different reservoir. As suggested by their names, the main difference between the two models is the size of the reservoir. Additionally, the large reservoir model has a higher heating ability due to the placement of more heating foils. The small reservoir model was designed prior to the commencement of this study. Therefore, the process that was followed and concluded to its design is out of this study's context. As the vaporized water flows through the channel, temperature and pressure are monitored. Thermocouples determine temperature using two dissimilar electrical conductors forming an electrical junction. The measured voltage is used to determine the temperature. The differential pressure sensors determines the difference in pressure between two ports using voltage outputs. The plume is also visually monitored through the windows of the vacuum chamber. A camera

used to record the plume model as well as Particle Image Velocimetry is used. Using tracer particles in the flow, the movement of the flow may be visualized. As a result, a velocity field may be obtained based on the displacement of the tracer particles. A pair of images are taken in a time interval, Δt, and statistical methods are used to determine the particle displacement over this interval, leading to the local velocity.

Research by Giordano, 2023 also conducted experiments using a plexiglass reservoir. The reservoir contained distilled water to mimic the subsurface ocean and a 3D printed PLA (Polylactic acid) channel to simulate a crevasse in the ice crust of Enceladus. For this study, a uniform cross sectional area channel with a length of 245 mm and a diameter of 5.7 mm was used. A The model was placed inside a vacuum chamber, evacuated throughout the experiment by two vacuum pumps to achieve pressures below the saturation point of water vapor, causing the water to boil. The first series of experiments were conducted with the channel at room temperature, and this was designated as the warm model. A subsequent set of experiments were performed with an ice block encased around the outer surface of the channel, cooling the channel walls and sustaining a uniform wall temperature throughout the experiment. This configuration was designated as the frozen model. Melting of ice before starting the experiment ensured that the model was at approximately 0 degrees Celsius. However, as the vacuum chamber reached low pressures, sublimation took place, leading to a cooling effect on the ice. Consequently, the observed model temperatures ranged between 0 and -5 degrees. A section of the Hypersonic Test Facility Delft was utilized as vacuum chamber. The minimum pressure observed in this vacuum chamber is approximately 1 mbar. The vacuum pumps evacuate the chamber throughout the duration of an experiment to guarantee the lowest pressure possible. Temperature equipment here were also acquired with type-T thermocouples.

2.5.2. Ice Model

In contrast to the plexiglass model, the ice model used nozzles that were made of ice to recreate the plumes of Enceladus. A vacuum chamber at FH Aachen, reaching a pressure of 8 Pa, was used for this research. The ice model was driven by the ice layer and liquid ocean of Enceladus. The physical characteristics of the model were based on the relations between the throat and vent area, and a supersonic nozzle-like structure was created in order to reach the plume exhaust velocities observed by Cassini. The model was made by pouring water into a mold, freezing this water and removing the mold once frozen. A picture of the ice model is shown in Figure 2.18.

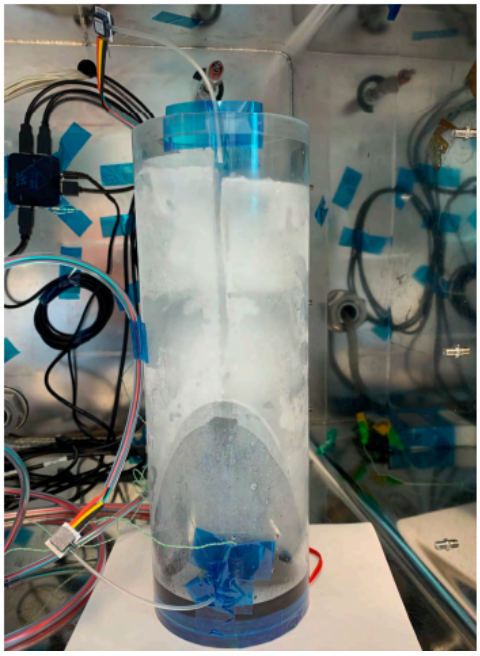

Figure 2.18: The setup of the (small) ice model in a vacuum chamber, including sensors and heating foils.

3

Research Plan

3.1. Introduction of the Project

As introduced in subsection 2.4.4, the profile of ejectiles from the Enceladian subsurface ocean may be used to infer the mechanism of the plumes. For instance, a larger vent may lead to greater growth of ejected grains, as the grain travels a longer distance and therefore more time in a region of high density and collision Yeoh et al., 2015. As such, analysis of the ejected particles provide a clue as to how these particles came to form, and this may be used to infer the possible environments that would allow such particles to form. The current analysis of the ejected particles come from the observation results obtained by Cassini and the computational modeling of the plumes using those observation results as constraints.

On the other hand, experimental approaches to the mechanism has also been made, as introduced in chapter 2. Several models have been made and tested to recreate the plumes in a laboratory to study the possible structures of the plumes that would produce the similar results as observed by Cassini. While the measurement of the ejectile particles have been performed in the past, it may not fully reflect the true profile of the particles, as noted by Sklavenitis, 2021. Particle Image Velocimetry (PIV) was employed in the work by Sklavenitis, 2021 to visualize the plumes and determine the velocity field. This method works by supplying a flow with tracer particles that illuminate in the flow to be traced optically. The initial intention was to use PIV to detect water particles that form due to nucleation of vapor, however it is unclear if these particles are large enough to be detected. Sklavenitis, 2021 notes that it is unclear if the detected particles are water particles or dust traces that was used to trace the plume in preliminary experiments. This points to the goal of this research to fully visualize the particles in order to achieve the research goal of experimentally inferring the possible mechanism of the Enceladian plumes.

3.2. Research Questions

The goal of this research is to provide an answer for the main research question below.

RQ: How can the plume's ejecta from an icy moon's subsurface ocean be visualized, and what can these reveal about the origin of the plumes?

This main research question may be deconstructed into several sub questions that lead back to the answer for the question above. The research question for the first phase of the project, RQ1, is as shown below. Moreover, based on the formulated research questions, the work packages can be constructed. Every small work package is allocated with a time period. It shall be noted that the work packages may be performed in parallel.

RQ1: How can Enceladus' plumes and the flow of gas and icy particles be recreated in a laboratory? *WP1: Recreate icy particles in an experimental plume setup.*

- **RQ1.1**: Can the existing laboratory setup be employed to recreate ice grains typical to Enceladus' plumes?

WP1.1: Use the existing set-up and vary temperatures and pressures to produce icy particles (2 weeks, in parallel with WP1.2).

- **RQ1.2**: What are the characteristics of the plume particles observed in the laboratory plume?
  WP1.2: Visually identify the characteristics of the icy particles (2 weeks, in parallel with WP1.1).
- **RQ1.3**: What are the constraints in employing a detection system regarding laboratory setup?
  WP1.3: Review the specifications of the experiment chamber to prepare the techniques that are feasible (<1 week, in parallel with WP1).

The first research question focuses on the utilization of the currently existing laboratory setup for the experiments needed in this research. The crucial point in this step is to ensure that icy particles can be generated from the setup. As the goal of this research is to detect and measure the velocities and sizes of the particles, a plume model with only vapor production would not be applicable for this study. As the production of particles in the laboratory setup is confirmed, the characteristics of the particles needs to be determined to connect to part of the next research question of generating requirements for the new detection system.

RQ2: What is the ideal method to visualize plume ejecta from an icy moon? *WP2: Determine the ideal method to visualize plume ejecta from an icy moon.*

- **RQ2.1**: What is required from the detection system for plume ejecta from an icy moon?
  WP2.1: Identify the requirements needed to detect grain velocities and sizes for Enceladus and laboratory experiments.
- **RQ2.2**: What are the possible technologies to detect and visualize the plume ejecta?
- *WP2.2: Select a concept to detect grain velocities and sizes for laboratory plume experiments.*
  - *WP2.2.1: Identify the possible technologies that may be employed (<1 week).*
  - *WP2.2.2: Conduct a trade off (<1 week).*
- **RQ2.3**: How can the selected detection technology be integrated in a laboratory setup?
  WP2.3: Integrate the selected technique to conduct experiments and measure results.
  - *WP2.3.1: Create a detailed design of the selected detection system (1 week).*
  - *WP2.3.2: Construct the detection system (2 weeks).*
  - *WP2.3.3: Conduct the experiments (2 weeks).*

In order to employ a technology to detect the particles ejected from plumes, the essential preceding step would be to identify what is required from the detection system. RQ3.1 addresses this point. Moreover, its sub-questions address the specific measurement that needs to be detected as well as constraints and feasibility regarding employment of the technology in the current setup. As an output of this phase, a set of requirements for the detection system may be constructed. The second sub-question, RQ3.2, addresses the following step of exploring and generating solution concepts. As a list of concepts are generated, the trade-off phase will evaluate the advantages and disadvantages of each concepts with respect to each requirement. In order to guarantee a successful end result, several concepts may be selected with priority. Following the trade off phase is the integration phase of the detection system. RQ3.3 addresses this phase. The integration phase is a key step to implementing the concepts into practice. This involves procurement of the technology, sizing the instruments for the laboratory setup and testing the detection system. If the selected technology is deemed to be unfeasible in the integration, then the secondary plan as selected in the previous phase shall be executed.

The second research question for the second phase, RQ3, is as shown below.

RQ3: What can be concluded from the grain velocities and sizes measured using the selected detection technology?
WP3: Conduct an analysis of the grain velocities and sizes measured using the selected detection technology and discuss its scientific implications.

- **RQ3.1**: What are the characteristics of the plume ejecta measured from the experiments?
  WP3.1: Determine the characteristics of the plume ejecta measured from the experiments.

  - **RQ3.1.1**: What is the spatial variation of the grain velocities and sizes above the vent?
    WP3.1.1: Measure the velocities and sizes of particles using the technique developed in WP2.3 (1 week).
  - **RQ3.1.2**: What is the relationship between the measured grain velocities and grain sizes?
    WP3.1.2: Determine the relationship between the measured grain velocities and grain sizes (<1 week).

- **RQ3.2**: What do the results imply about icy moon plumes mechanism?
  WP3.2: Conclude on the implications that the experiment results have on the mechanism of icy moon plumes.

  - **RQ3.2.1**: What can be inferred about the formation mechanism of the grains from the results?
    WP3.2.1: Using experiment results, infer about the formation mechanism of the grains (1 week).
  - **RQ3.2.2**: What can be inferred about the interior structure of the icy moon from the results?
    WP3.2.2: Using experiment results, infer the interior structure of the Enceladus (1 week).
  - **RQ3.2.3**: How do the results compare to the values observed by Cassini?
    WP3.2.3: Compare experiment results to the values observed by Cassini (<1 week).

  WP3.3: Verify and validate the results of the experiment (1 week).
  WP3.4: Finalize the research report (<2 weeks).

The second phase of the project conducts the experiments and processes the results obtained from the testing of the detection technology. Multiple sub questions were generated with regard to the scientific goals generated in the initiation of this project. RQ2.1 is formulated for the data processing step to grasp the full image of the plume ejecta velocities and sizes. This includes identifying the spatial variation of the grains as well as the coupling of the two parameters. The second sub-question, RQ2.2, analyzes the results from the previous step and discusses about the implications it has on the mechanism of the plumes. This includes the formation mechanism of the grains as well as the interior structure that can be inferred from the results.

3.3. Research Plan

In addition to the work packages above, there are several milestones over the course of the project. With these milestones included, a Gantt chart may be created to visually organize the work packages and the timeframe.

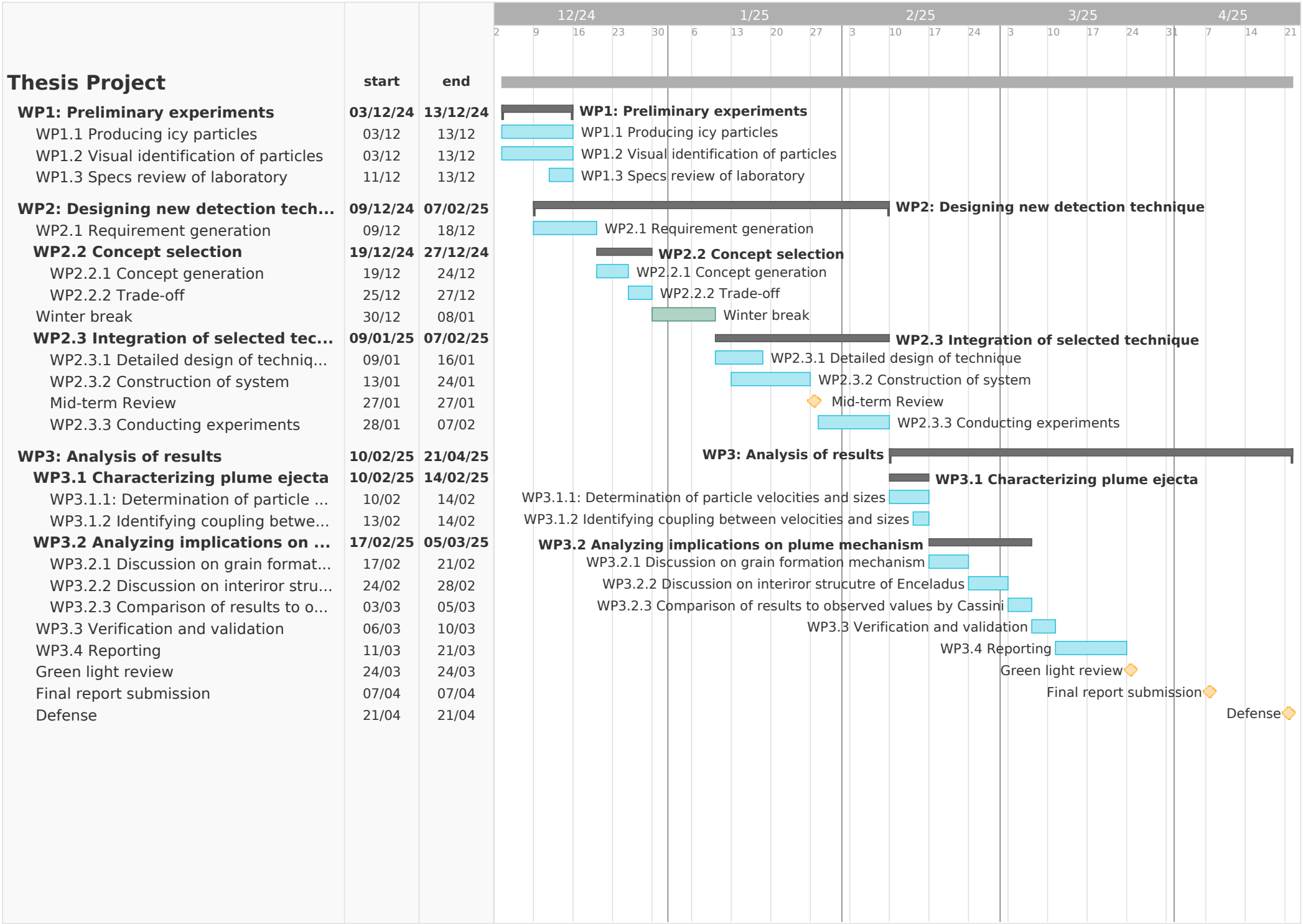

Thesis Project	start	end
WP1: Preliminary experiments	**03/12/24**	**13/12/24**
WP1.1 Producing icy particles	03/12	13/12
WP1.2 Visual identification of particles	03/12	13/12
WP1.3 Specs review of laboratory	11/12	13/12
WP2: Designing new detection tech...	**09/12/24**	**07/02/25**
WP2.1 Requirement generation	09/12	18/12
WP2.2 Concept selection	**19/12/24**	**27/12/24**
WP2.2.1 Concept generation	19/12	24/12
WP2.2.2 Trade-off	25/12	27/12
Winter break	30/12	08/01
WP2.3 Integration of selected tec...	**09/01/25**	**07/02/25**
WP2.3.1 Detailed design of techniq...	09/01	16/01
WP2.3.2 Construction of system	13/01	24/01
Mid-term Review	27/01	27/01
WP2.3.3 Conducting experiments	28/01	07/02
WP3: Analysis of results	**10/02/25**	**21/04/25**
WP3.1 Characterizing plume ejecta	**10/02/25**	**14/02/25**
WP3.1.1: Determination of particle ...	10/02	14/02
WP3.1.2 Identifying coupling betwe...	13/02	14/02
WP3.2 Analyzing implications on ...	**17/02/25**	**05/03/25**
WP3.2.1 Discussion on grain format...	17/02	21/02
WP3.2.2 Discussion on interiror stru...	24/02	28/02
WP3.2.3 Comparison of results to o...	03/03	05/03
WP3.3 Verification and validation	06/03	10/03
WP3.4 Reporting	11/03	21/03
Green light review	24/03	24/03
Final report submission	07/04	07/04
Defense	21/04	21/04

4

Experimental Setup

This chapter elaborates on the experimental setup used for the research on the solid particle detection technique development. An overview of the test environment, including the vacuum chamber and other related equipment are first elaborated. The chapter then describes the plume model that is placed inside the vacuum chamber. Here, details on the plume geometry, the reservoir, and the cooling system are described. Finally, the measurement system of the experimental model is elaborated.

4.1. Test Environment

This section describes the test environment of the plume model. The environment consists of a vacuum chamber in which the plume model is placed in, a pair of primary vacuum pumps, and a cryogenic pump (cold finger). An overview image of the experimental setup in the vacuum chamber is as shown in Figure 4.1. The subsequent subsections describe the components that make up the test environment.

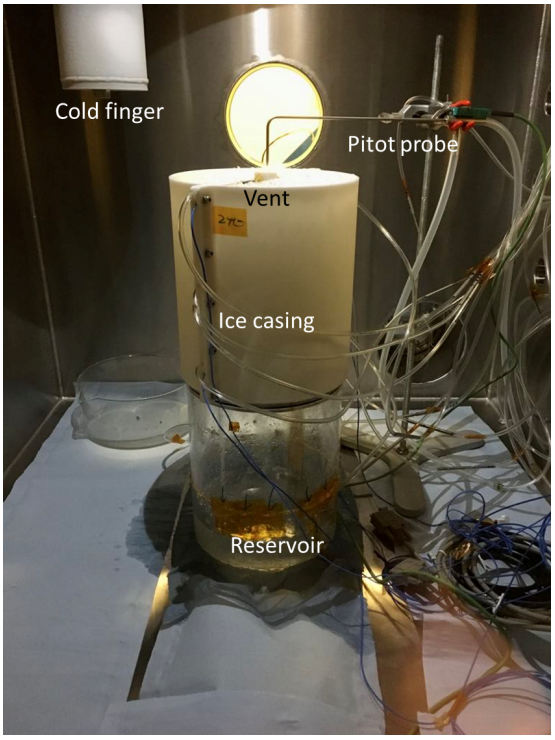

Figure 4.1: Image of the experimental setup placed in the vacuum chamber. The transparent cylinder located at the bottom is the reservoir, and the white cylinder on the top is the casing for the coolant, with the channel located at the center of this cylinder.

4.1.1. Vacuum Chamber

A vacuum chamber located in the Delft Planetary Labs of TU Delft Faculty of Aerospace Engineering is employed to recreate the low pressures found on the surface of Enceladus. The chamber, with its cubic shape, has side lengths of 80 cm, making up a total volume of 512 liters. The chamber is constructed with stainless steel, with a tested leak rate below 1×10^{-7} mbar L/sec The chamber is equipped with feedthroughs in which sensor wiring from outside the vacuum chamber may be connected to. The feedthroughs employ eleven DN40 KF flanges with one multi-pin electrical feed through, three differential pressure line feedthroughs, two type K thermocouple feedthroughs, two gas inlet/outlet feedthroughs, two liquid nitrogen supply feedthroughs, and four 9-pin D-Sub standard connector feedthroughs. Small windows are located on each side of the vacuum chamber for visual observation. Moreover, the vacuum chamber is equipped with a cold finger used as a cold trap, suspended from the chamber ceiling in the far left corner of the chamber as visible in Figure 4.1, with a diameter of 11 cm and a height of 28 cm. Air is evacuated to pressures below 1 mbar in the chamber during testing, and the exact minimum pressure varies between trials. In the baseline experiments, minimum pressure varies between 0.026 mbar and 0.520 mbar (with the use of cryogenic pumping). The variability in minimum pressure may be due to the temperature and pressure conditions within the laboratory as well as the performance variation of the vacuum pumps. Temperature inside the chamber is not controlled, thus the cooling of the channel is achieved via direct contact of channel wall to ice.

4.1.2. Vacuum Pump

Pressure is lowered in the chamber using two primary pumps throughout the experiment. The pumps used here are the air-cooled ECODRY plus 40 (Leybold) and the TURBOVAC 850 i(X) (Leybold). The primary pumps are employed 1-2 minutes after the start of data acquisition to allow for a calibration of the sensors. The pumps are then kept running for the entire duration of the experiment. In order to have a consistent performance of the pump, the pumps are kept on dry run prior to an experiment.

4.1.3. Cryogenic Pumping

Cryogenic pumps, colloquially called a cold finger, achieve high vacuum by cooling internal surfaces to low temperatures, causing gases and vapors to be removed from a vacuum chamber. Heavier gases like water vapor condense on cold surfaces. Liquid nitrogen is poured into the cold finger to achieve the low temperature needed to further reduce the pressure. With the system of these evacuation methods, the vacuum chamber reaches a minimum pressure of below 1 mbar with the exact minimum pressure varying between experiments. Liquid nitrogen is poured into the cold finger at as vacuum chamber pressure reaches 100 mbar. As pressure is lowered in the chamber, the decrease in pressure is reduces at a pressure below 10 mbar. This may be seen in Figure 4.2, showing the absolute pressure of the vacuum chamber in a case that cryogenic pump is not employed. Here, the absolute pressure in the chamber is mainly measured by the reading with the label ”TTR PISCES”, with the other two sensors serving as supplemental information on the pressure conditions inside the chamber. Details on the sensor setup is elaborated in section 4.3. In order to bolster the reduction of pressure alongside the primary pumps, the cryogenic pump is employed. As the cryogenic pump has some time lag between time at which liquid nitrogen is poured into the cold finger and the time at which pressure starts reducing, it is poured in as chamber pressure reduces below 100 mbar.

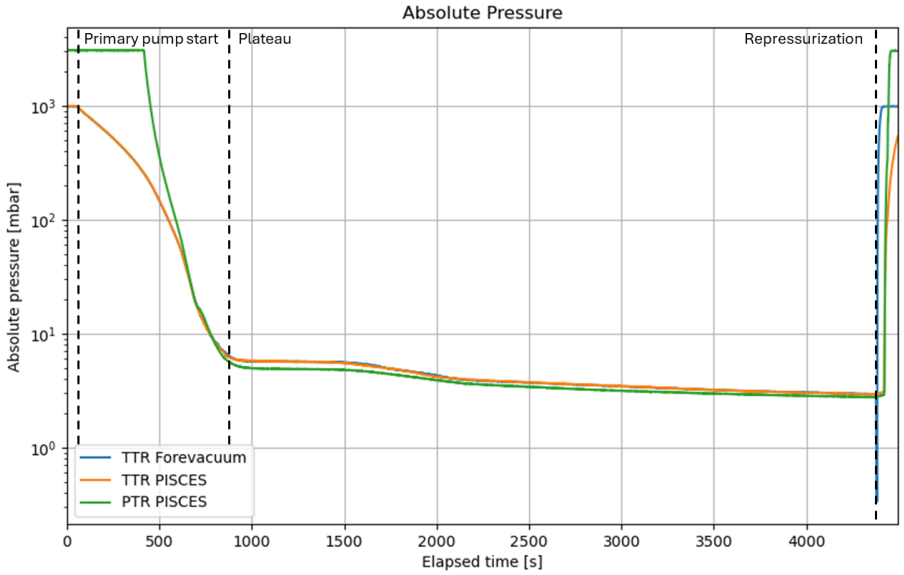

Figure 4.2: Absolute pressures in the vacuum chamber for trial 006 without the use of cryogenic pump. TTR Forevacuum records absolute pressure in the roots pump's line. TTR PISCES is used for the primary measurement of the absolute pressure in the vacuum chamber with a measurement range of 5×10^{-5} mbar to 1500 mbar. PTR PISCES also records the absolute pressure in the vacuum chamber mounted in the chamber with a measurement range of 5×10^{-9} mbar to 1000 mbar.

When cryogenic pump is employed, the absolute pressure in the vacuum chamber is reduced as shown in Figure 4.3. The pressure is seen to reduce further, as the plateau seen in Figure 4.2 at approximately 800 seconds into the elapsed time is not present in Figure 4.3. As a result, the chamber is able to reach pressures below the triple point of water, below which a phase change from solid to vapor is possible.

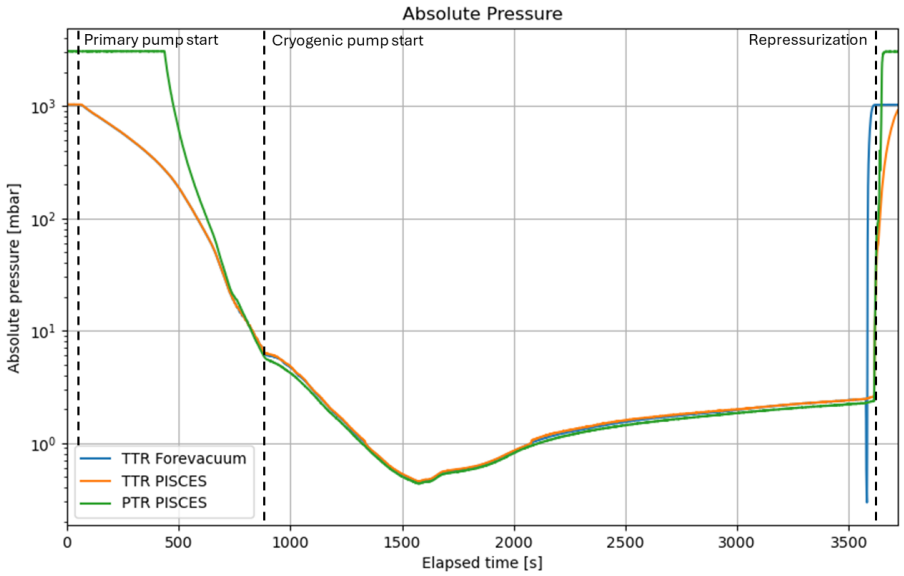

Figure 4.3: Absolute pressures in the vacuum chamber for trial 009 with the use of cryogenic pump. TTR Forevacuum records absolute pressure in the roots pump's line. TTR PISCES is used for the primary measurement of the absolute pressure in the vacuum chamber with a measurement range of 5×10^{-5} mbar to 1500 mbar. PTR PISCES also records the absolute pressure in the vacuum chamber mounted in the chamber with a measurement range of 5×10^{-9} mbar to 1000 mbar.

4.2. Plume Model

This section describes the plume model that is used to recreate the plumes. The model consists of a reservoir with liquid water recreating the subsurface ocean of Enceladus, and a channel recreating the crevasse in its ice layer. In Figure 4.1, the reservoir is visible as a transparent section of the plume model, while the channel is not visible in the figure due to the outer ice casing. As pressure in the vacuum chamber is reduced, reservoir water accelerates and travels up the channel. A simplified schematic of the setup is shown in Figure 4.4.

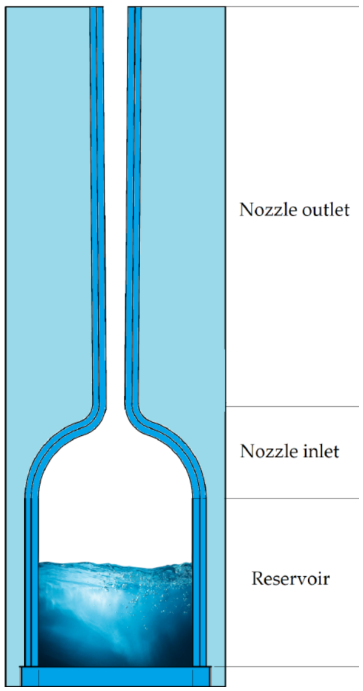

Figure 4.4: Side-view schematic of the simplified channel, using straight channel. The real setup employs a choked channel with thermocouples and pressure sensors located along several locations along the channel. Image retrieved from Sklavenitis, 2021.

It should be noted that the simplified schematic does not accurately depict the plume model, including the scale of channel geometry and the various sensors along the channel. In addition to the reservoir and channel, the channel section is cooled with ice in direct contact with the outer surface of the channel. The outer ice casing to contain the ice is visible in Figure 4.1.

4.2.1. Channel Geometry

A choked nozzle was selected for the plume model, to recreate the supersonic flow speeds as well as to increase the chances of nucleation occurring in the channel. The nozzle geometry is as defined in Table 4.1.

Table 4.1: Summary of nozzle geometry used in preliminary experiments.

Property	Value
Inlet diameter	7.98 mm
Throat diameter	5.7 mm
Outlet diameter	7.98 mm
Total length	250 mm
Inlet-throat length	50 mm
Throat-vent length	200 mm

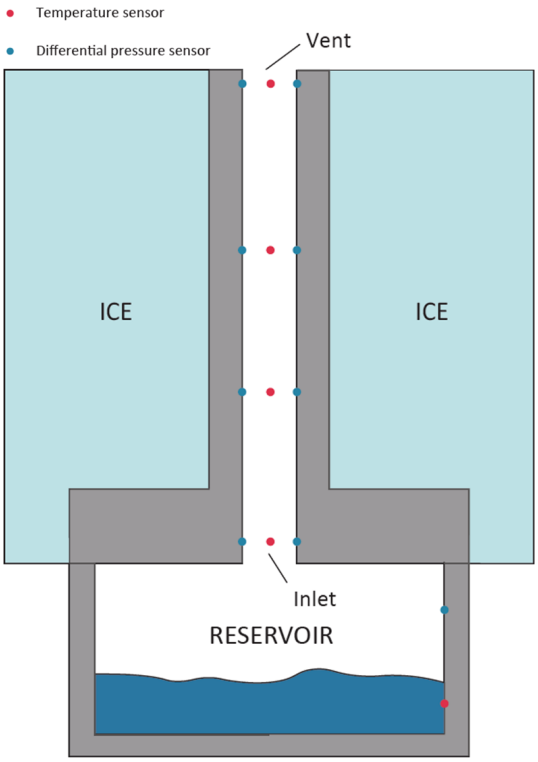

Figure 4.5: Side-view schematic of the plume model.

4.2.2. Other Plume Model Properties

The channel is 3D printed, using White Resin V4 as its material. While not shown in Figure 4.4, the channel is cooled with ice surrounding the entire nozzle section. For this baseline experiment, the ice temperature is approximately -2 $^{\circ}C$. It shall be noted that ideally the ice temperature should reach a lower temperature. It is a recommendation for future research to achieve lower levels of channel temperature, as the surface temperature on Enceladus reaches as high as -198 $^{\circ}C$ (75 K). To improve the cooling of the channel, the channel was cooled in the freezer for at least 12 hours before an experiment. Alternatively, aluminum solid coolants may be used to cool the channel.

For the baseline experiment, 800 ml of reservoir water is used. The initial volume of water was controlled such that the boiling splash does not reach the channel. When the reservoir water surface was too close to the channel, the splash droplets freezing at the channel surface has caused clogging of the channel.

4.3. Measurement Equipment

This section describes the measurement equipment used in the plume model. Temperature and differential pressure measurements along several locations along the channel are the primary measurements taken from the basic experimental setup. In addition, a Pitot probe may be situated at the vent of the channel for an accurate measurement of the vapor flow speed. The following subsections describe in detail about each measurement equipment used here.

4.3.1. Temperature Measurement

Temperature is one of the two sets of data that are collected in the experiment. The temperatures are measured at the reservoir and four locations along the channel, described as height from the inlet: 5 mm, 60 mm, 140 mm and 240 mm. Type K thermocouples with an operational temperature range of 80 K to 600 K are employed in the plume model. In Figure 4.5, a schematic drawing of the plume model including the approximate sensor location (not to scale) are shown. The thermocouple locations are indicated with red dots, placed along the centerline of the channel. The thermocouples are inserted through small holes in the plume model and secured in position using melted Tecbond 7784 polyamide.

The thermocouples are positioned within the channel so that the temperature at the center of the flow may be measured. This position is chosen to accurately measure the flow temperature, as the temperature of the channel wall surface deviates from the real flow temperature. According to Giordano, 2023, the adiabatic wall temperature is observed to be higher than the mean stream static temperature due to viscous dissipation. The obvious benefit of measuring temperature along the channel centerline rather than the wall temperature is that a recovery factor to correct for this effect is not necessary, however the presence of a thermocouple in the middle of the flow gives rise to concerns regarding the extent of intrusiveness of this sensor. This effect shall be investigated in future research.

4.3.2. Pressure Measurement

Differential pressure (i.e. difference between chamber pressure and static pressure along the channel wall) is also measured at the same locations as the temperatures. A pair of pressure sensors, one with a maximum measurement of 6 mbar and one with a maximum measurement of 12 mbar, are placed at each measurement height. For the 6 mbar sensors, the HSCDRRD006MGAA5 from Honeywell are employed, and for the 12 mbar sensors, a combination of the 5INCH-G-4V and the NPA-500B-05WG from Amphenol All/Advanced Sensors are employed. Sensors record pressures through cavities located at designated points along the channel. The sensors are powered by a 5 V supply, connected via DIN Rail distribution terminals to an NI 9201 CompactDAQ voltage input module. An averaged value is taken between the two sensors when the differential pressure values are below 6 mbar, and with values above 6 mbar, only the 12 mbar values are processed to generate the differential pressure plots. As differential pressures are measured from sensor holes located along the channel, droplet entrapment within the holes occur frequently, disturbing the measurement data. The pressure values are sampled at 100 Hz.

The static pressure P_{static} at each measurement location may be determined by adding the differential pressure measurement P_{dif} back to the chamber pressure $P_{chamber}$.

$$P_{static} = P_{dif} + P_{chamber} \tag{4.1}$$

In addition to the differential pressure sensors, absolute pressure of the vacuum chamber is also monitored. Three gauges are used for this purpose: two THERMONAC TTR 101 Transmitters (Leybold) with a pressure range of 5×10^{-5} mbar to 1500 mbar using Equation 4.2 for reading conversion, and one PENNINGVAC PTR 90 cold cathode transmitter (Leybold) with a pressure range of 5×10^{-9} mbar to 1000 mbar using Equation 4.3 for reading conversion. Here, P_{mbar} is the pressure reading in millibars and V_{out} is the output voltage of the sensor.

$$P_{mbar} = 10^{\frac{V_{out}-6.143}{1.286}} \tag{4.2}$$

$$P_{mbar} = 10^{1.667V_{out}-11.33} \tag{4.3}$$

Flow velocity through the channel may be derived using the pressure measurements. Assuming the conservation of kinetic energy and internal energy with an adiabatic flow, Equation 4.4 expressing the conservation of total enthalpy may be used (Anderson, 2002).

$$h + \frac{1}{2}V^2 = constant \tag{4.4}$$

Here, h is the specific enthalpy and V is flow velocity. Equation 4.4 can be applied to the experiment case as total enthalpy of channel inlet and vent can be assumed to be constant (neglecting the nucleation term). Assuming the flow velocity at the inlet to be zero, Equation 4.5 may be formulated.

$$c_p T_{inlet} = c_p T + \frac{1}{2}V^2 \tag{4.5}$$

Here, specific enthalpy is expressed as the product of specific heat capacity c_p and temperature T. Rearranging for flow velocity and defining specific heat capacity in terms of specific gas constant R_{sp} and heat capacity ratio γ, Equation 4.6 may be derived.

$$V = \sqrt{\frac{2\gamma}{\gamma - 1} R_{sp} T_{res} (1 - \frac{T}{T_{res}})} \tag{4.6}$$

Assuming an isentropic flow, the Poisson relations may be applied to derive Equation 4.7 to express flow velocity in pressure terms.

$$V = \sqrt{\frac{2\gamma}{\gamma - 1} R_{sp} T_{res} (1 - (\frac{P}{P_{res}})^{\frac{\gamma-1}{\gamma}})} \tag{4.7}$$

4.3.3. Pitot Probe Measurement

In addition to the flow velocities derived based on differential pressure measurements, Pitot probes are also employed to measure flow velocity at the vent. The setup employs the Kimo / Sauermann TPL-03-300T model. The Pitot tube is positioned 5 mm above the vent of the channel, measuring the both the dynamic pressure of the flow and the static pressure. The Pitot probe serves as a supplemental measurement method to acquire accurate flow speed from the experiments. Depending on the selected detection method for solid particles, the Pitot probe may not be employed as it stands in the way for the ejectiles' trajectory. The flow velocity from the Pitot tubes may be determined using Equation 4.8, with p_0 being the total pressure and p being the static pressure.

$$M = \sqrt{\frac{2}{\gamma - 1} \cdot \left[\left(\frac{p_0}{p} \right)^{\frac{\gamma-1}{\gamma}} - 1 \right]} \tag{4.8}$$

As the flow velocities from the differential pressure measurements suggest, the flow velocity is likely in the supersonic range at the vent. In this case, it is likely that a shock occurs at the vent, causing an offset from the real flow speed. This may be corrected for using Rayleigh Pitot formula as shown in Equation 4.9 (Giordano, 2023).

$$\frac{p_0}{p} = \left(\frac{(\gamma + 1)^2 M^2}{4\gamma M^2 - 2(\gamma - 1)} \right)^{\frac{\gamma}{\gamma-1}} \frac{1 - \gamma + 2\gamma M^2}{\gamma + 1} \tag{4.9}$$

5

Particle Generation Experiments

Prior to the selection process of the detection concepts, experiments were conducted with the goal of creating ice particles in the plume. As the objective of this thesis project is to develop a detection method of solid particles, the experiments conducted in this chapter first test ways to generate solid particles in the plume model. The objective of the preliminary experiments is to establish a baseline experiment in which the new detection technique is to be applied to. The consistency of the generated plumes can be examined using the temperature and pressure profile from the experiment. While the exact value of temperature and pressure may vary depending on the conditions within the laboratory as well as the weather conditions, the general shape of the curves and the relative values between different locations have been consistent from past experiments. These tendencies are described in each respective sections on temperature and differential pressure measurement in subsection 5.2.1 and subsection 4.3.2. The production of solid particles may be confirmed with 1) a visual confirmation of solid particles from the vent or in case the solid particles produced are not visible with the human naked eye, 2) an analysis of the experiment data that suggests the formation of solid particles.

5.1. Experiment Procedure

In all experiments conducted in this research, the time frame of an experiment is based on t_0, defined as the start of temperature and pressure data acquisition. The vacuum pumps are initiated approximately 1-2 minutes after t_0 for sensor calibration purposes. As described in chapter 4, pressure inside the chamber is reduced using two primary pumps and the cold finger. As chamber pressure reaches approximately 30 mbar, the boiling of reservoir is observed. During the initial boiling (approximately the first 5 minutes of boiling), measurement readings show a curve with many spikes. After some time, the boiling becomes less severe and the lines are more smooth, showing some spikes due to some large bubbles boiling in an intermittent fashion. As temperature and pressure reaches and reduces below triple point (273.16 K, 6.12 mbar), the conditions necessary for water vapor to deposit from gaseous state to solid state is achieved. The experiment is stopped when the reservoir water freezes. A detailed description of the experimental process with regard to specific measurement readings are described in each respective measurement section in section 5.2.

5.2. Baseline Experiment Results

The baseline experiment is used to determine the occurrence of nucleation in the experimental setup. The measurement of temperature and differential pressure are first evaluated. This is followed by an interpretation of the results using several nucleation parameters that may be derived from the measurements. To investigate the formation of solid particles in the baseline experiments, the measurement data were processed to derive several parameters that imply existence of solid particles.

5.2.1. Temperature

The temperature readings of a baseline experiment is as shown in Figure 5.1, with the horizontal axis showing time elapsed since t_0. The phases of the experiment are the following: boiling of the reservoir starting approximately at a chamber pressure 30 mbar, plume formation, and freezing of reservoir. The temperature is collected throughout the experiment duration. As the recording of data is initiated, a buffer time of approximately 1-2 minutes is allocated to allow for a calibration of the differential pressure sensors in data processing. As the boiling of the reservoir begins, temperature values along the channel temporarily converge towards a value between 285 K and 290 K. The temperatures then slowly decrease throughout the experiment. As the reservoir temperature approaches triple point, the reservoir water begins to freeze. As an indication of freezing, the reservoir temperature slightly increases implying an exothermic process occurring in the reservoir. Additionally, as freezing of the reservoir also ends the boiling, temperature curves would also smoothen with the reduction of erratic measurements caused by the bursting of bubbles.

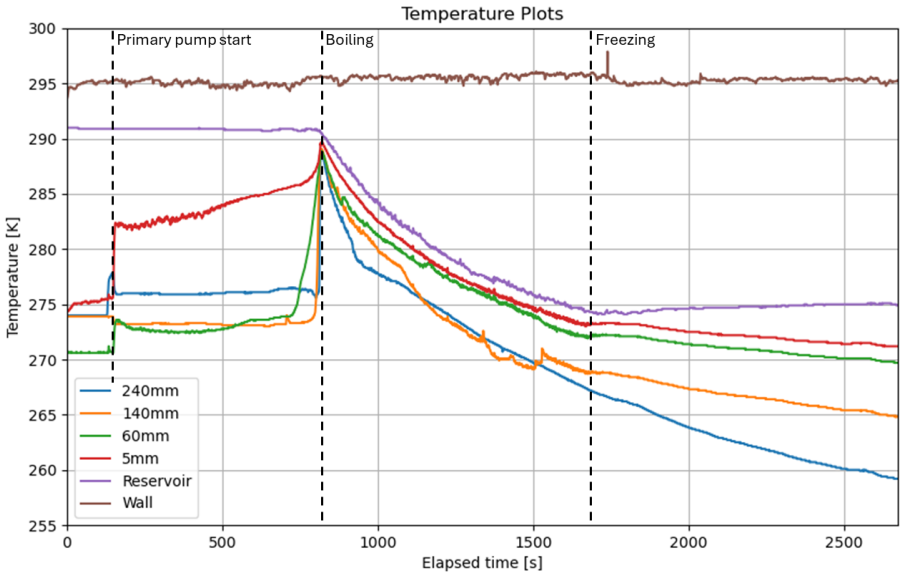

Figure 5.1: Temperature measurements of a baseline experiment. Temperatures are measured at several locations along the channel, with the height from the channel inlet indicated in the plot legend. 'Wall' temperature measures the room temperature.

Average temperatures from four baseline experiments are shown in Figure 5.2. Here, the error bars show the value of one standard deviation from the mean value. This plot only shows the average temperatures after the boiling point for each experiment. This is because boiling starts at different times for each experiment, and therefore the times are aligned at the boiling point. This plot shows the general decreasing trend of temperature along the channel after boiling starts, and the tendency for temperatures further from the reservoir to be of lower values.

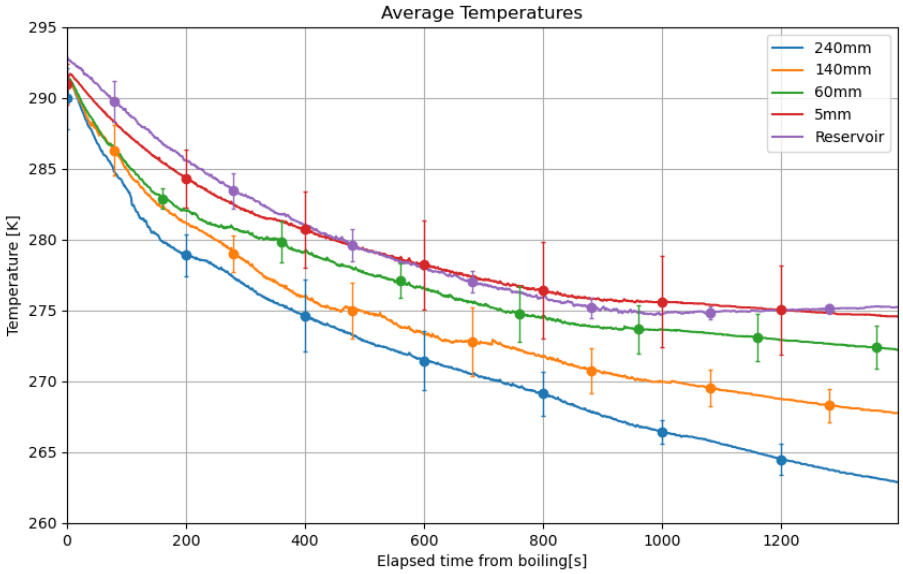

Figure 5.2: Average temperature measurements from 4 baseline experiments. The time scaled is aligned with the boiling time of each experiment. Error bars show the range of one standard deviation from the average value. Temperatures are measured at several locations along the channel, with the height from the channel inlet indicated in the plot legend.

The temperature difference along the length of the channel provides an indication of the flow within the channel. The temperature tends to decrease for locations further away from the inlet. This tendency can be explained as an acceleration of flow in the channel, as thermal energy is transferred to kinetic energy of the flow. As indicated in the experimental setup, the channel employs a choked geometry, in which a supersonic flow may be expected downstream of the throat. A detailed analysis of flow speed is presented in subsection 5.2.4.

5.2.2. Pressure

Differential pressure here is defined as the difference between chamber pressure and static pressure at the measurement location. Like the temperature plots, the differential pressures measured at several locations are plotted against the elapsed time since t_0. As the raw differential pressure measurement has a slight offset from 0, the first few minutes of the measurement is used to calibrate this offset in the post processing. During this time, the differential pressure value settles and flattens, at which this offset value is corrected and calibrated as 0 mbar. Figure 5.3 shows the calibrated differential pressure measurements from a baseline experiment.

As air is evacuated from the chamber and boiling starts, the flow of water vapor is seen to begin as differential pressure shows a steep increase. Boiling is observed to be the most intense in the first few minutes after it has started, and during this phase, the differential pressure measurements near the reservoir shows a high value, while those for locations higher up in the channel indicate lower values. It is worth noting that condensation along the walls of the channel occasionally cause disturbances in the measurement of pressures due to entrapment of water droplets in the sensor holes. After the initial boiling, differential pressure near the reservoir decrease, while those near the vent increase. As the reservoir water freezes over, all differential pressure curves show some increase before settling on a linearly decreasing curve.

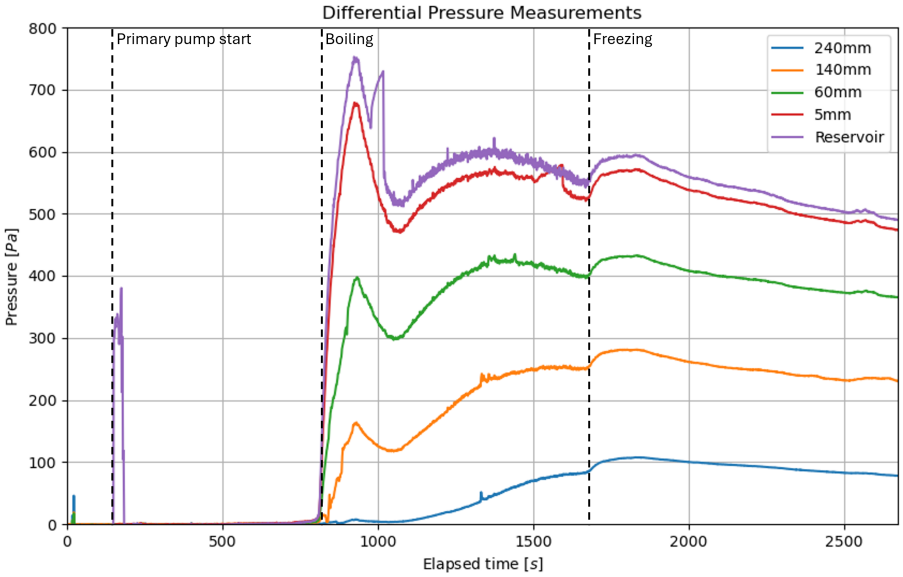

Figure 5.3: Pressure measurements of a baseline experiment. Pressures are measured at several locations along the channel, with the height from the channel inlet indicated in the plot legend.

Average differential pressures at each measurement location from four baseline experiments are shown in Figure 5.5. Here, the similar trend of lower locations showing higher differential pressure values are observed. It shall be noted that the differential pressure curves for different experiments do not always follow a similar shaped curve for several reasons. As mentioned already, condensation building up on the channel wall occasionally cause clogging of the sensor holes, causing disturbances in the measurements. Moreover, the performance of the primary pumps may be inconsistent depending on operation of the pump prior to the experiment. Figure 5.4 shows a comparison of absolute pressures between two tests. In Figure 5.4a, a minimum pressure of 45.75 Pa is reached, whereas in Figure 5.4b a minimum pressure of 26.39 Pa is reached.

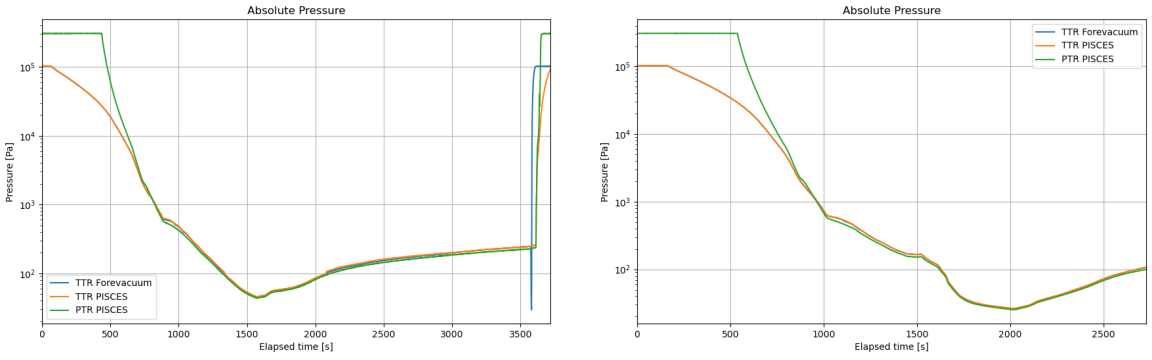

(a) Absolute pressures in the vacuum chamber for test 009.

(b) Absolute pressures in the vacuum chamber for test 011.

Figure 5.4: Comparison of absolute pressures in the vacuum chamber between test 009 and test 011. TTR Forevacuum records absolute pressure in the roots pump's line. TTR PISCES is used as the primary measurement of the absolute pressure in the vacuum chamber with a measurement range of 5×10^{-5} mbar to 1500 mbar. PTR PISCES also records the absolute pressure in the vacuum chamber mounted in the chamber with a measurement range of 5×10^{-9} mbar to 1000 mbar.

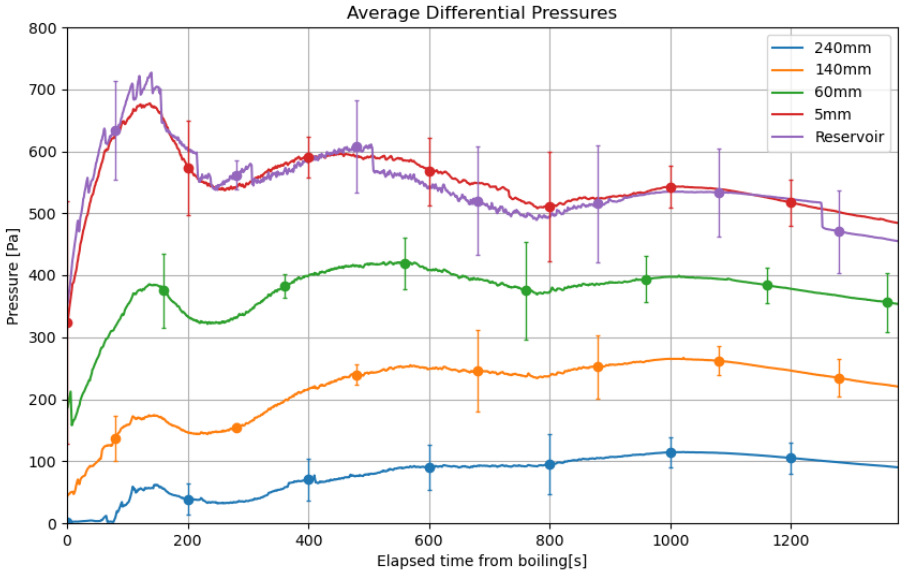

Figure 5.5: Average differential pressure measurements from 4 baseline experiments. Time scale of each measurement is aligned based on the start of boiling. Error bars are show one standard deviation from the average value. Differential pressures are measured at several locations along the channel, with the height from the channel inlet indicated in the plot legend.

The static pressure at each measurement location may be determined by adding the differential pressure measurement with the chamber pressure. This is shown in Equation 4.1. As a result, the static pressures for the baseline case are as shown in Figure 5.6.

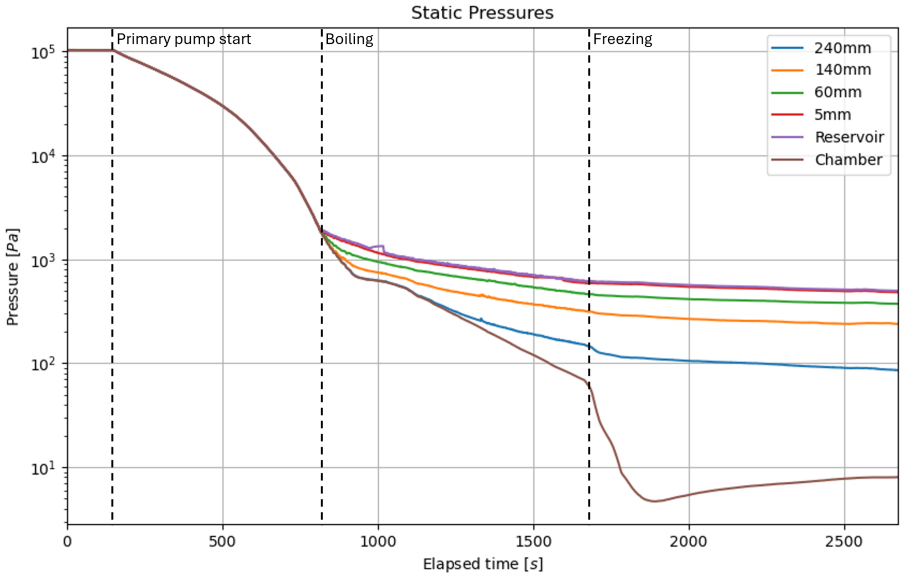

Figure 5.6: Static pressure plot of a baseline experiment. Pressures are measured at several locations along the channel, with the height from the channel inlet indicated in the plot legend.

Average velocity at each measurement location from four baseline experiments are shown in Figure 5.10.

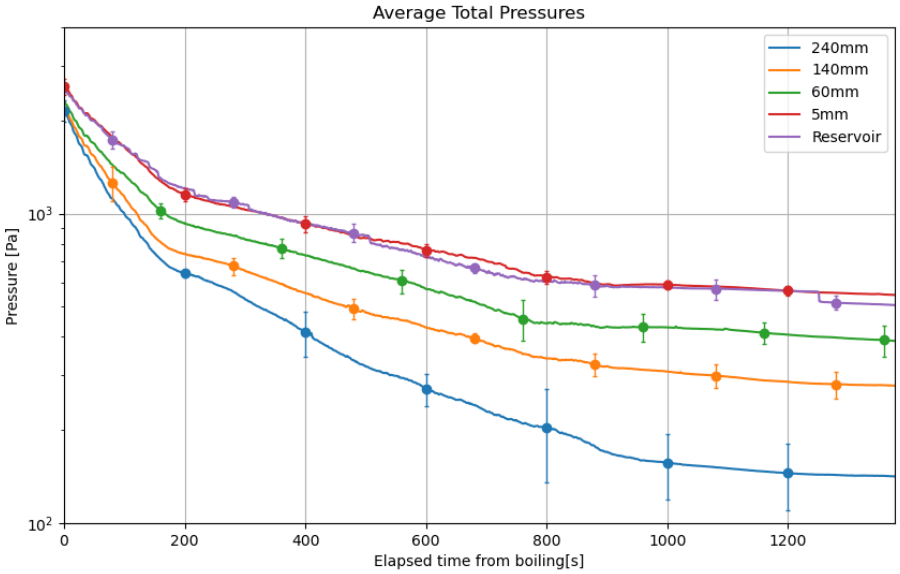

Figure 5.7: Average static pressure measurements from 4 baseline experiments. Time scale of each measurement is aligned based on the start of boiling. Error bars are show one standard deviation from the average value. Pressures are computed for each measurement locations along the channel, with the height from the channel inlet indicated in the plot legend.

5.2.3. Pressure-Temperature Relations

The temperature and pressure measurements were plotted onto a phase diagram of water to show the thermodynamic state of the flow. Again, the measurements for each location along the channel are plotted. The dashed lines in the plot show the phase transition curves (sublimation curve, vaporization curve and fusion curve). Time stamps are added to the plot to show the notable event points during the experiment. The PT curves all begin at the top of the graph, and as the reservoir starts to boil, the curves connect at its highest temperature throughout the experiment. After this point, pressure and temperature decrease, following the sublimation curve. As pressure and temperatures decrease, some deviations can be seen for measurements close to the vent. The 240 mm and 140 mm sensors measurements are seen to deviate towards a higher temperature compared to the reservoir and the 5 mm measurements. This tendency may be attributed to nucleation in the channel, as nucleation from vapor to solid particles is an exothermic process, therefore shifting the curve towards the higher temperature direction than it would without nucleation occurring.

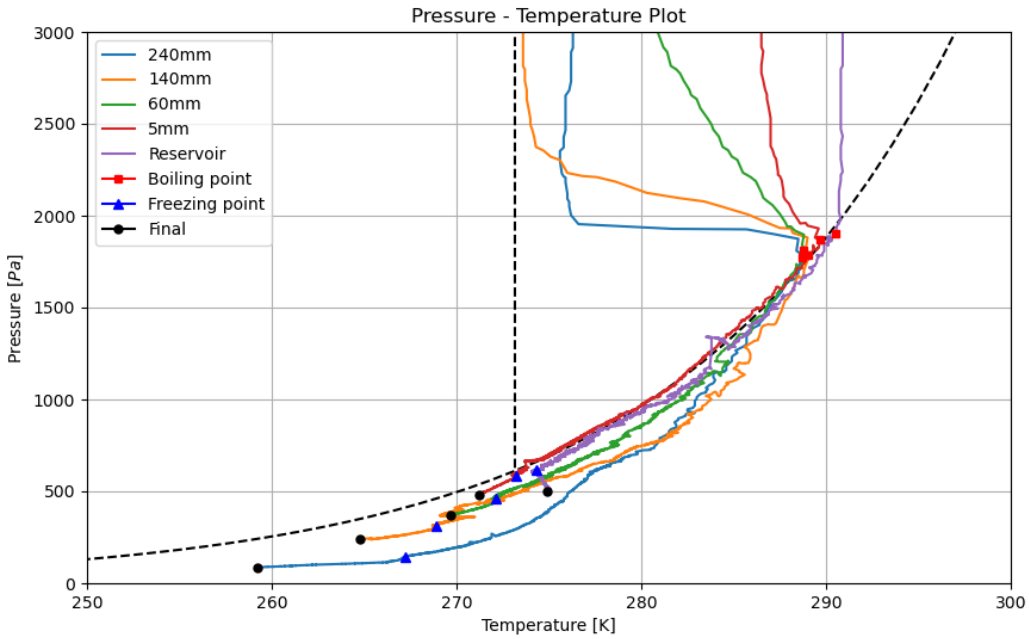

Figure 5.8: Plot showing the pressure and temperature at five measurement points in a baseline experiment. The dotted line shows the phase transition curves.

5.2.4. Flow Velocity

The velocity profile of a baseline experiment is as shown in Figure 5.9. Velocities at each measurement location are shown. As mentioned, the flow velocity at the reservoir is assumed to be zero.

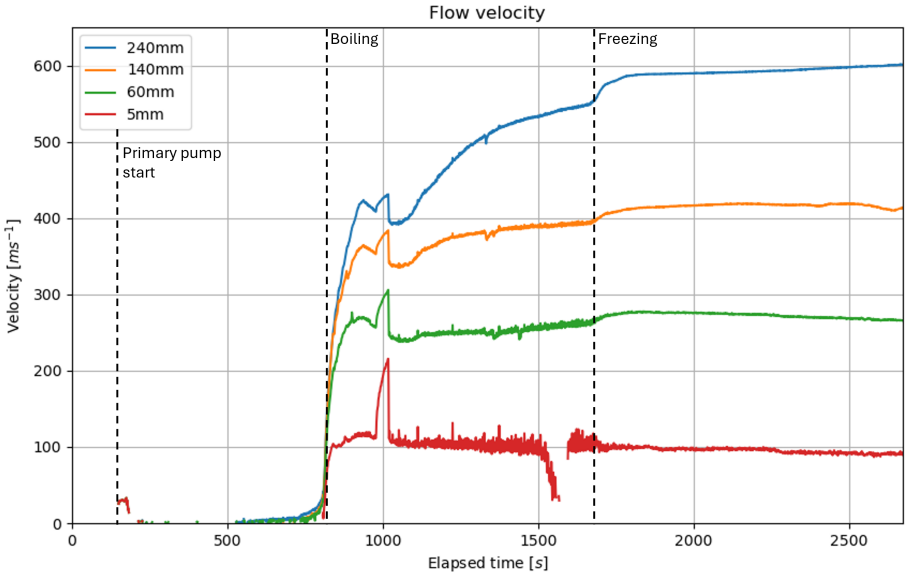

Figure 5.9: Plot showing the flow velocity at five measurement points in a baseline experiment.

Average velocities at 60 mm, 140 mm and 240 mm from four baseline experiments are shown in Figure 5.10. As shown in Equation 4.7, computation of velocity is dependent on the ratio of pressure

between the measurement location and reservoir. As it may be seen in Figure 5.7, pressure between 5 mm and reservoir cross over with each other for much of the measurement. As a result, velocity at 5 mm are computed to be close to 0 for bulk of the measurement time. Thus, the 5 mm velocity is not included in the figure.

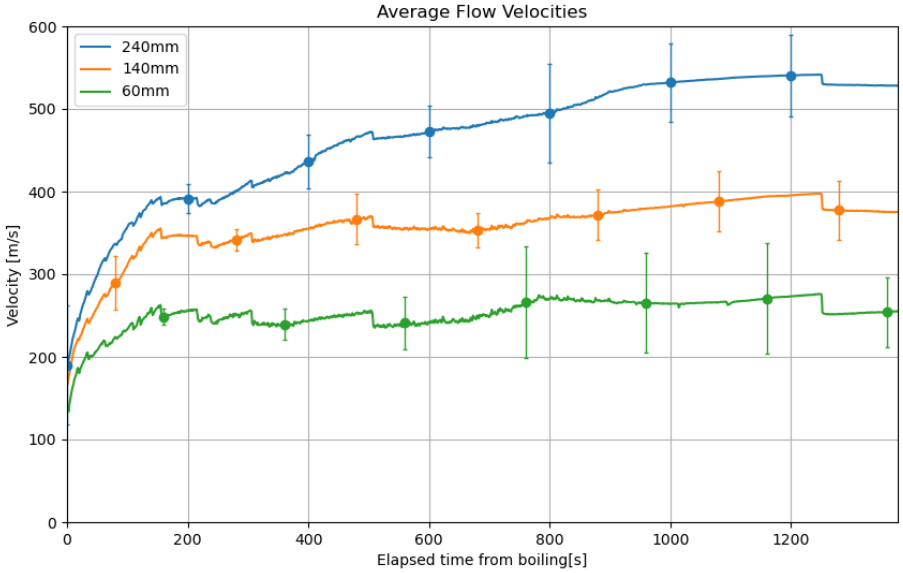

Figure 5.10: Average velocity measurements from 4 baseline experiments. Time scale of each measurement is aligned based on the start of boiling. Error bars are show one standard deviation from the average value. Velocities are computed for several locations along the channel, with the height from the channel inlet indicated in the plot legend.

As suggested from the temperature readings in subsection 5.2.1, both Figure 5.9 and Figure 5.10 show an acceleration of the flow throughout the channel. According to the differential pressure measurements, the near-vent flow velocity reaches 542 m/s (Mach 1.34) at its maximum on average.

In addition to the flow velocities derived based on differential pressure measurements, Pitot probes are also employed to measure flow velocity at the vent. As mentioned in subsection 4.3.3, the flow velocity is likely in the supersonic range at the vent, and this results in a difference between the real flow speed and the flow speed derived using Equation 4.8, due to a shock occurring at the vent. This is corrected for using Rayleigh Pitot formula as shown in Equation 4.9. A comparison of Mach numbers derived from 240 mm pressure measurements, isentropic flow (using Pitot probe measurement and Equation 4.8), and Rayleigh Pitot formula Equation 4.9 are shown in Figure 5.11.

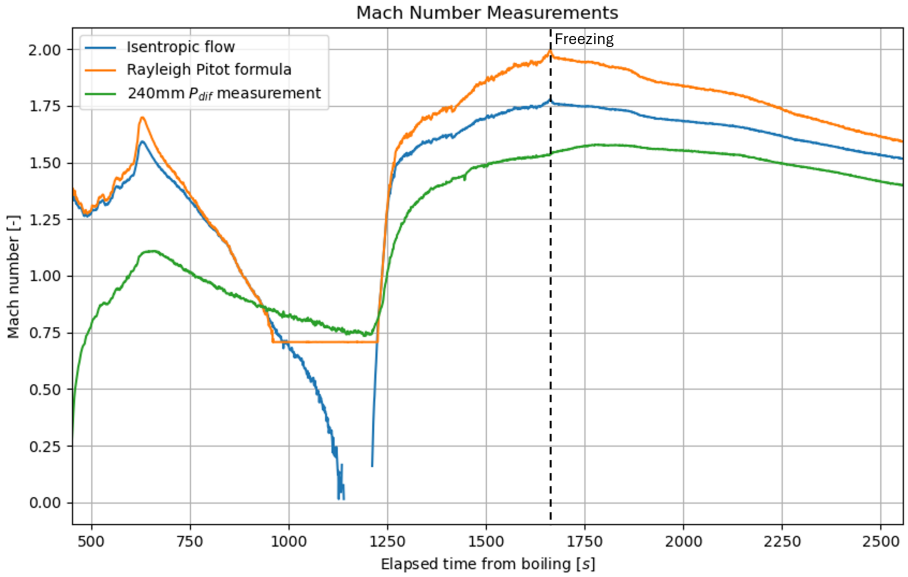

Figure 5.11: A comparison of Mach numbers showing values derived from Equation 4.8 assuming isentropic flow (blue), Equation 4.9 accounting for shock at vent (orange), and Equation 4.7 using differential pressure measurement at 240 mm.

Several notable differences may be seen between the three methods. Equation 4.9 yields the highest flow velocity, reaching Mach 2.0 at its maximum. The isentropic flow formula shows flow velocity just below the Rayleigh Pitot formula. Meanwhile, the 240 mm differential pressure measurement shows the lowest flow velocity, as expected considering that the measurement location for this plot is below the vent.

5.2.5. Saturation

Saturation degree may be derived and used to examine the condition within the channel in relation to sustaining phase change. Saturation degree S is defined as the ratio of water vapor pressure p_{gas} to the saturated vapor pressure $p_{eq}^{l.g.}(T_{gas})$. Equation 5.1 is used to determine saturation degree (Schmidt et al., 2008).

$$S = \frac{p_{gas}}{p_{eq}^{l.g.}(T_{gas})} \tag{5.1}$$

To determine the saturated vapor pressure, the Antoine equation as shown in Equation 5.2 is used (Stull, 1947).

$$p_{eq} = 10^{A - \frac{B}{C + T_{flow}}} \tag{5.2}$$

Here, T_{flow} is the flow temperature, and a set of constants derived from empirical relations based on the studies of Stull, 1947 are employed. The values used here are shown in Table 5.1.

Table 5.1: Summary of constants used in Antoine equation, calculated by NIST based on the study of Stull, 1947.

Constant	Value
A	4.6543
B	1435.264
C	-64.848

Figure 5.12 shows the saturation degree of a baseline experiment. A state in which S > 1 is referred to a supersaturated state. A supersaturated state enables nucleation to occur. Thus, the saturation degree is illustrated to show the times at which flow is saturated enough for nucleation to occur.

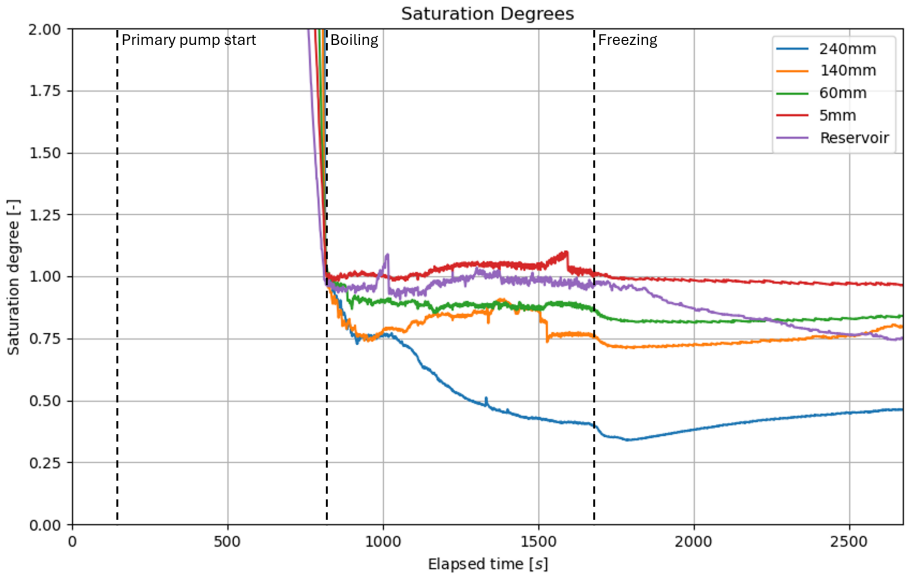

Figure 5.12: Plot showing the saturation degree at five measurement points in a baseline experiment.

Average saturation degree at each measurement location from four baseline experiments are shown in Figure 5.13. Here, time scale from each experiment is aligned with boiling time, and are thus plotted starting at this time.

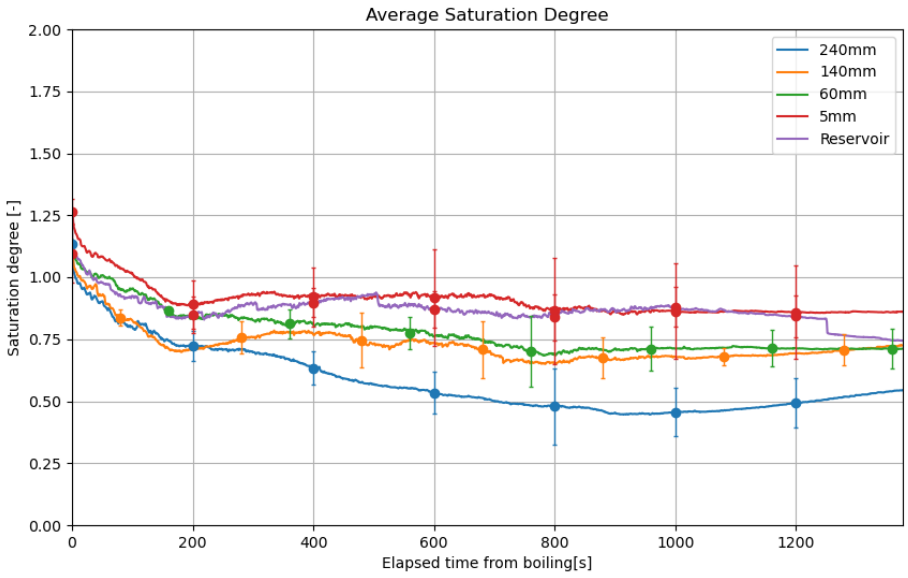

Figure 5.13: Average saturation degree measurements from 4 baseline experiments. Time scale of each measurement is aligned based on the start of boiling. Error bars are show one standard deviation from the average value. Saturation degree are computed for each measurement locations along the channel, with the height from the channel inlet indicated in the plot legend.

In the baseline experiments, saturation degree in the reservoir and at 5 mm stays near the S = 1 level. In Figure 5.12, readings from both locations stay at this level until freezing of the reservoir. After freezing starts, the reservoir saturation degree shows a steady decrease, with the 5 mm value also decreasing but to a lesser extent. For other locations along the channel, the saturation degree are of relatively lower values.

Under isentropic expansion, the expansion of flow leads to a decrease in the flow temperature, resulting in the reduction of saturated vapor pressure, as highlighted in Equation 5.2. This would lead to a very high value of saturation degree. On the other hand, the baseline experiment results have shown saturation degree of approximately 1. Experimental research by Giordano, 2023 also acquires saturation degree values of similar order. Moreover, Giordano, 2023 also explains the difference between the isentropic flow and the experimental model. Vapor at a pressure above the saturated pressure changes phase, and as a result, the saturation degree stays at a value near 1. Thus, a saturation degree of near 1 gives rise to the possibility of nucleation occurring in the channel.

5.2.6. Mass Flow

Using the principle of mass conservation as shown in Equation 5.3, the mass flow rate may be derived by substituting Equation 4.7 for flow velocity.

$$\frac{d}{dz}(\rho V A) = 0 \tag{5.3}$$

As a result, Equation 5.4 may be derived to determine mass flow rate $\dot{m}$.

$$\dot{m} = \frac{p_0 A}{\sqrt{R_{sp}} T_0} \sqrt{\frac{2\gamma}{\gamma - 1} \left(\frac{p}{p_0}\right)^{\frac{2}{\gamma}} \left(1 - \left(\frac{p}{p_0}\right)^{\frac{\gamma-1}{\gamma}}\right)} \tag{5.4}$$

Using Equation 5.4, the mass flow rate for a baseline experiment is determined to be as shown in Figure 5.14.

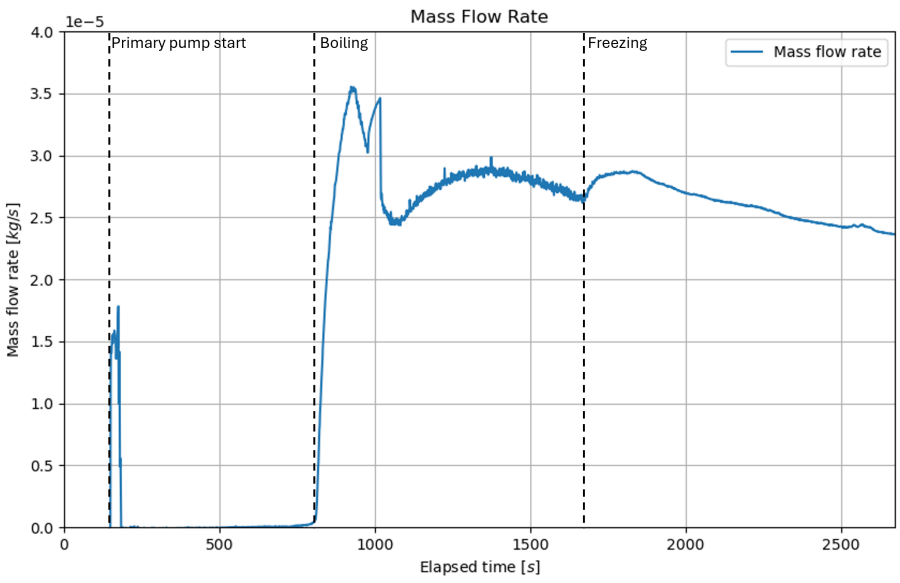

Figure 5.14: Plot showing the total mass flow in a baseline experiment.

The total mass ejected from throughout the experiment may be determine by integrated the mass flow curve with time. For this particular baseline experiment trial, the total mass ejected was estimated to be 49.6 grams.

5.2.7. Solid Fraction

Solid fraction f is defined as the proportion of solid particles ejected from the channel of all mass ejected as obtained in the previous section. Solid fraction may be determined using the enthalpy difference between the vent and the inlet Δh_{vent}, as determined using Equation 5.5. Assuming that the flow velocity is 0 at the inlet, the enthalpy at the inlet may be equal to the sum of internal energy at the vent, the velocity component and the enthalpy of nucleation. Here, $c_{p,inlet}$ is the specific heat capacity at inlet, $c_{p,vent}$ is the specific heat capacity at vent, T_{inlet} is the flow temperature at inlet, T_{vent} is the flow temperature at vent and V_{vent} is the flow velocity at the vent.

$$c_{p,\,\text{inlet}}\, T_{\text{inlet}} = c_{p,\,\text{vent}}\, T_{\text{vent}} + \frac{V_{\text{vent}}^2}{2} - \Delta h_{\text{vent}} \tag{5.5}$$

Solid fraction may be determined as the fraction of this enthalpy difference and latent heat of fusion L_v. This is shown in Equation 5.6.

$$f = \frac{\Delta h_{vent}}{L_v} \tag{5.6}$$

As a result, the solid fraction throughout the experiment may be plotted as in Figure 5.15.

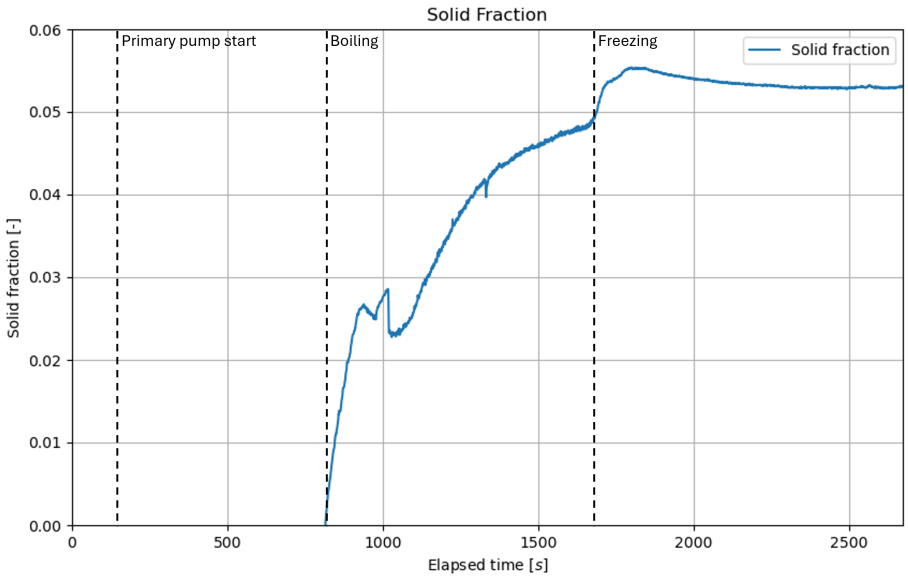

Figure 5.15: Plot showing the solid fraction in a baseline experiment.

Solid fraction increases as the boiling starts, and continues to increase throughout the boiling. It reaches a value over 0.05, just as the freezing of the reservoir begins. After the freezing, it follows a more constant value, just lower than the maximum value.

Using the obtained solid fraction value, the total solid mass ejected can be determined. With the solid fraction value multiplied to the mass flow rate, the solid mass flow rate may be plotted. The total solid mass ejected is determined by integrating this plot with time. The total solid particle mass flow is shown in Figure 5.16.

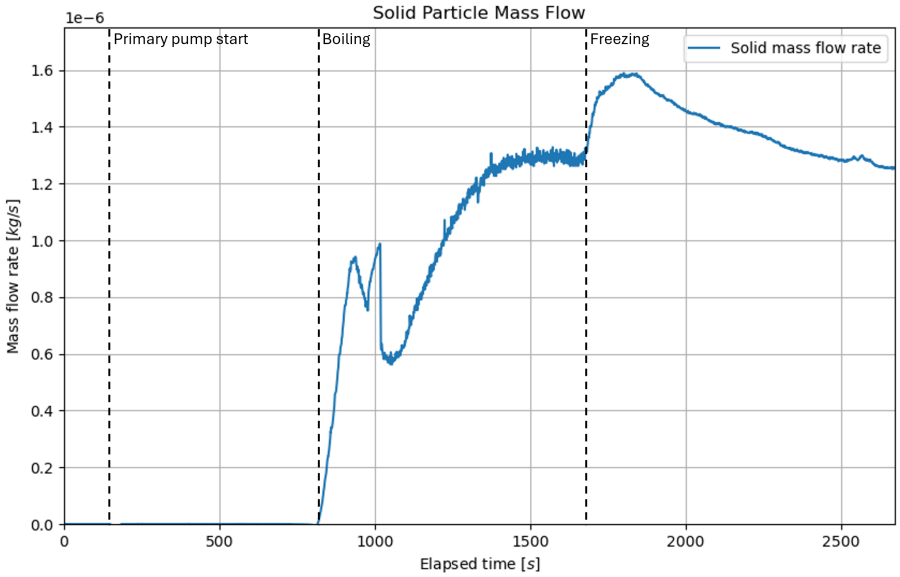

Figure 5.16: Plot showing the solid particle mass flow in a baseline experiment.

Using the solid flow curve, the total solid mass ejected for this particular experiment is estimated to be 2.2 grams.

5.3. Simulation Results on Particle Formation and Growth

Along with the experimental investigation of solid particle formation, a computational investigation was conducted by modeling the experimental setup in a computational simulation, based on the works of Fontes, 2023 and Scholts, 2025. A fully multi-phase, multidimensional model for condensation and grain dynamics phenomena was used to recreate a simulation of the plume model. Using the geometries of the physical plume model, the computational model serves as a comparison of the plume theories and the experimental results. A mesh was created using Gmsh with the same geometry as baseline experiment, as described in subsection 4.2.1. To save on computational time, the channel geometry was cut in half. The simulation does not include wall accretion or wall sublimation and only phase change within the flow itself. In this simulation, the static pressure is defined at the inlet close to triple point with the temperature at 273 K. The temperature and pressure throughout the channel and all other variable are determined by the flow physics. Figure 5.17 presents the Mach number, temperature T, pressure P and the density of the vapor flow ρ. Figure 5.18 shows several nucleation parameters of this channel: nucleation rate J, particle number N, saturation degree S_{sat}, solid fraction f, particle growth rate dr/dt, and grain radius r_{grain} are presented here. Nucleation rate indicates the amount of particles that are produced in a given time, with particle number being the total amount of particles. Particle growth rate indicates the rate at which the radius of the grain grows per unit time, and particle radius plot shows the radius of the particles at a given location. For parameters that are also acquired in the experimental model, the results are overlaid onto the simulation results shown as red points.

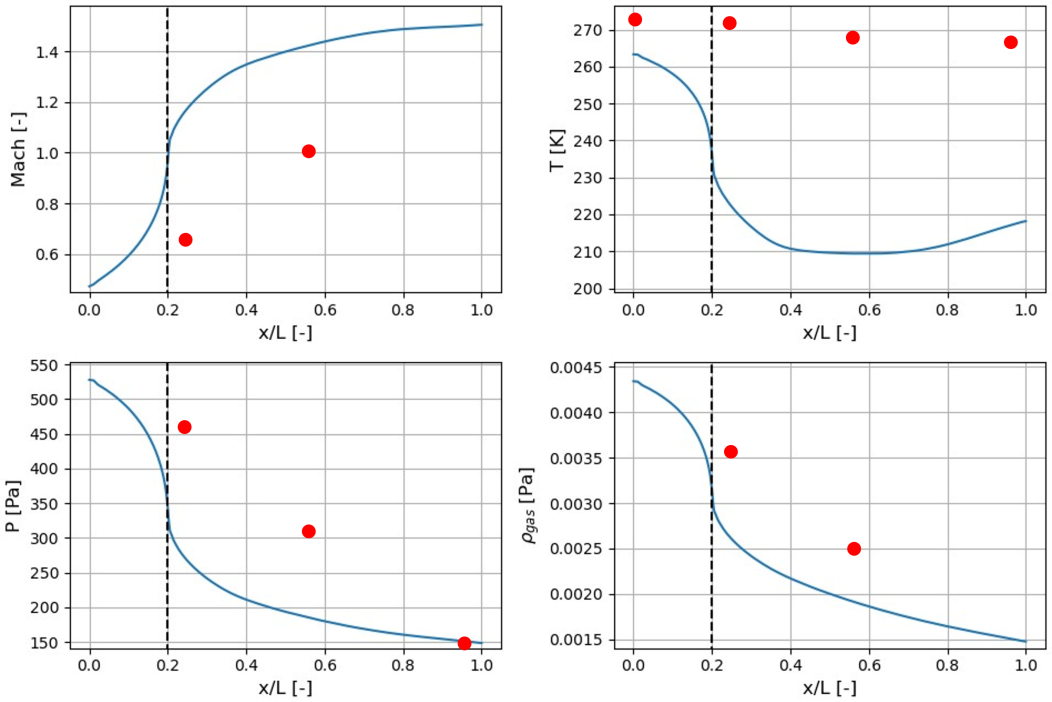

Figure 5.17: Simulation results showing the basic parameters of the channel model.

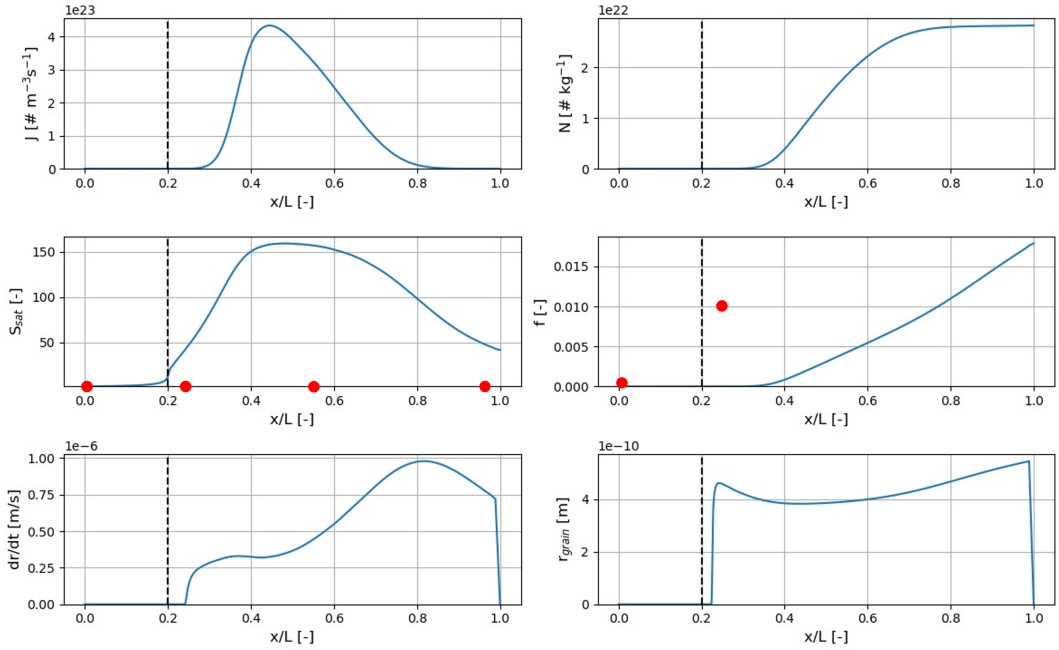

Figure 5.18: Simulation results showing the nucleation parameters of the channel model.

Here, the dotted line indicates the throat location. Mach number shows a sharp increase just after the throat, reaching over Mach 1.4 at the vent. Conversely, temperature of the channel reduces sharply from the throat, and shows a slight increase towards the vent. This slight increase may be interpreted as due to boundary conditions at the vent. Pressure and density decreases towards the vent in a similar manner.

Nucleation rate shows a peak just after three-fifth up the channel, before reducing back to 0. Saturation degree S_{sat} shows a similar peak, but on a much broader length range. Solid fraction f shows a gradual increase starting after the throat and rising up close to 0.02. Particle growth rate $\frac{dr}{dt}$ describes the rate at which nucleated particles grow in radius, with particle radius r_{grain} showing its size at each location. Growth rate shows its first increase just after the throat and peaks out at approximately four-fifth of the way up the channel. From the growth rate, the particle radius may be determined to be in the order of $10^{-10}m$ scale.

5.3.1. Conclusion on solid particle formation in baseline experiment

The results from the preliminary investigation, including both the experimental and simulation models, indicate several possibilities of nucleation occurring in the channel. Namely, the deviation of the pressure-temperature curve, the computed solid fraction and the saturation degree at the inlet suggest that the conditions to generate solid particles are established in the baseline experiment. However, while the simulation results also suggest the similar results, the size of the particles are suggested to be in the nanometer scale.

6

Selection of Detection System

This chapter presents the trade-off phase for the selection of the detection system to be employed for the purpose of this research. This chapter first examines the performance requirements that the detection system should adhere to. An appropriate set of criteria and weights are given prior to conducting the trade-off. Based on the final scores of the trade-off, a selection of the detection system is made.

A solution to detect plume particles' speed and size may be developed based on the results of the preliminary experiments. To summarize the findings from the baseline experiments, although there were no visual confirmation of particles in the visible sizes (down to 10 μm scale), there were indications of solid particles being generated, based on the computed solid fraction and the pressure-temperature conditions inside the channel. Moreover, simulation results have shown the probable ranges of nucleation rate and particle growth rate, which were derived to show the number of particles around the vent to be in the 10^{22} range and the particle diameter to be in the 10^{-9} range. Based on these results, a detection method to detect ice particles in the nanometer range traveling at speeds close to the flow velocities at the vent are developed.

6.1. Trade-off Method Description

The trade-off process begins with the review of the solid particle profile that is expected to be observed from the plume model. This helps to generate a list of trade-off criteria in which the detection system should adhere to. While the profile of particles generated here is an estimate of the particle profile and not a definitive technical requirement, it is used to deduce the properties of particles crucial to construct the detection system.

Based on the deduced particle profile as well as other factors constraining the detection system, the trade-off criteria are established. Moreover, weights are given to each criteria based on the relative importance of each criterion with another. Finally, the score boundaries are given to each criterion. The grading scale is based on three levels: good (2 points), satisfactory (1 point), and bad (0 point). The specific score levels and boundaries are elaborated in the section of each criterion.

6.2. Solid particle profile

The size of the particles generated from nucleation are estimated to be reaching 1 nm, as derived from the plume simulation in section 5.3. With this size of solid particles, the velocity of the solid particles is assumed to be coupled with the water vapor flow speed, reaching Mach 2.0 at its maximum. The mass flow of the solid particles $\dot{m}$, determined using the total mass flow and the solid fraction of the flow, is estimated to be $1.6 \times 10^{-6} kg/s$. Using this mass flow, the force due to the solid particles F_{solid} may be derived as the product of mass flow and velocity V_{solid}.

$$F_{solid} = \dot{m}_{solid} V_{solid} \tag{6.1}$$

Using the aforementioned values of mass flow and velocity, the bulk force attributed to solid particles is estimated to be $1.12 \times 10^{-3}N$. The force exerted by a single particle may be inferred using an estimate of the number of particles ejected per time n_{solid}. The simulation results in Figure 5.17 show an indication of the number of particle per mass of solid particles ejected N. By multiplying this value with the mass flow rate of solid particle as shown in Figure 5.16, the number of particles ejected per time n_{solid} may be estimated. This is shown in Equation 6.2.

$$n_{solid} = N\dot{m}_{solid} \tag{6.2}$$

Assuming a particle per mass of $10^{22}/kg$ and a solid mass flow of $1.6 \times 10^{-6}kg/s$, the number of particle ejected per time may be estimated to be $1.6 \times 10^{16}/s$. Using this particle number, the force exerted by an individual particle $F_{i,solid}$ may be determined as shown in Equation 6.3.

$$F_{i,solid} = \frac{F_{solid}}{n_{solid}} \tag{6.3}$$

As a result, the force exerted by an individual particle is determined to be $7.5 \times 10^{-20}N$.

As mentioned previously, the force attributed to vapor flow must be offset from the raw measurement. This force due to vapor flow F_{vapor} may be determined using the mass flow of vapor $\dot{m}_{vapor}$ and the flow velocity of vapor V_{vapor}. The force is simply determined as a product of the two, as shown in Equation 6.4.

$$F_{vapor} = \dot{m}_{vapor}V_{vapor} \tag{6.4}$$

An estimate of this force may be determined from the Pitot tube measurements. Using a vapor mass flow of $2.85 \times 10^{-5}kg/s$ and a flow speed of $800m/s$, a vapor flow force of $0.0228N$ may be expected. It shall be noted that the vapor flow force to be offset in the experiments will use measurements values from the 240 mm sensors as the Pitot probe may not be placed with the setup for particle detection.

6.2.1. Splash Droplet Particles

On the other hand, solid particles may also be generated due to freezing of the liquid droplets. Intense boiling has been observed after the initial boiling of the reservoir. This produces liquid droplets in the channel, that can freeze as it travels up the channel or collides with the channel wall. Moreover, it was also observed that the splashing droplets that freeze in the channel can cause clogging of the channel.

Weber number We may be used to estimate the size of droplets and ultimately the size of the solid particle after freezing. Weber number is an indicator of the relative significance between a fluid's inertial force and surface tension force (source). The Weber number may be expressed in terms of the fluid's density ρ, velocity v, droplet diameter d and surface tension σ. Equation 6.5 shows the expression of Weber number using those terms.

$$We = \frac{\rho v^2 d}{\sigma} \tag{6.5}$$

When boiling occurs, Weber number may be assumed to be equal to 1, as it is at the critical point in which the fluid's inertial force and surface tension force are in balance. When the reservoir is assumed to be at room temperature conditions ($\rho = 998.29kg/m^3$, $\sigma = 0.0728N/m$) with a splash speed of 1 m/s (source) and using an ice density of 999.77 kg/m^3, the particle diameter is estimated to be 73 μm. This is the particle size when the droplet is first formed, and it does not consider the growth in size as it travels up the channel.

A summarized table of the particle profile is shown in Table 6.1.

Table 6.1: Summary of expected particle profile.

Parameter	Value
Velocity	Mach 2.0
Size (nucleation particles)	1 nm
Size (splash droplets)	73 μ m
Mass flow	1.6×10^{-6} kg/s
Solid particle force	1.12×10^{-3} N
Vapor flow force	2.28×10^{-2} N

6.2.2. Additional requirements

Some additional requirements that constrain the detection system are stated in this section.

Size

The size of the detection system shall be able to fit within the vacuum chamber. The vacuum chamber is a cubic chamber with dimensions of 80 cm on each side, taking up a volume of 512 L. Moreover, a cold finger is situated on the far end left hand side corner of the vacuum chamber. The detection system shall also avoid contact with this cold finger as it is a crucial component in reducing the pressure within the chamber to a sufficient level.

Vacuum resistance

Any apparatus that must be placed within the vacuum chamber shall be resistant to low pressures of below 1 mbar. Any instrumentation that must be placed outside the vacuum chamber shall be able to be connected via the feed through.

6.3. Selection Criteria

Several selection criteria are derived to select the most appropriate detection method for this application. The detection method will be evaluated with respect to the following criteria.

Table 6.2: List of tradeoff criteria.

Code	Criterion	Weight
001	Size measurement	3
002	Velocity measurement	2
003	Individual detection	3
004	Cost	1
005	Ease of construction	1

001 - Size measurement

This criterion is directly related to the main research purpose of characterizing the solid particles that are ejected from the experimental plume model. As noted in section 6.2, the estimated size of nucleation particles is in the nanometer-range, and the estimated size of splash particles is in the micrometer-range. While the exact capability of the chosen detection system needs to be determined in the experimental setup, the size estimation serves as a general guide for which the size measurement system shall be able to detect. A ”good” score is awarded to systems with the full capacity to measure the sizes of the particles, a ”satisfactory” score is awarded to systems that can measure the sizes of particles but with some limitations, such as a minimum detectable size of above the estimated sizes, and a ”bad” score is awarded to systems that cannot measure particle sizes. Since capability to measure size is a crucial function of the detection system, it is given a criterion weight of 3 which is the highest in this trade-off.

002 - Velocity measurement

This criterion also serves the main research purpose of characterizing the plume particles. An estimation of the particle velocity are also given in section 6.2. Like the size measurement criterion, a ”good”

score is awarded to systems with the full capacity to measure particle velocity, a ”satisfactory” score is awarded to systems with the capacity to measure particle velocity with some limitations, and a ”bad” score is awarded to systems without the capability of measuring particle velocity. This criterion is given a weight of 2. This is because the baseline experiment has already shown an indication of the general speed at which the particles would travel. Especially for small particles, it is expected that the particles are coupled to the vapor flow velocity. Thus, the relative significance of particle velocity detection is lower than that of the size measurement detection.

003 - Individual particle detection

While some detection systems may detect the presence of solid particles as a bulk, it is essential for the purpose of this research that sizes of individual particles are determined. The expected number of particles released per second from nucleation is in the order of 10^{16}. This number was determined based on the particle number per mass of solid ejected (as shown in Figure 5.17) and the solid mass flow from preliminary experiments. While this number is a simulation estimate of the particle number and not an measured value from the baseline experiments, it nonetheless serves as a metric suggesting that particle numbers of such high value may be expected. For this criterion, a ”good” score is awarded to systems with the full capability to individually detect particles, a ”satisfactory” score is awarded to systems with the capability to individual detect particles with some limitations, and a ”bad” score is awarded to systems without the capability to individually detect particles.

004 - Cost

Cost of the detection system is graded based on a rough estimate of the equipment required. For systems costing below $100 a ”good” score is awarded, for system costing between $100 and $1000, a ”satisfactory” score is awarded, and any systems costing higher is awarded a ”bad” score.

005 - Construction

The ease of construction are evaluated to determine the feasibility of employing the setup with the readily available resources. As this criterion is not quantifiable, the scores are given qualitatively, based on the required amount of components and the required precision in setup.

6.4. Particle Measurement Techniques: Optical Methods

This section elaborates on the possible optical methods that may be employed to measure the size and/or the speed of the particles.

6.4.1. Particle Image Velocimetry

Particle Image Velocimetry (PIV) is an optical measurement technique used to displacement measurement of particles during two laser flashes (Harmand et al., 2013). The working principles as described by Zhang et al., 2018 are as follows. First, the fluid is seeded with tracer particles that match the fluid’s density and scatter light effectively. A laser sheet then illuminates a cross-section of the flow, making the particles visible. High-speed cameras capture two images of the illuminated particles at a controlled time interval. These images are divided into small interrogation windows, and the displacement of particle patterns between them is calculated using cross-correlation. Dividing the displacement by the time interval yields local velocity vectors, forming a complete velocity field. Finally, post-processing techniques are applied to reduce noise and enhance the accuracy of the data.

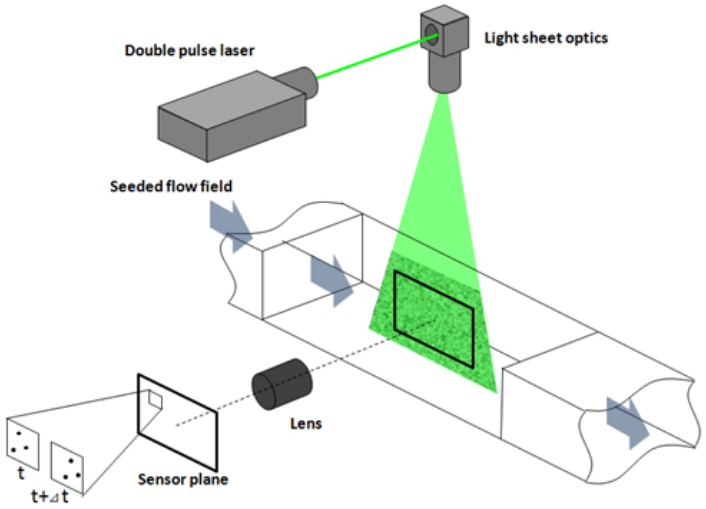

Figure 6.1: Diagram showing the working principles of PIV. Retrieved from Seika Digital Image Corporation, 2017.

The main advantages of PIV are that it is non-invasive and provides detailed, spatially resolved velocity fields. Moreover, it can measure 2D or 3D velocity fields depending on the setup (e.g., stereo-PIV for 3D measurements). Meanwhile, PIV is not capable of measuring the velocity of individual particles, unlike the particle tracking velocity method described in subsection 6.4.2. The cost of a PIV setup may be as low as $500, as highlighted by Acquah et al., 2024. In terms of construction of the PIV system, several components of the detection system must be sized to fit within the vacuum chamber. The camera and the illumination system must be placed within the limited space of the vacuum chamber. Moreover, several components of a PIV system require precision during setup to ensure accurate velocity measurements. A laser sheet to illuminate a 2D plane of the flow must be precisely aligned with the centerline of the vent. The camera must be mounted perpendicular to the laser sheet and the focused to the laser plane. Moreover, reflections shall be minimized. Since the vacuum chamber walls are of a metallic materials, the walls may need to be covered by a non-reflecting sheet. For these reasons, this detection system is graded as ”satisfactory” level for the 005 - Construction criterion.

6.4.2. Particle Tracking Velocimetry

Particle Tracking Velocimetry (PTV) is a flow measurement technique used to determine the velocity and trajectory of individual particles in a fluid (Dracos, 1996). It differs from Particle Image Velocimetry (PIV) by focusing on the motion of discrete particles rather than computing an averaged velocity field. The working principles are as follows. First, the fluid is seeded with tracer particles that are small, neutrally buoyant, and light-scattering to ensure they accurately follow the flow. The measurement region is then illuminated, typically using a laser sheet for 2D or volumetric lighting for 3D to make the particles visible. High-speed cameras capture successive images at precisely timed intervals, and multiple cameras may be used for 3D tracking. Image processing techniques detect individual particle positions with subpixel accuracy, and tracking algorithms link particles between frames to form trajectories. Particle velocities are calculated by dividing displacement by time, and post-processing is used to analyze trajectories, interpolate data, and extract detailed flow characteristics such as velocity gradients and vorticity.

Advantages of the PTV include the high accuracy to tracks individual particles, allowing precise velocity measurements, detailed flow information in which trajectories and interactions of discrete particles may be captured, and the applicability in complex flows. In terms of cost, a PTV system may cost as low as a few hundred dollars, according to Noto et al., 2023. The construction of a PTV system is similar to that of a PIV system.

6.4.3. Laser Doppler Velocimetry

Laser Doppler Velocimetry (LDV), also known as Laser Doppler Anemometry (LDA), is a non-intrusive optical measurement technique used to measure the velocity of a fluid or particles in a flow. It is based

on the Doppler effect, where the frequency of light scattered by moving particles changes relative to the velocity of the particles. LDV works by intersecting two coherent laser beams to create an interference fringe pattern in a small measurement volume. When tracer particles in the flow pass through this region, they scatter light with a frequency modulated by the Doppler effect. The scattered light is collected by a photodetector, which converts the signal into a frequency burst. This frequency is directly proportional to the velocity component of the particle along the beam intersection plane, allowing accurate determination of flow velocity without disturbing the fluid. The working principles of LDV is shown in Figure 6.2.

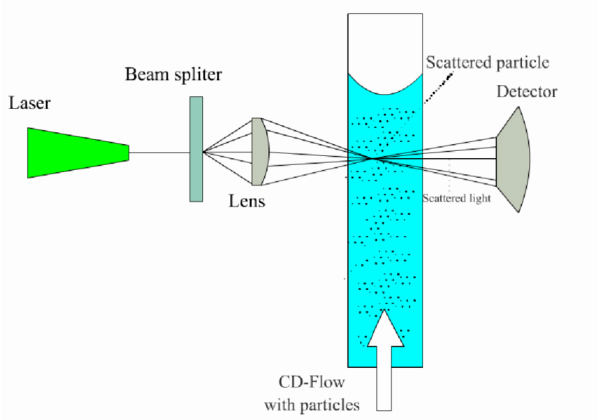

Figure 6.2: Diagram showing the working principles of LDV. Retrieved from Cito, 2010.

Instead of measuring the frequency shift directly, LDV often measures the interference pattern created by intersecting laser beams. This pattern forms regions of alternating high and low intensity, known as fringes. As particles pass through these fringes, they scatter light that fluctuates in intensity. The frequency of these fluctuations corresponds to the particle velocity.

The components of an LDV System include a laser source emitting coherent and monochromatic light, beam splitter to intersect light beams at a measurement volume and create a fringe pattern due to constructive and destructive interference, a photodetector collecting the scattered light and converting it into an electrical signal, and signal processing to analyze and determine the Doppler frequency shift.

Advantages of LDV are that it is non-intrusive, high in accuracy with high spatial and temporal resolution, directional sensitivity that can measure flow direction and reverse flows, and the capability of multi-dimensional measurements by using multiple laser pairs to measure velocity components in 2D or 3D. The limitations of LDV are that it requires seeding, in which particles must be introduced into the flow to scatter light effectively, the complex setup that involves optical alignment and calibration, the limited measurement volume, and cost compared to other velocimetry techniques.

6.4.4. Direct High-Speed Imaging

Direct imaging using high-speed cameras is a another method for optically measuring the velocity and, in some cases, the size of small solid particles in a flow. By capturing successive frames at high frame rates, this technique allows for accurate tracking of particle displacement over time, enabling velocity calculation. When paired with high-resolution imaging and proper calibration, particle size can also be estimated, particularly if the particles are spherical and well-focused. A typical setup includes a high-speed camera with a global shutter, and an illumination system. Image analysis software is then used to track particles frame by frame. While this approach is simpler and more flexible than laser-based systems like LDV or PTV, it does have limitations, such as difficulty tracking overlapping or out-of-focus particles, potential motion blur, and lack of depth information without stereo imaging. The detectability as well as distinguishing of individual particles may be limited by the size of the particles.

The cost of a high-speed camera starts at a price of a few hundred dollars, and increases in price for cameras of higher performance. An advantage of a direct high-speed imaging system is that the construction of the system does not require a precise illumination system.

6.5. Particle Measurement Techniques: Impulse-based Methods

6.5.1. Piezoelectric Sensor Detection

Impact-based detection principles measure the impulse of the incident particles. The particle's kinetic energy is related to its mass and velocity. Piezoelectric sensors convert applied mechanical stress into electric charge (Owojaiye and Sun, 2013). The signal amplitude, measured as voltage from the piezoelectric sensor is proportional to the impulse. With the piezoelectric sensor placed near the vent of the plume model, the mechanical force applied onto the sensor may be measured as voltage. The setup using a piezoelectric sensor consists of a sensor placed above the plume vent and an oscilloscope wired to the sensor to read output voltage signals. Because this detection principle measures impulse of the particles, the size of the particle may be determined only through using an estimate of particle velocity.

The capability of this detection system to distinguish individual particles depends on the sampling frequency of the oscilloscope. If multiple particles impact the sensor in short succession, the voltage signal may be overlapped, resulting in the derived particle size to be larger than the size of the individual particles. The low cost of a piezoelectric sensor (typically starting at $10), is an advantage of this detection method. Moreover, the construction of the system involve very few components; the sensor is to be wired to an oscilloscope for the output voltage to be read. Thus, this setup scores high on the cost and construction criteria.

6.5.2. Transient electricity detection method

Transient electricity detection employs a thin current-carrying film placed near the vent, at which an incident particle may cause several effects on the current. If a particle hits the film, this may cause a localized disturbance (e.g., resistance change, voltage spike), momentary heating, change in conductivity or impact ionization. The setup apparatus includes a current-carrying thin film (e.g. aluminum, indium tin oxide) and an oscilloscope (with GHz-level bandwidth). Similar to the piezoelectric sensing method, the voltage of the transient electricity may be measured to determine the impulse of the incident particle. A calibration is necessary to identify the size-signal relationship. This may be done using a nebulizer that spray particles of known size. The sensitivity of this technique is still unclear, and this remains as a disadvantage of this detection method.

Like the piezoelectric sensing method, this method is also of low cost. However, regarding the ease of construction of the system, the durability of the thin current-carrying film to repeated particle impacts and the vapor flow is questionable, making it possible that the thin film needs replacement after several uses.

6.5.3. Surface Acoustic Wave Sensing

An acoustics-based method using surface acoustic wave (SAW) sensor detect sound propagated as a result of the impact of the solid particles. As the particle impacts on the SAW path, a mechanical strain occurs as the site of impact. This generates a transient disturbance that propagates along the SAW path. The result is a brief disturbance peak. The amplitude of disturbance may be related to the mass and velocity of the impact, as it was shown in Equation 7.3.

One of the challenges in detecting surface acoustic wave is the noise in the surrounding environment. As the vacuum chamber evacuates air with the use of pumps throughout the experiment, this generates a fair amount of noise causing vibration at the detection surface that may drown out the signals attributed to solid particles. The cost of a SAW sensor has a wide range depending on its performance, with the lowest prices starting from $100. The setup of a SAW sensor in the plume model is similar to that of the piezoelectric sensor setup, with the SAW sensor being wired to an oscilloscope to read the voltage output from the sensor.

6.5.4. Conventional microphone

As another acoustics-based methods, conventional microphones are also considered. Conventional microphones such as dynamic microphones that function with a vibrating membrane may indeed capture traces of particles directly striking the membrane, causing vibrations. By analyzing the measured mechanical vibrations that the impact has caused, this may be linked to the kinetic energy of the particle that ultimately leads to determining the size or the speed of the particle. The working principle here

is, at the basic level, similar to that of piezoelectric impact detection. The difference lies in the way in which impact is measured: through a membrane/diaphragm system or a piezoelectric material. In fact, piezoelectric materials are used in contact microphones that are specialized to detect sound caused by direct mechanical contact. As conventional dynamic or condenser microphones use membrane or diaphragm designed to collect sound pressure waves, while it may be theoretically possible to detect small particles depending on its size and speed, it is less sensitive to mechanical impacts compared to piezoelectric sensors that are designed for this purpose. On the other hand, low-cost options are available with microphones, as the price varies greatly depending on the performance. The setup of the system is similar to that of a SAW sensor.

6.6. Comparison of detection methods

An overview of the main concepts are organized in the design option tree as shown in Figure 6.3.

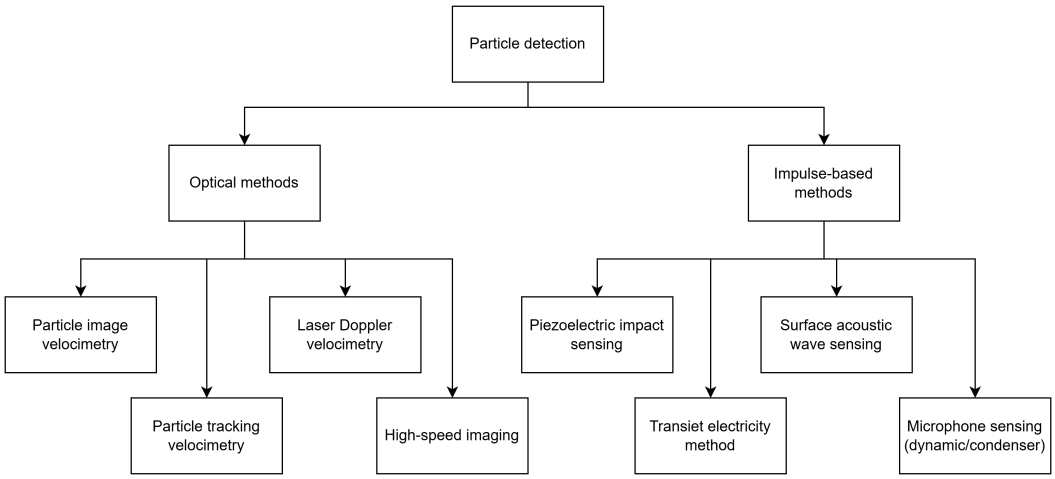

Figure 6.3: Design option tree showing possible particle detection methods.

A selection of detection method is made from the list of possible detection methods described earlier. A comparison is made between the options to tradeoff the relative advantages and disadvantages to determine the option with the best score. Table 6.3 show the scores given to each criterion. Final score of the trade off is shown in the right-hand most column, determined using the criteria weights defined in Table 6.2.

Table 6.3: Tradeoff scores for the final detection method selection.

Method	Size	Velocity	Individual detection	Cost	Ease of construction	Score
PIV	0	1	0	1	1	4
PTV	0	2	2	1	1	12
LDV	0	2	2	0	0	10
High-speed image	0	2	2	1	2	13
Piezoelectric	2	0	2	2	2	**16**
Transient electricity	2	0	2	2	1	15
SAW sensing	2	0	2	1	2	15

As a result of the tradeoff process, the piezoelectric detection method scored the highest among all considered detection methods. Transient electricity method and SAW sensing method score just below the piezoelectric sensing method, leaving the two as secondary options in case the first option is shown to be unfeasible.

7

Testing of Detection System

7.1. Detection System Setup

Piezoelectric sensors detect impact of solid particles by converting mechanical strain due to its strain into electrical charge that is detected as a voltage output. A piezoelectric sensor is positioned above the channel to detect solid particles exiting the vent. The piezoelectric sensor may be applied in several configurations. The simplest configuration would be to adhere the sensor onto a stiff support plate positioned above the vent to directly measure the impact of the sensor. An alternative configuration would be to employ the sensor as a cantilever beam, in which the sensor is clamped on one of its sides and the other end is used as the contact point for the ejected solid particles. For the case of this research, since the objective is to detect particles of very small size, the cantilever beam configuration is adopted as this configuration is relatively more sensitive compared to the direct impact configuration. A cantilever beam amplifies strain due to its lever arm geometry. Small forces applied at the tip cause larger bending moments at the fixed base, where the piezo sensor is typically placed. This results in greater local strain than a flat configuration, and hence a larger voltage output from the piezoelectric element. Figure 7.1 shows the sensor setup and the location and attachment of the piezoelectric sensor.

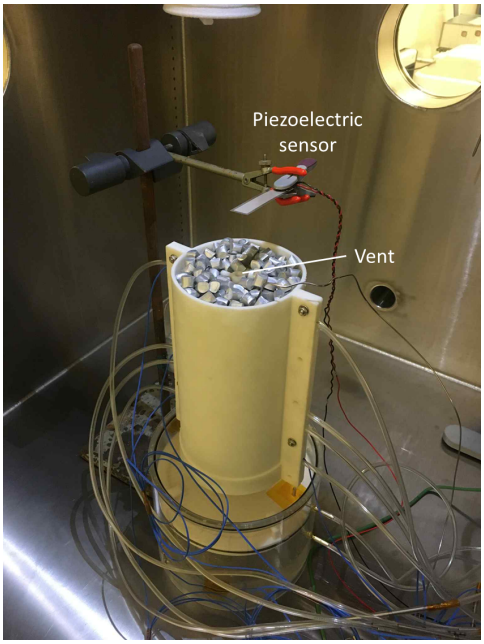

Figure 7.1: Cantilever beam configuration of the piezoelectric sensor placed above plume model vent.

For this research, the LDT-2-028K sensor from TE Connectivity is used. The sensor has a capacitance of 2.85 nF, a minimum impedance of 1 MΩ, and an output voltage of 10 mV to 100 V (Connectivity, 2017). The unclamped edge of the piezoelectric sensor is placed 5 cm above the vent. Piezoelectric sensor data are collected via the feedthrough wiring to an oscilloscope placed outside the vacuum chamber. For this research, the PicoScope 7 software is used to display and collect oscilloscope data on a computer.

7.2. Drop Test

The detection method is first tested using particles of known mass to investigate the response of the detection system. Grains of known mass are dropped onto the sensor impact surface. The voltage response of from the piezoelectric sensor is plotted against the estimated impulse of the impact. The correlation between impulse and voltage is used to extrapolate for size and velocity with the particle sizes found in the plumes. A linear relationship between the impulse of the grain and the voltage response is expected. This is because the strain of the sensor is dependent on the force that the grain exerts onto the sensor as it contacts the sensor tip. Equation 7.1 expresses the strain of a cantilever beam ϵ in terms of load F, beam length L, Young's modulus E, beam width b and beam height h_b.

$$\epsilon = \frac{6FL}{Ebh_b^2} \tag{7.1}$$

When the load is due to a particle impacting the beam, the load may be expressed as in Equation 7.2. Here, the load is expressed in terms of particle mass m, velocity V and contact time Δt.

$$F = \frac{mV}{\Delta t} \tag{7.2}$$

Assuming that the contact time for any small particle is constant, the strain caused by a small incident particle is linearly dependent on its impulse. Thus, the initial test campaign investigates the relationship between the measured voltage and the impulse of the incident grain particles. As voltage responses of the impact, maximum voltage and peak-to-peak amplitude are acquired to determine the response with a closer fit to the particle impulse. Impulse of the grain may be estimated using Equation 7.3.

$$J = mv \tag{7.3}$$

The speed of the grain v is determined using Equation 7.4.

$$v^2 = u^2 + 2as \tag{7.4}$$

Here, v is the final velocity of the grain, u is the initial velocity of the grain (assumed to be 0), a is the acceleration on the grain (assumed to be gravitational acceleration g = 9.81), and s is the drop height of the grain. For this drop test, drop height and grain mass were varied.

7.2.1. Initial Test: Large Grains

In the initial tests, beads grains are dropped from varying heights. Moreover, two different bead masses are also tested: 17 mg and 14 mg. Two variants of response are acquired from the test: maximum voltage and peak-to-peak voltage. 10 trials are conducted for each test case. Figure 7.2 and Figure 7.3 show the correlation between particle impulse and measured voltage. Figure 7.2 plots the maximum voltage measured from the impact, while Figure 7.3 plots the peak-to-peak voltage. Each data point shows the average result for the test case. The test case is labelled on each data point, showing the mass of the grain and the drop height.

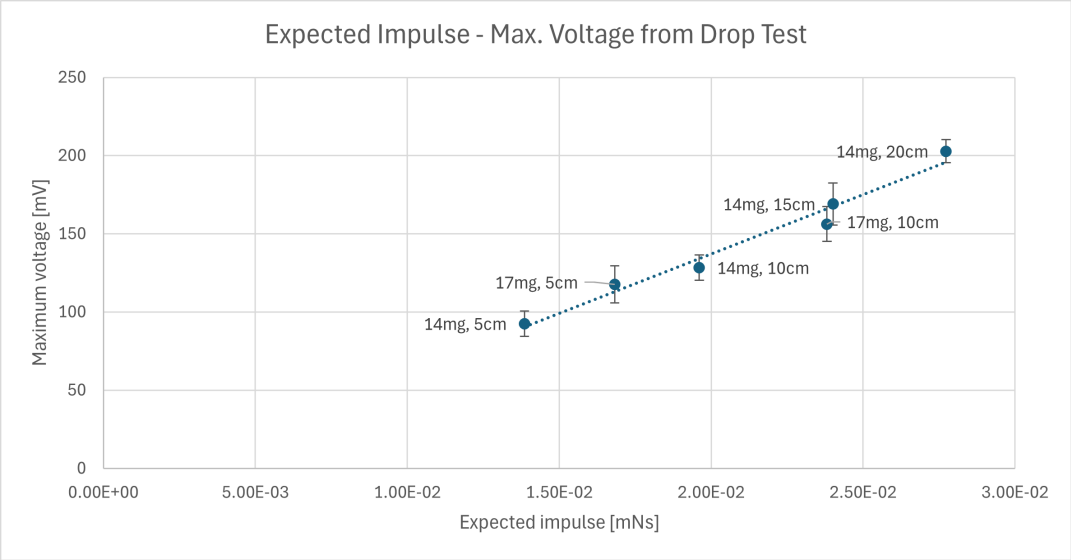

Figure 7.2: Plot showing measured maximum voltage and estimated impulse of impact particle from large grain tests. Mass and drop height for each test case are labeled on each average measurement point.

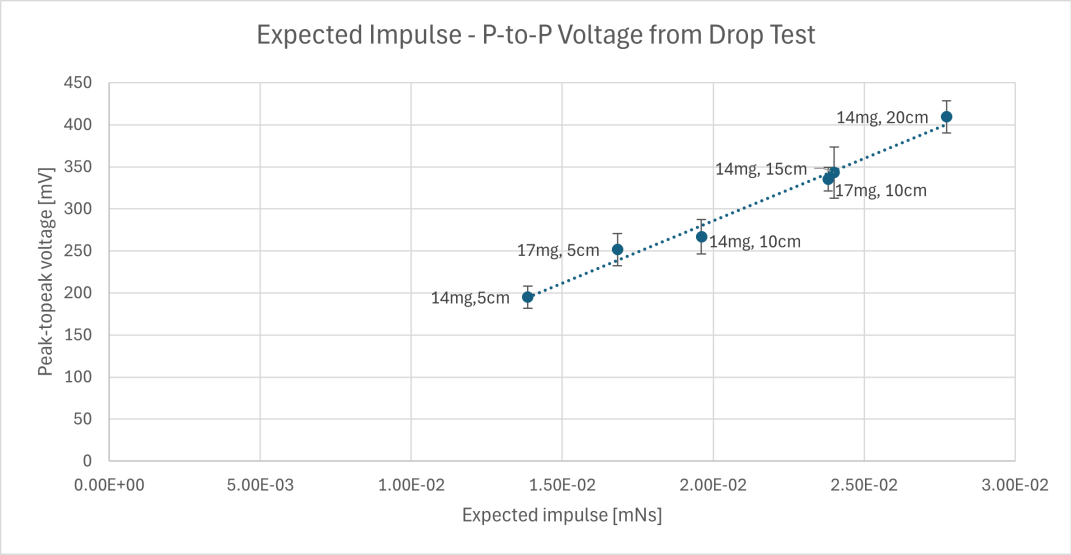

Figure 7.3: Plot showing measured peak-to-peak voltage and estimated impulse of impact particle from large grain tests. Mass and drop height for each test case are labeled on each average measurement point.

A linear relationship between impulse and voltage may be observed with the maximum voltage - impulse relationship having an R^2 number of 0.993, and the peak-to-peak voltage - impulse relationship having and R^2 number of 0.995. The linear best fit line is as shown in Equation 7.5 and Equation 7.6. The R^2 values here show a slightly stronger correlation for the peak-to-peak voltage than the maximum voltage. The best fit line may be used to extrapolate the voltage signal for a given impulse. Here, J is impulse, V_{max} is maximum voltage and V_{peaks} is peak-to-peak voltage.

$$V_{max} = 6920.13J \tag{7.5}$$

$$V_{peaks} = 14336.55J \tag{7.6}$$

Since the grains tested here are well within the detectable range, smaller grains are tested for the secondary tests elaborated in subsection 7.2.2.

7.2.2. Secondary Test: Small Grains

Secondary tests were conducted to test the detection system with smaller masses and lower drop heights. The objective here is to determine the lowest impact that the detection system can register. Here, grain masses of 3 mg and 1 mg are used. Again, a linear relationship between the impulse of the grain and the voltage response is expected. However, if the voltage response is smaller than the signal noise, a lower limit on the detectable impulse is reached.

?? shows the expected impact speed and impulse for each tested mass and height case, combined with the measurement results of maximum voltage and peak-to-peak voltage. Like the initial test, 10 trials are conducted for each test case, and **??** shows the average measured voltage for each test case. For the test case with mass 1 mg and drop height 0.1 cm, no response signals were detected. Figure 7.4 and Figure 7.5 show the correlation between particle impulse and measured voltage. Figure 7.4 plots the maximum voltage measured from the impact, while Figure 7.5 plots the peak-to-peak voltage.

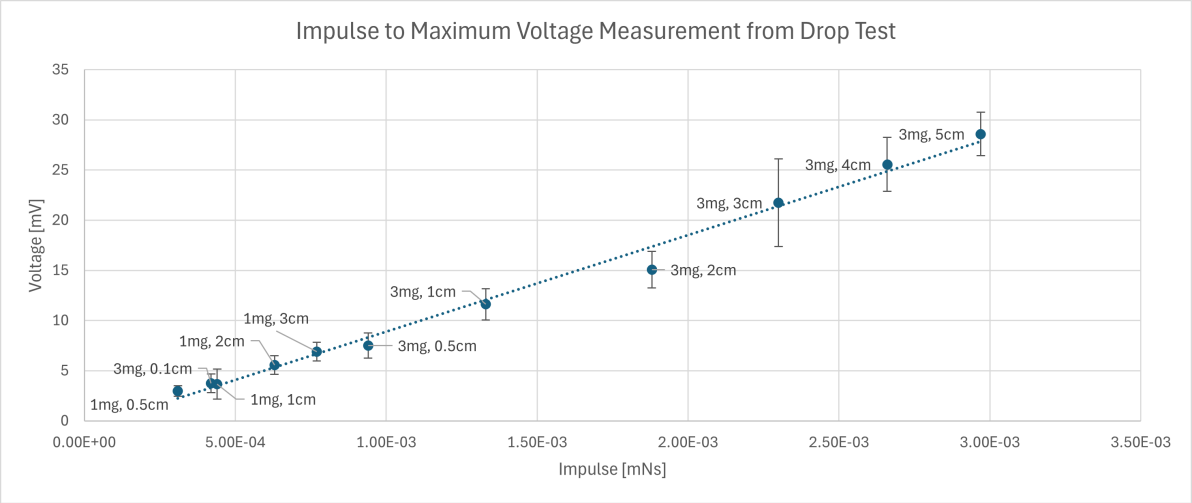

Figure 7.4: Plot showing measured maximum voltage and estimated impulse of impact particle from small grain tests. Mass and drop height for each test case are labeled on each average measurement point.

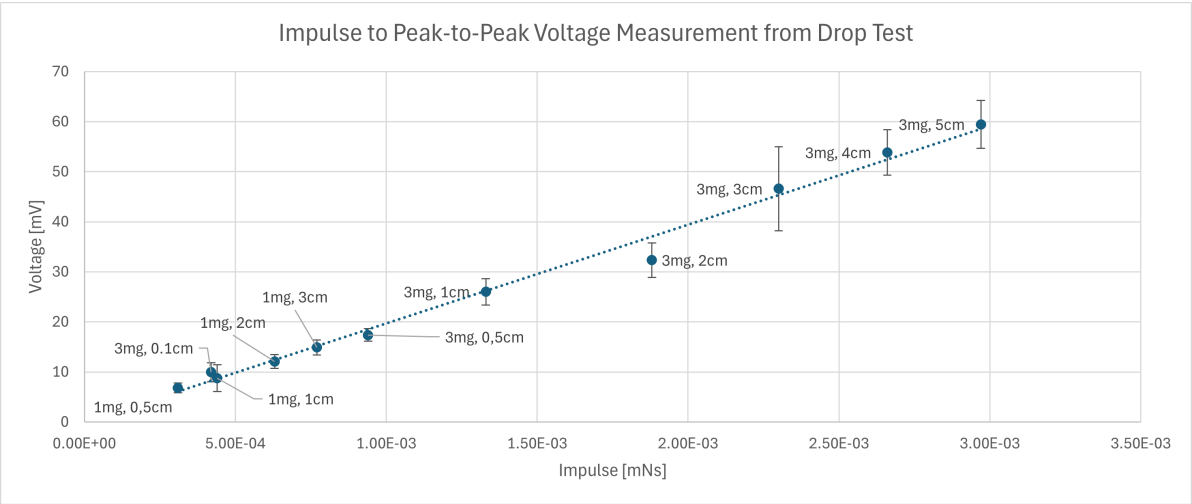

Figure 7.5: Plot showing measured peak-to-peak voltage and estimated impulse of impact particle from small grain tests. Mass and drop height for each test case are labeled on each average measurement point.

A linear relationship between impulse and voltage is again observed with the maximum voltage - impulse relationship having an R^2 number of 0.979, and the peak-to-peak voltage - impulse relationship having and R^2 number of 0.984. Again, the R^2 values here show a stronger correlation for the peak-to-peak values. The linear best fit line slopes (assuming y-intercepts of 0) according to maximum voltage and peak-to-peak voltage are 9249.85 V/Ns and 19705.75 V/Ns, respectively. The slope values may be used to extrapolate for the voltage signal for a given impulse. This is shown in Equation 7.7 and Equation 7.8. Here, J is impulse, V_{max} is maximum voltage and V_{peaks} is peak-to-peak voltage.

$$V_{max} = 9249.85J \tag{7.7}$$

$$V_{peaks} = 19705.75J \tag{7.8}$$

7.2.3. Comparison of Large Grain and Small Grain Tests

The results from the small grains may be combined with the data from the previous investigations using large grains, presented in subsection 7.2.1. The full overlay plots for maximum voltage and peak-to-peak voltage are as in Figure 7.6 and Figure 7.7 respectively.

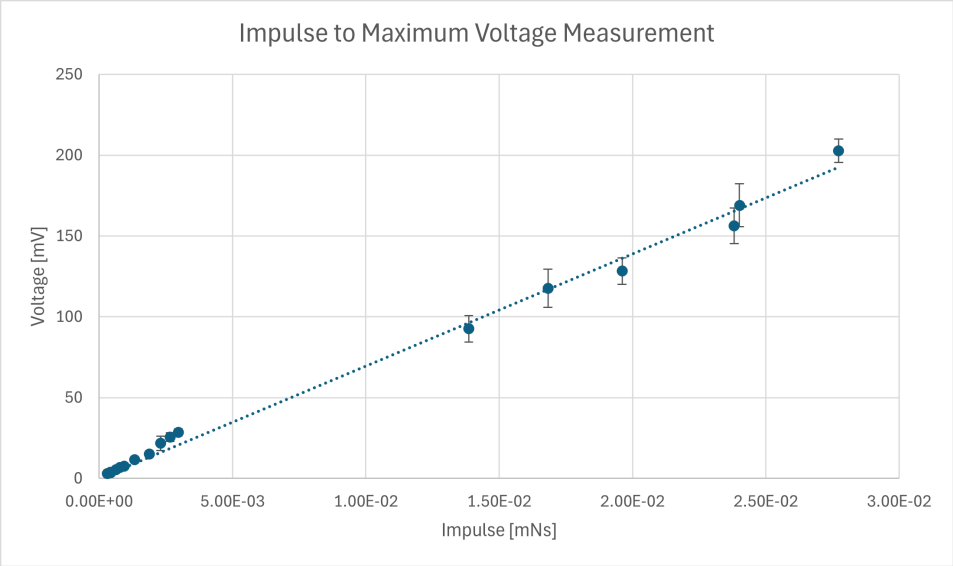

Figure 7.6: Plot showing measured maximum voltage and estimated impulse of impact particle from small and large grain tests. Mass and drop height for each test case are labeled on each average measurement point.

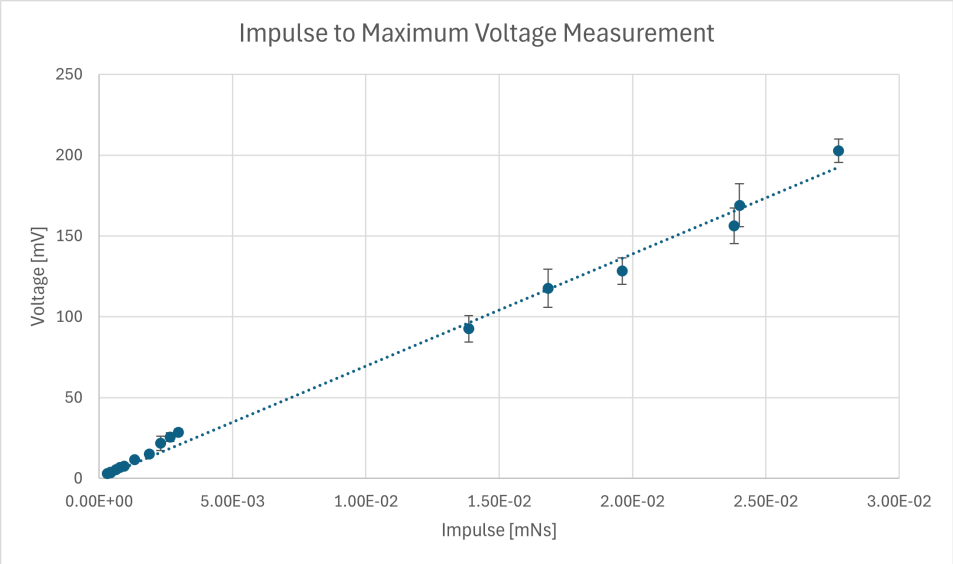

Figure 7.7: Plot showing measured peak-to-peak voltage and estimated impulse of impact particle from small and large grain tests. Mass and drop height for each test case are labeled on each average measurement point.

A linear relationship between impulse and voltage is again observed with the maximum voltage - impulse relationship having an R^2 number of 0.993, and the peak-to-peak voltage - impulse relationship having and R^2 number of 0.991. Again, the R^2 values here show a stronger correlation for the peak-to-peak values. The linear best fit lines are shown in Equation 7.9 and Equation 7.10. Here, J is impulse, V_{max} is maximum voltage and V_{peaks} is peak-to-peak voltage.

$$V_{max} = 6899.016J \tag{7.9}$$

$$V_{peaks} = 14329.95J \tag{7.10}$$

The small grain tests showed a larger slope compared to the large grain tests. This suggests that the small grain tests have picked up higher voltages than it would have given the results of the large grain tests. The difference may be attributed to the precision of the grain's impact point on the sensor. The large grain tests involved dropping the grains from a higher point than the small grain tests. With the grains dropped from a higher point, the grains have a higher chance of deviating from the intended aiming point on the sensor, which is the tip of the unclamped edge. The standard deviation values for test 1 is 19.3 mV on average, whereas the standard deviation values for test 2 is 3.0 on average. For a more precise measurement of the drop test with the purpose of establishing an empirical relationship between the impulse and the voltage, it is recommended to employ a more precise method to conduct the drop test.

The derived slopes are used in the following subsection 7.2.4 to determine the minimum detectable particle size.

7.2.4. Noise Analysis

The noise detected during the drop tests shows an indication of the minimum detectable voltage and therefore particle size and/or speed. The signal noise in terms of maximum voltage is measured to be 1.866 mV, and 4.011 mV in terms of peak-to-peak signal. Using the slope values derived in subsection 7.2.2, the minimum detectable impulse according to maximum voltage and peak-to-peak voltage are 0.000202 mNs and 0.000204 mNs, respectively. Given an assumed particle velocity, Equation 7.3 can be used to determine particle mass, and Equation 7.11 can be used to determine particle size assuming a particle density ρ. For this investigation, a particle density for ice (918 kg/m^3) is used.

$$m = \frac{4}{3}\rho\pi r^3 \tag{7.11}$$

Figure 7.8 plots the minimum detectable particle size as a function of particle velocity. This plot uses Figure 7.5 to determine the minimum impulse, as peak-to-peak voltage tends to have a stronger correlation than the maximum voltage, and test 2 drop test has a lower standard deviation value than test 1.

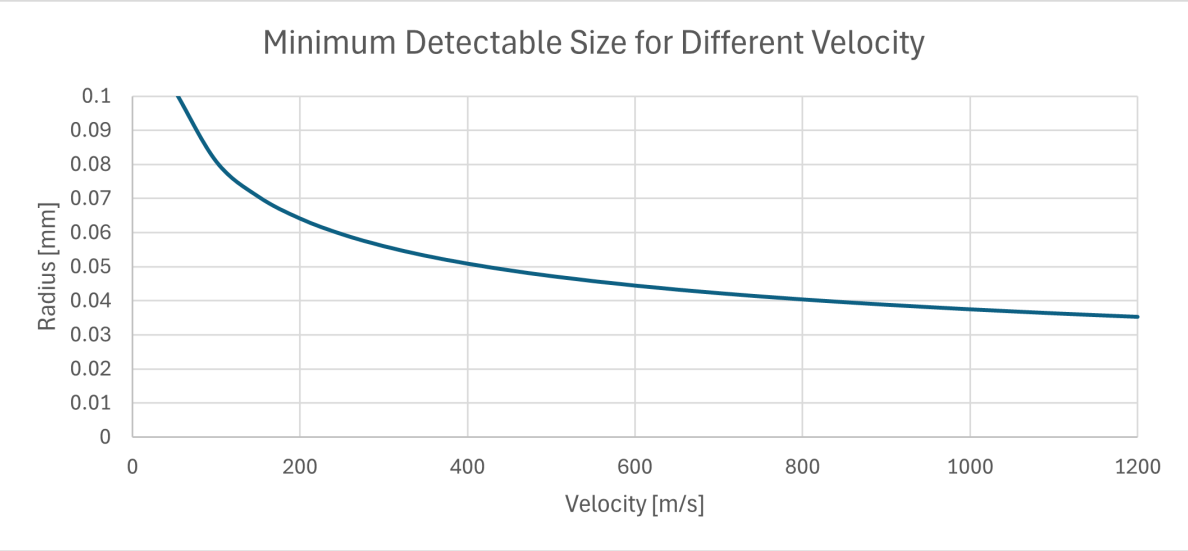

Figure 7.8: Plot showing measured peak-to-peak voltage and estimated impulse of impact particle from small and large grain tests. Mass and drop height for each test case are labeled on each average measurement point.

When particle speed is assumed to be 800 m/s (as was the maximum velocity for the baseline experiment), the minimum detectable particle diameter is 0.081 mm.

7.3. Detection of Plume Particles

The piezoelectric system setup is tested in the vacuum chamber to investigate solid particle detection in the plume model. The setup in the chamber is as described in section 7.1.

Data from the piezoelectric sensor is collected through the PicoScope 7 software, working as a separate data acquisition system from the temperature and pressure measurements. Thus, it is essential to apply a method in which the time frame of the two data may be coupled. For this research, a stopwatch is started at the beginning of data acquisition for temperature and pressure sensors. The sensor-oscilloscope starts acquisition of data as boiling starts in the reservoir. The stopwatch time at which this is started is kept in a record. Video footage were also taken during the experiment for visual aid of the sensor status.

7.3.1. Test Result Overview

The temperature and differential pressure profile of the test are as shown in Figure 7.9. These plots are used to analyze the status of the plume model during the detection of particles with the piezoelectric sensors. For a more detailed analysis into the temperature and differential pressure at each event location, a zoomed view of the plots are provided in each respective section. It shall be noted that some sections of the readings for differential pressure measurements Figure 7.9b exceeded the measurement limit, and this is also shown in the figure as a dotted line labeled as ”Pressure measurement limit”. The time frame of the experiment is based on t_0, defined as the start of temperature and pressure data acquisition (i.e. consistent with the horizontal axis of Figure 7.9a and Figure 7.9b).

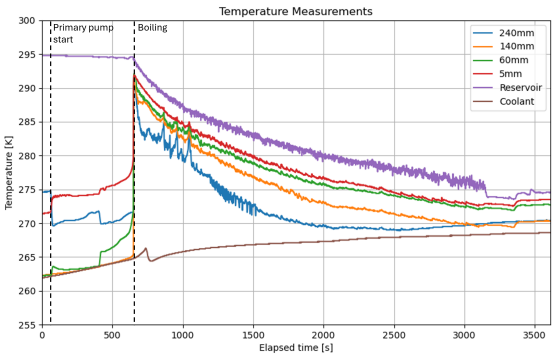

(a) Temperature measurements of a test with piezoelectric impact sensors. Temperatures are measured at several locations along the channel, with the height from the channel inlet indicated in the plot legend.

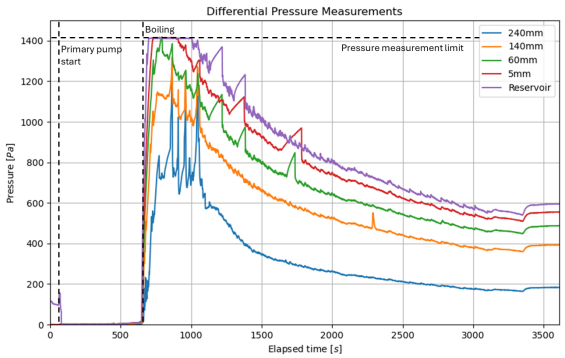

(b) Differential pressure measurements of a test with piezoelectric impact sensors. Pressures are measured at several locations along the channel, with the height from the channel inlet indicated in the plot legend.

Figure 7.9: Overview of temperature and differential pressure profiles for the piezoelectric sensor test.

Like the baseline experiment, as the boiling of the reservoir begins, temperature values along the channel temporarily converge towards a value between 285 K and 290 K. The temperatures then slowly decrease throughout the experiment. Small fluctuations of temperature may be seen throughout the experiment, and these are due to bubble bursts in the reservoir. Moreover, a buildup of ice occurs along the walls of the channel, and when these build up of ice comes directly in contact with the thermocouples, it will also interfere with the temperature measurement.

As air is evacuated from the chamber and boiling starts, the flow of water vapor is seen to begin as differential pressure shows a steep increase. Boiling is observed to be the most intense in the first few minutes after it has started, and during this phase, the differential pressure measurements near the reservoir shows a high value, while those for locations higher up in the channel indicate lower values. It is worth noting that condensation along the walls of the channel occasionally cause disturbances in the measurement of pressures due to entrapment of water droplets in the sensor holes. After the initial boiling, differential pressures uniformly decrease.

Figure 7.10 shows the velocity of the flow at measurement locations along the channel, based on the differential pressure measurements. The velocity plots are used in subsection 7.3.3 and subsection 7.3.5 to determine the size of the detected particles.

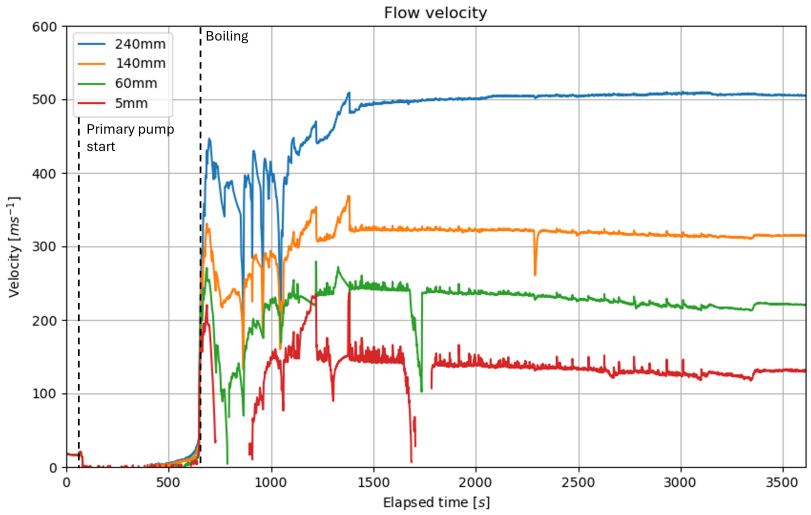

Figure 7.10: Velocity measurements of a test with piezoelectric impact sensors. Velocities are determined based on pressure measurements at several locations along the channel, with the height from the channel inlet indicated in the plot legend.

It should be noted here that the velocities plotted here may have some offset from the real flow speed. This was seen in the baseline experiments in which Pitot probes were used to measure the speed of the flow at the vent, as shown in Figure 5.11. In this figure, a comparison is made between the flow speed determined using the 240 mm differential pressure measurements and the two flow speeds based on Pitot probe measurements through different analyses methods. It was observed here that the velocities based on the Pitot tube were higher than the velocities based on differential pressure measurements for most of the experiment duration, as the maximum Mach number based on the Pitot probe is 2.00, while the Mach number based on differential pressure is 1.58. With the current piezoelectric sensor setup, the Pitot probe cannot be placed over the vent of the channel. Thus, the minimum detectable particle size may be of lower size than the size determined here. It is a future recommendation for an Empirical relation to be derived between the Pitot probe speed and the differential pressure speed.

7.3.2. Overview of Piezoelectric Sensor Readings

The full data of the piezoelectric sensor readings are presented here. Several types of wave are detected in the sensor readings, and these different types are annotated in the overview. Each wave type are elaborated in their respective sections. The list of all types of waves and its annotation color are as follows.

- Type I (red): damped wave
- Type II (yellow): turbulent wave
- Type III (green): low-amplitude periodic wave

Figure 7.11 and Figure 7.12 shows the readings from the piezoelectric sensor, measured between 0 seconds and 780 seconds, and 780 seconds and 1560 seconds since t_0, respectively. The full data is available in Appendix A.

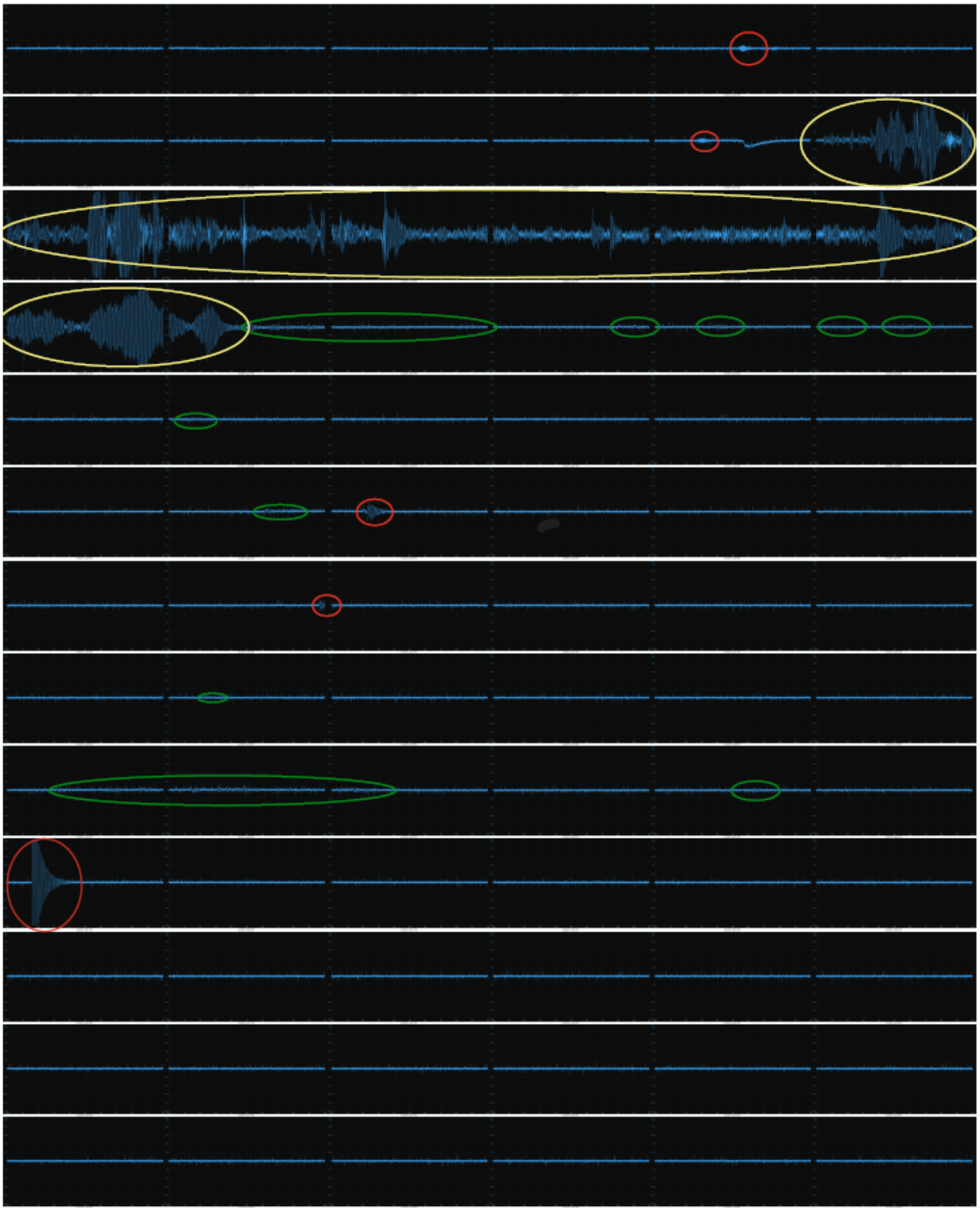

Figure 7.11: Waveform generated from piezoelectric sensor reading, measured between 0 seconds and 780 seconds since t_0.

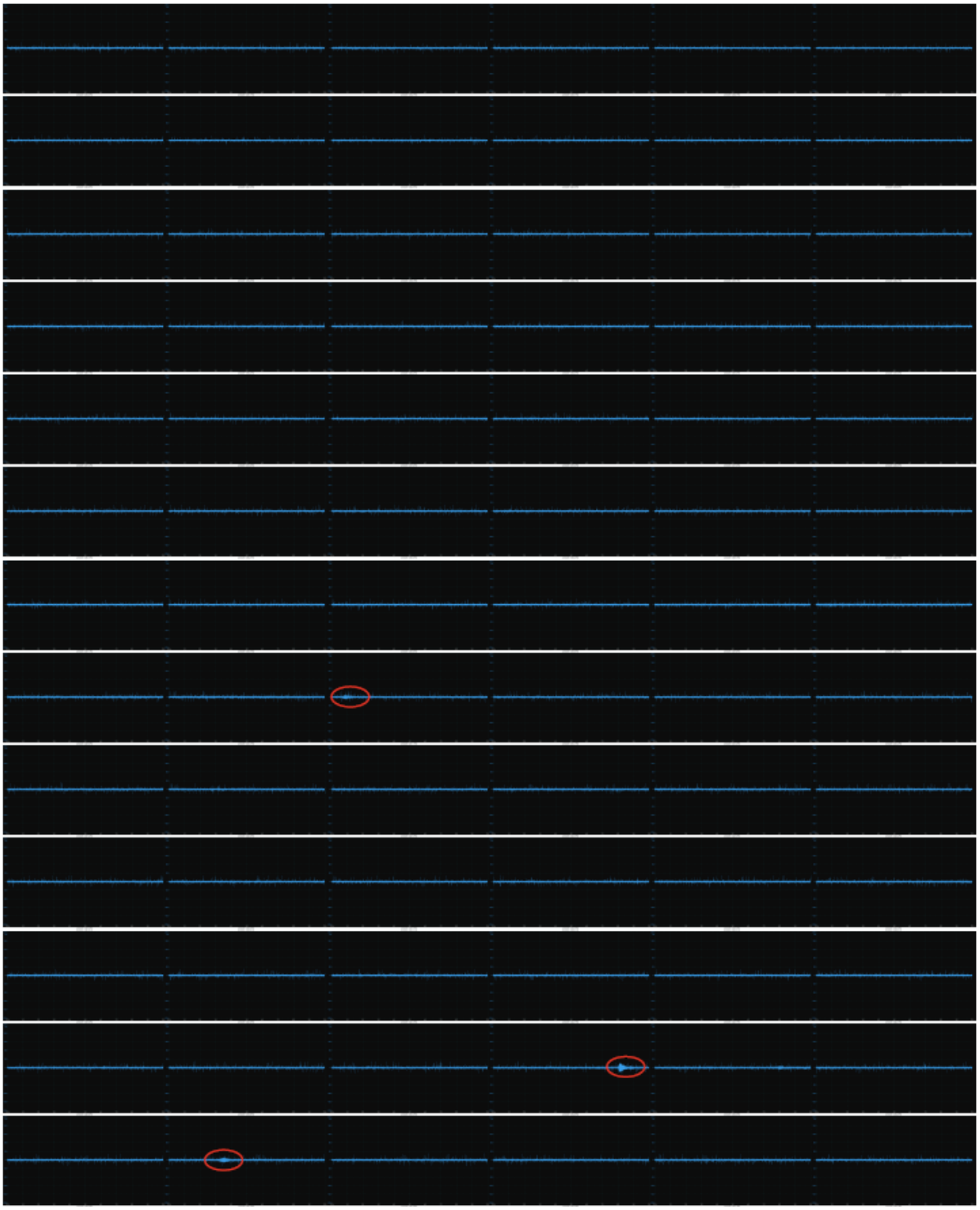

Figure 7.12: Waveform generated from piezoelectric sensor reading, measured between 780 seconds and 1560 seconds since t_0.

The readings from the piezoelectric sensor showed a flat waveform for most of the experiment. An example of this flat wave is shown in Figure 7.13. This flat wave is observed between 794 seconds and 804 seconds since t_0. As it can be seen in the differential pressure plots in Figure 7.9b, there is a flow of water vapor when this measurement was taken. This shows that a constant flow of gas incident onto the sensor is not registered in the piezoelectric sensor. This is because the piezoelectric sensor detects changes in strain of itself. With a constant flow of vapor flow, the sensor is strained to some

extent, but more importantly there is not change in the strain. Thus, it can be said that the force due to the flow of vapor does not significantly disturb the detection of solid particles as long as the flow is constant. An analysis of the wave noise is performed in subsection 7.3.6 to determine the minimum detectable particle size with the test setup employed in the vacuum chamber. The full voltage plot is not shown due to the length of the full data. Instead, the notable waveforms are picked up and presented in this section.

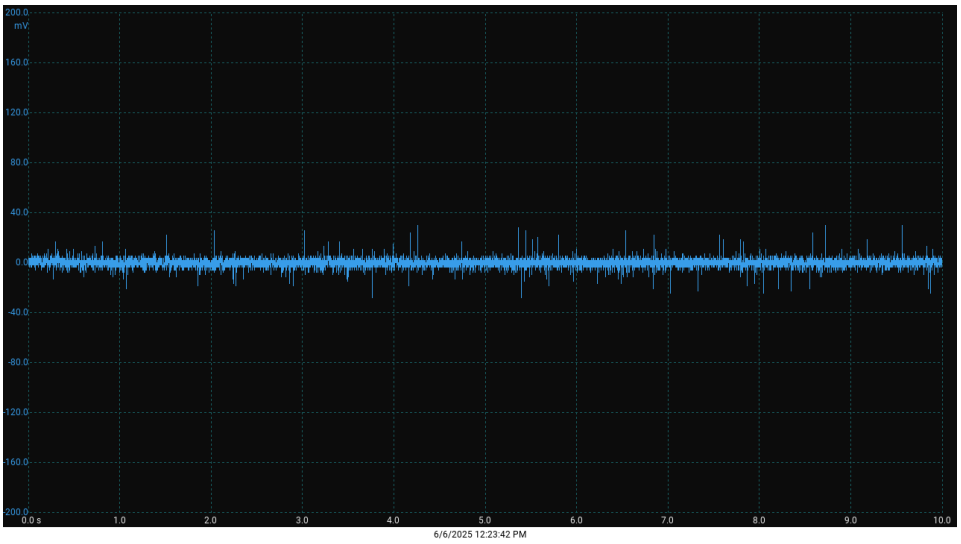

Figure 7.13: Flat waveform generated from piezoelectric sensor reading, measured between 794 seconds and 804 seconds since t_0.

On the other hand, notable waveforms were observed at several points in the experiment. These waveforms may be categorized by its shape: damped wave, turbulent wave, and low-amplitude periodic wave. The following sections review the observed notable waveforms by its shape.

7.3.3. Damped Wave

A damped wave in this particular setup with a piezoelectric sensor configured as a cantilever beam, typically suggests that the system has undergone a sudden mechanical excitation, and then gradually returned to rest due to energy dissipation (such as friction, air resistance, internal damping). Several of these damped waveforms were observed during the experiment. Figure 7.14 is the waveform observed between 874 seconds and 884 seconds since t_0, and it shows an example of a damped wave. Figure 7.15 shows the corresponding temperature and differential pressure readings between 874 seconds and 884 seconds.

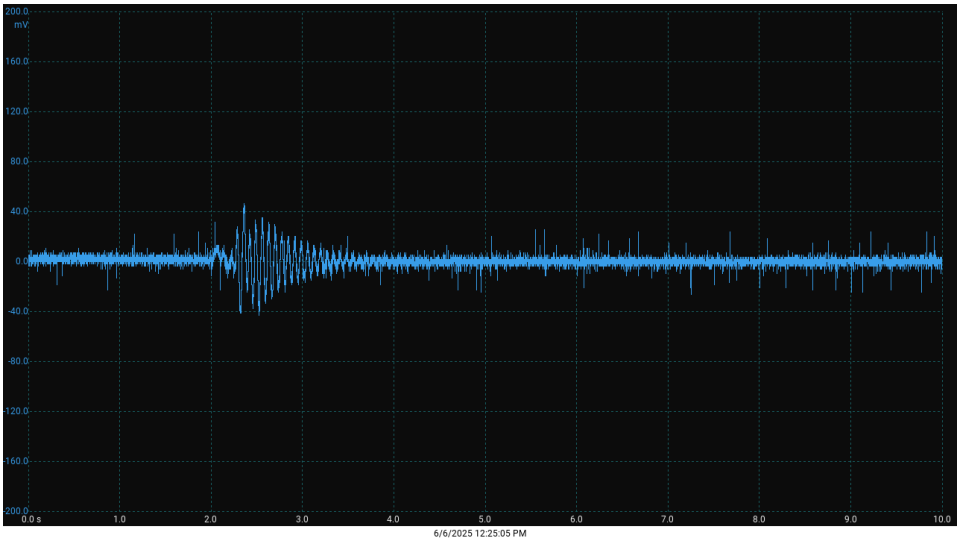

Figure 7.14: Damped waveform generated from piezoelectric sensor reading, measured between 874 seconds and 884 seconds since t_0.

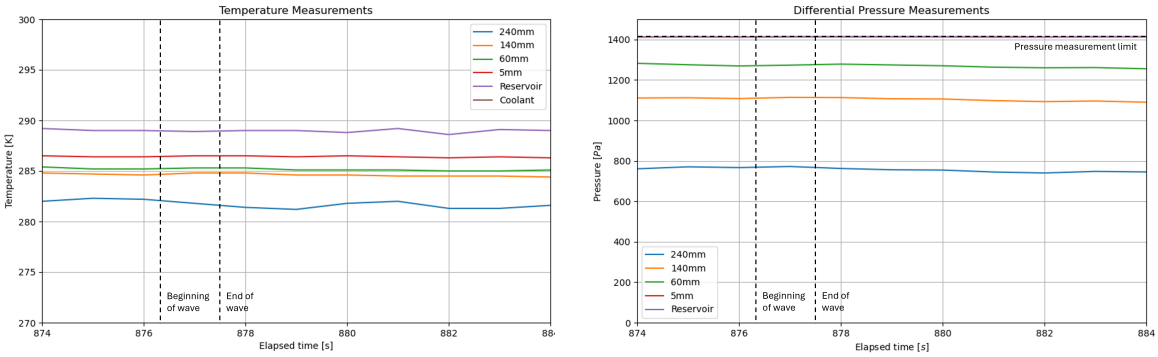

(a) Temperature measurements between 874 seconds and 884 seconds. Measurement locations are indicated in the legend.

(b) Differential pressure measurements between 874 seconds and 884 seconds. Measurement locations are indicated in the legend.

Figure 7.15: Temperature and pressure measurements between 874 seconds and 884 seconds since t_0.

Here, a maximum voltage of 46.57 mV and a peak-to-peak voltage of 89.41 mV is detected.

Solid particle as Origins

Solid particle or liquid droplets rising up from the reservoir and striking the sensor are the most likely candidate for the source of this sudden mechanical excitation. As the particle strikes the sensor, the sensor is mechanically strained momentarily, and as the particle is deflected away, the sensor damps down back to its original state. While a direct imaging of the particle using the video footage was not achieved, a slight vibration of the sensor was imaged in the video footage.

The flow speed at this time is 380 m/s, and if it is assumed that the particle speed is coupled to this speed, the particle size estimated using the drop test results is 0.292 mm in diameter.

Consideration of Other Possible Origins

Another possible source of a damped waveform may be an increase in the speed of the vapor flow, such as due to an unclogging of the channel. It has been observed in the experiments that ice accumulates along the channel walls. This occasionally causes the channel to be clogged. When this clogging is resolved, a sudden increase in the channel flow can occur, causing a sudden mechanical strain on the sensor.

However, it may also be said that an increase in the channel flow would not cause a periodic motion of the sensor after the initial mechanical excitation. This is because after the sensor is strained from the new flow, the sensor remains in the lifted position as the new flow continuously applies an upward force onto the sensor. As the piezoelectric sensor detects changes to the strain, the wave would gradually flatten without a periodic wave due to the flapping of the sensor after the initial impact. Figure 7.16 shows an example of such occurrence. This dip-shaped wave was recorded at the start of boiling between 654 seconds and 664 seconds since t_0. Moreover, Figure 7.17 shows a comparison of the piezoelectric sensor bending state at 654 seconds (before the dip wave) and at 664 seconds (after the dip wave). Here, it can be seen that the sensor changed its position due to the rush of vapor flow. As boiling start, the first wave of vapor flow travels up the channel, ultimately reaching the sensor. In Figure 7.16, it can be seen that a dip without a sinusoidal signal can be spotted, as this first wave of flow lifts the position of the sensor up and applying a constant strain on the sensor. Because the only change to strain on the sensor occurs when the sensor is lifted up, no sinusoidal waves due to some sudden mechanical impact is observed.

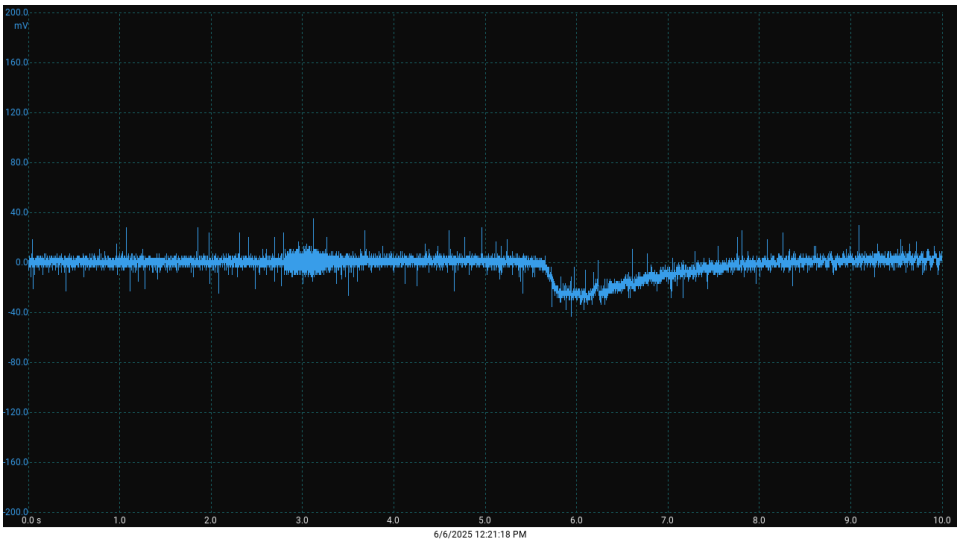

Figure 7.16: Dip waveform generated from piezoelectric sensor reading, measured between 654 seconds and 664 seconds since t_0.

In Figure 7.15b, while there are observations of slight fluctuations in the differential pressure, no significant change in differential pressure is observed. Consequently, it is likely that an unclogging of the channel is the cause of this particular damped wave.

Another source that this waveform may be attributed to is a burst of bubble in the reservoir. A pressure wave of a bubble burst may momentarily cause the sensor to strain before returning to its original position. However, bursting of bubbles was observed throughout the initial phase of the plume, while the sensor data for the most part showed flat wave as seen in Figure 7.13. Since the reservoir pressure measurements is at its upper limit during this time, it is not possible to verify this possibility through an analysis of the differential pressure data. Other possible sources include accidental mechanical shock to the system. Nevertheless, solid particles or liquid droplets striking the sensor impact point remains the most likely source of this damped waveform. For this observed waveform, an estimate of the particle size may be derived assuming a given particle speed.

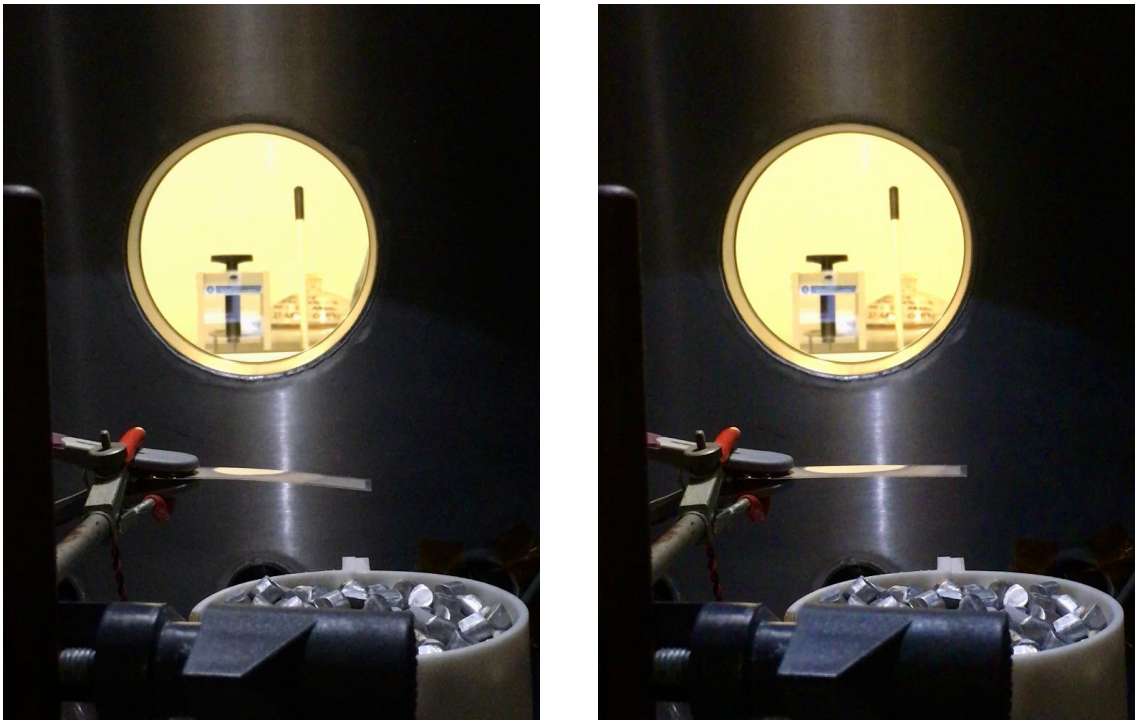

(a) Piezoelectric sensor orientation at 654 seconds since t_0.

(b) Piezoelectric sensor orientation at 664 seconds since t_0.

Figure 7.17: Comparison of piezoelectric sensor orientation between 654 and 664 seconds since t_0.

7.3.4. Turbulent wave

A turbulent wave with varying amplitude in this experimental setup suggests an unsteady interaction between the sensor and the fluid dynamics of the airflow. Turbulent waves were observed during the initial boiling of the reservoir. The turbulent waves show no clear sinusoidal or impulsive shape, with the amplitude fluctuating irregularly over time. Figure 7.18 shows the sensor measurement between 684 seconds and 694 seconds since t_0. The corresponding differential pressure measurements between 680 seconds and 800 seconds is shown in Figure 7.19b. Moreover, Figure 7.18 shows a comparison of the piezoelectric sensor bending state at 684 seconds and 694 seconds since t_0.

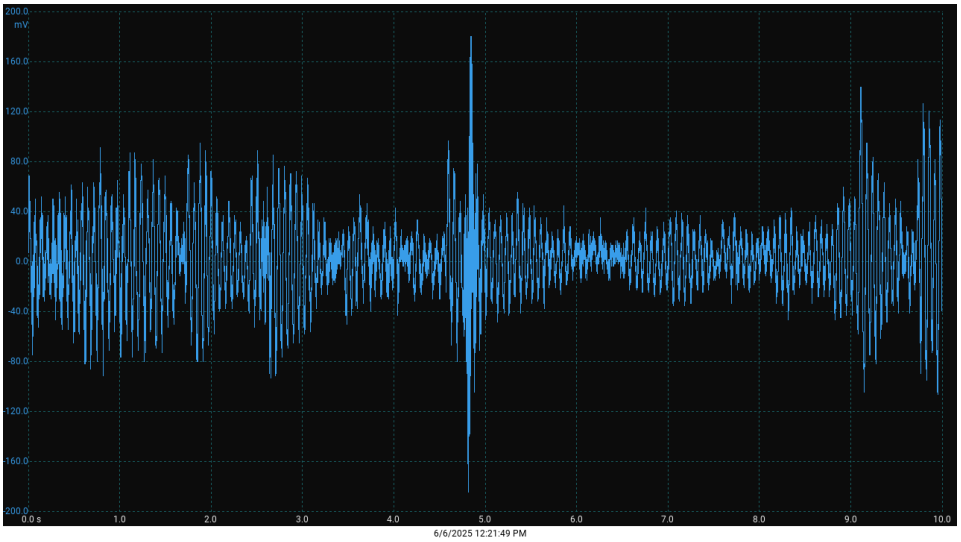

Figure 7.18: Turbulent waveform generated from piezoelectric sensor reading, measured at 684 seconds since t_0.

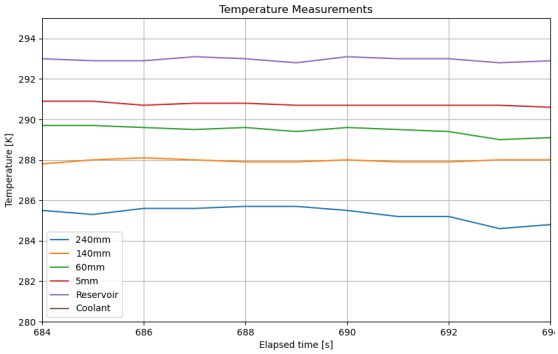

(a) Temperature measurements between 684 seconds and 694 seconds since t_0. Temperatures are measured at several locations along the channel, with the height from the channel inlet indicated in the plot legend.

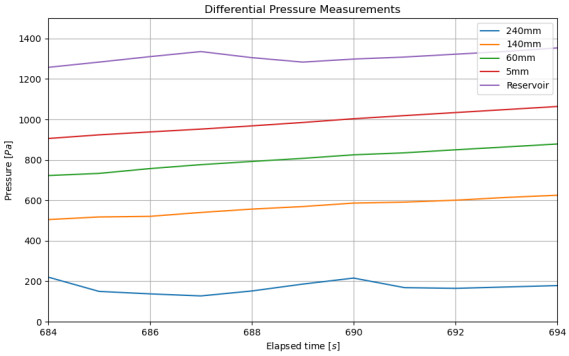

(b) Differential pressure measurements between 684 seconds and 694 seconds since t_0. Pressures are measured at several locations along the channel, with the height from the channel inlet indicated in the legend.

Figure 7.19: Overview of temperature and differential pressure profiles for the piezoelectric sensor test.

(a) Piezoelectric sensor orientation at 684 seconds since t_0.

(b) Piezoelectric sensor orientation at 694 seconds since t_0.

Figure 7.20: Comparison of piezoelectric sensor orientation between 684 and 694 seconds since t_0.

Source of Turbulent Waves

The turbulent waves here may be directly attributed to the intense initial bubbling in the reservoir. It was observed during this phase that the sensor had a repeated flapping movement, causing a series of sensor strain, and thus this unsteady flow of vapor is most likely what was causing the turbulent readings in the measurement. The flapping of the sensor is shown in Figure 7.20. The turbulent wave is not observed in other phases of the experiment.

Figure 7.19b shows a constant increase in the 5 mm, 60 mm and 140 mm differential pressures. Meanwhile, the reservoir pressure and the 240 mm pressure show some fluctuations. This pressure profile suggests that the speed of the flow and the mass flow rate within the channel are constantly changing, and as a result, causes a vigorous movement of the piezoelectric sensor. It is also possible that parti-

cles are ejected during this phase, with the turbulent flow making the detection difficult. Figure 7.19a shows some fluctuation of temperature at all measurement locations. In the case that particle formation is occurring, an increase in temperature may be expected due to the exothermic nature of the process. Here, an increase in temperature is not registered, and thus the temperature data here does not suggest the generation of particles. A further analysis of the sensor response may allow for the particles to be differentiated from the flow wave, but it should also be noted that the impacts may also be due to liquid droplets, as Figure 7.9a shows that the temperature in the channel is still above freezing point at this phase of the experiment.

7.3.5. Low-amplitude periodic wave

This wave shape shows a low amplitude at all points along the wave (peak-to-peak amplitude of 60 mV), and shows a somewhat sinusoidal shape. An example of this low-amplitude periodic wave is shown in Figure 7.21, measured between 1044 and 1054 seconds since t_0.

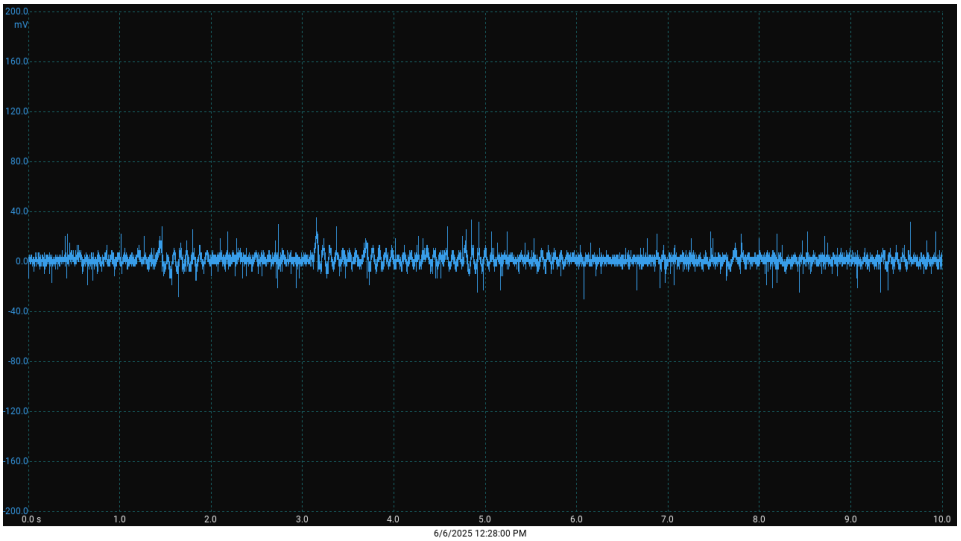

Figure 7.21: Periodic waveform generated from piezoelectric sensor reading, measured between 1034 seconds and 1044 seconds since t_0.

While the waveforms do not stand out from the regular noise, sinusoidal shapes may be observed at several locations. Similar to Figure 7.14, waves with an initial impact followed by a slight damping of the wave are also observed here. Figure 7.22 show the temperature and differential pressure measurements between 1034 seconds and 1044 seconds since t_0, corresponding to the time at which the low-amplitude periodic wave was observed.

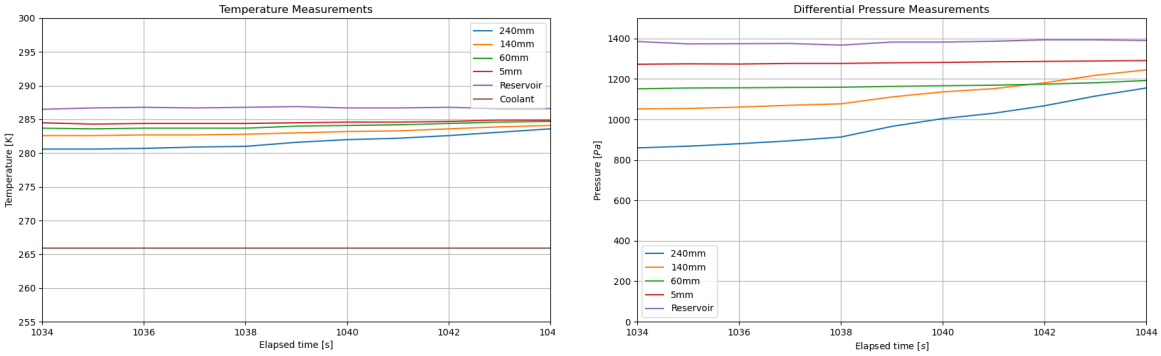

(a) Temperature measurements between 1034 seconds and 1044 seconds since t_0. Temperatures are measured at several locations along the channel, with the height from the channel inlet indicated in the plot legend.

(b) Differential pressure measurements between 1034 seconds and 1044 seconds since t_0. Pressures are measured at several locations along the channel, with the height from the channel inlet indicated in the plot legend.

Figure 7.22: Overview of temperature and differential pressure profiles for the piezoelectric sensor test between 1034 seconds and 1044 seconds since t_0.

Discussion of Possible Origins

These low-amplitude periodic wave may have two possible explanations for its source: a flock of very small particles striking the sensor, or a turbulence-induced flow oscillation. It is possible that the observed low-amplitude, noisy wave is caused by a flock or stream of very small particles impacting or interacting with the cantilever sensor, but without enough energy to generate a distinct, sharp damped waveform like the larger particles do. With smaller particles carrying less momentum compared to the larger particles traveling at the same speed, the sensor is not excited strongly enough to produce a large spike and a damping oscillation like that of Figure 7.14. Moreover, with many small particles striking the sensor in rapid succession, their individual signals may combine into a low-amplitude, noisy signal that reflects a physical interaction.

Figure 7.22a show the temperature readings of the higher locations converging towards the temperatures of the lower location. Moreover, Figure 7.22b show similar trends with measurements at higher locations increasing and converging towards the lower location measurements. The peak of convergence occurs just after the detection of the low-amplitude waves, but the gradual converging trend is already observed from before the convergence peaks off. The trend of increasing temperature may be an indication of freezing of water within the channel, as this is an exothermic process releasing heat out into the surroundings.

On the other hand, it is also plausible that an aerodynamic turbulence at the vent exit of the channel to cause the signal displayed here. When turbulent eddies form and break near the cantilever, they can cause fluctuating pressure or velocity fields, which in turn induce vibrations in the cantilever beam. These are often low-amplitude, broadband, and noisy, but may still show dominant frequencies corresponding to characteristic flow structures like vortex shedding. If a structure is not mounted rigidly and the frequency of vortex shedding matches the resonance frequency of the structure, then the structure can begin to resonate, vibrating with harmonic oscillations driven by the energy of the flow (Epifanio, 2003).

The increase in temperature and pressure may be explained with an increased clogging of the channel due to ice formation. With a partially clogged channel, less vapor leaves the plume model, making the pressure within the channel higher than it would have been without any clogging. Moreover, the temperature inside the channel would increase due to 1) the development of ice being an exothermic process and 2) clogging causing the flow speed inside the channel to decrease and therefore less acceleration that would otherwise be observed with the gradually decreasing temperature for higher locations along the channel. The clogging in the channel can consequently alter the speed of the flow exiting the channel. As a result, vortex shedding may be caused at a particular flow speed to match the resonance frequency of the sensor.

For this observed waveform, an estimate of the particle size may be derived assuming a given particle

speed. The flow speed at this time is 405 m/s, and if it is assumed that the particle speed is coupled to this speed, the particle size estimated using the drop test results is 0.201 mm in diameter. However it should be noted that because this waveform may be due to a group of multiple small particles striking the sensor, the impulse is also a collection of many particles striking the sensor. The diameter computed here is the ”bulk” size of the particles hitting the sensor at this point in time.

7.3.6. Noise Analysis

The noise detected during the tests shows an implication of the minimum detectable voltage and therefore particle size and/or speed. The signal noise in terms of maximum voltage is measured to be 29.80 mV, and 54.02 mV in terms of peak-to-peak signal. Using the slope values derived in subsection 7.2.2, the minimum detectable impulse according to maximum voltage and peak-to-peak voltage are 0.003221674 mNs and 0.002741357 mNs, respectively. Given an assumed particle velocity, Equation 7.3 can be used to determine particle mass, and Equation 7.11 can be used to determine particle size assuming a particle density ρ. For this investigation, a particle density for ice (918 kg/m^3) is used. From the preliminary plume experiments, when particle speed is assumed to be 800 m/s, the minimum detectable particle diameter is 0.1925 mm using maximum voltage value and 0.2031 mm using peak-to-peak voltage value. These sizes are larger compared to those derived in subsection 7.2.4. This is mainly due to the presence of vapor flow incident on the sensor. While this vapor flow does not cause the sensing system to be entirely unmeasurable, small variations in the flow speed cause the sensor to have a larger noise compared to the drop test, in which the flow of vapor was absent. It is a future recommendation to incorporate data processing to remove these noise from the measurement data, through an analysis and removal of the noise that the vapor flow causes.

Figure 7.23 plots the minimum detectable particle size as a function of particle velocity. This plot uses Figure 7.5 to determine the minimum impulse.

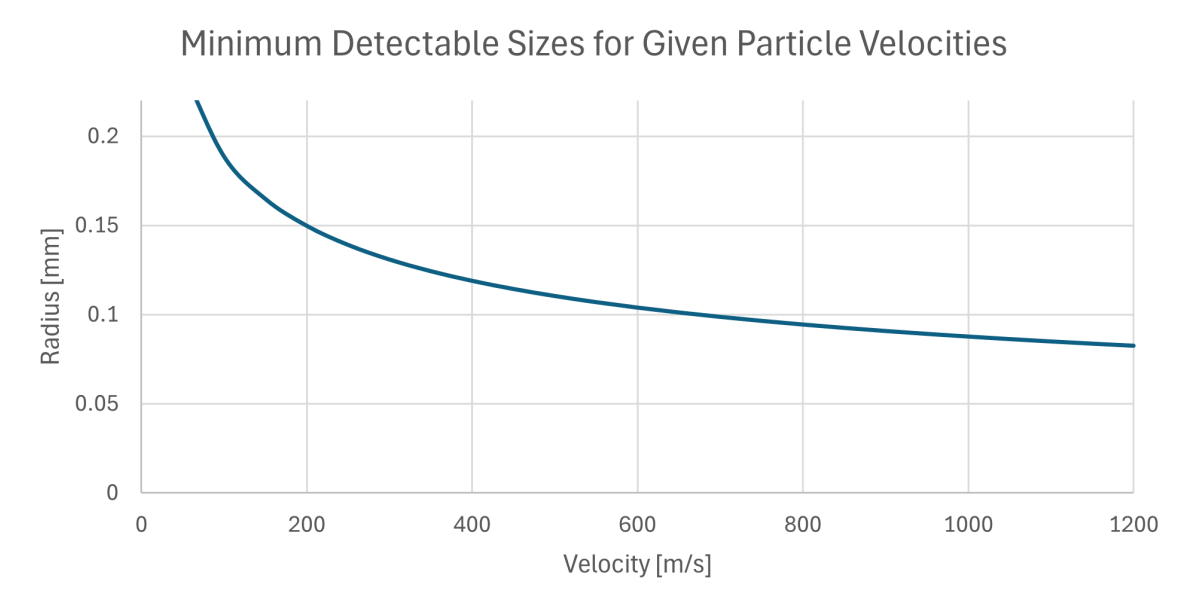

Figure 7.23: Plot showing measured peak-to-peak voltage and estimated impulse of impact particle from small and large grain tests. Mass and drop height for each test case are labeled on each average measurement point.

8

Conclusion and Recommendations

Experimental approaches have been employed to better understand the plumes of Enceladus. The past researches have mainly focused on the flow properties of the experimental plume model. Giordano, 2023 used experimental results to infer the occurrence of phase change in the plume model, suggesting a possibility of nucleation occurring in the channel. This research project addresses the solid particles within the vapor flow, and aims to detect the solid particles that are suggested to be existing in the model. The following research question was formulated.

How can the plume's ejecta from an icy moon's subsurface ocean be visualized, and what can these reveal about the origin of the plumes?

The main research question is further divided into several sub-questions.

How can Enceladus' plumes and the flow of gas and icy particles be recreated in a laboratory? The first sub-question is addressed to establish a baseline experiment in which a consistent plume with solid particles is generated. The results from the preliminary investigation, including both the experimental and simulation models, indicate several possibilities of nucleation occurring in the channel. Although no visual confirmation of the solid particles were made, saturation degree values and the solid fraction have suggested an occurrence of nucleation occurring within the plume model. A computational simulation of the same channel geometry also suggest the occurrence of nucleation within the channel, with the size of the particles estimated to be in the nanometer scale. Overall, the baseline experiment results show that conditions to generate solid particles are present in the plume model.

What is the ideal method to visualize plume ejecta from an icy moon? The second sub-question is addressed to conduct a trade-off between various methods to detect solid particles in the plume model. The concept generation of the detection solution has yielded two general detection principles: optical methods and impulse-based methods. As a result of the trade-off, an impulse-based method using piezoelectric sensor was selected to be the most appropriate technique for this application. This method is characterized by the capability to determine the size of particles based on the measured impulse of the solid particles.

What can be concluded from the grain velocities and sizes measured using the selected detection technology? The third sub-question addresses the findings from the implementation of the selected detection method. The first phase of the test campaign involved conducting a drop test to investigate the voltage response of the sensor using grains of known masses. A linear relationship between the impulse of the grain and the voltage response was identified, and this result allowed for the impulse of an incident particle to be extrapolated given a voltage response. The second phase of the test campaign integrated the detection system into the plume mode in the vacuum chamber. Several waveforms were detected throughout the experiment: damped wave, attributed to solid particles ejected from the model, turbulent wave, attributed to an unsteady flow of vapor during the initial boiling phase, and low-amplitude periodic waves, attributed to a flock of small particles ejected from the plume model. These results indicate a presence of solid particles in the plume model, and given a particle velocity,

the particle size may be determined. A noise analysis of the sensor in the plume model was performed, yielding a plot of the minimum detectable particle size to the particle velocity.

8.1. Recommendations for Future Research

Several recommendations may be suggested from the results of this research project.

Thermocouple location: the temperatures are measured at the reservoir and four locations along the channel, and the thermocouples are inserted into the channel through small holes in the plume model. The thermocouples are positioned within the channel so that the temperature at the center of the flow may be measured. This position is chosen to accurately measure the flow temperature, as the temperature of the channel wall surface deviates from the real flow temperature. According to Giordano, 2023, the adiabatic wall temperature is observed to be higher than the mean stream static temperature due to viscous dissipation. The benefit of measuring temperature along the channel centerline rather than the wall temperature is that a recovery factor to correct for this effect is not necessary, however the presence of a thermocouple in the middle of the flow gives rise to concerns regarding the extent of intrusiveness of this sensor. This effect shall be investigated in future research.

Detection of temperature and pressure along channel: as noted in section 5.3, a surge in saturation degree may be occurring at a certain location in the channel. However, since the current experiment setup collects data from only 5 points along the channel, this surge may be difficult to be identified through the current experimental model. It is a recommendation for future research to consider possible ways to collect temperature and pressure data throughout the entire length of the channel, or otherwise at increased number of locations in a non-intrusive manner.

Drop test precision: Tthe small grain test shows a steeper impulse-to-voltage slope compared to the large grain test. This suggests that the small grain tests have picked up higher voltages than it would have given the results of the large grain tests. The difference may be attributed to the precision of the grain's impact point on the sensor edge. The large grain tests involved dropping the grains from a higher point than the small grain tests. With the grains dropped from a higher drop height, the grains are more likely to miss the intended detection point on the sensor. The standard deviation values for the large grain test is 19.3 mV on average, whereas the standard deviation values for the small grain test is 3.0 on average. For a more precise measurement of the drop test, it is recommended to employ a more precise technique to drop the grains from a high drop height. This is especially important when the purpose of the drop test is to establish an empirical relationship between the impulse and the voltage.

Flow velocity measurement: it was seen in the baseline experiments that there is a difference between the flow velocities derived from Pitot probes and the differential pressure sensors near the vent. It was observed here that the velocities based on the Pitot tube were higher than the velocities based on differential pressure measurements for most of the experiment duration. With the current piezoelectric sensor setup, the Pitot probe cannot be placed over the vent of the channel. Thus, the only way to infer flow velocity with the sensor setup is to use the differential pressure sensor near the vent. As this velocity tends to be lower than the Pitot probe velocity, the minimum detectable particle size may be of lower size than the current determined size. It is a future recommendation for an Empirical relation to be derived between the Pitot probe speed and the differential pressure speed, or to develop other methods of flow velocity measurement.

Piezoelectric sensor signal processing: the comparison of noise between the drop test and the plume model test shows that the noise is larger for the plume model test, likely due to the presence of vapor flow incident on the piezoelectric sensor. While this vapor flow does not cause the sensing system to be entirely unmeasurable, small variations in the flow speed cause the sensor to have a larger noise. It is a future recommendation to incorporate a more developed signal processing method to remove these noise from the raw measurement data.

Use of impulse-based method in conjunction with velocity measurement technique: the selected impulse-based detection method using piezoelectric sensor can determine the size of the incident particles using an estimated particle velocity. For this research, it was assumed that the particle speed is coupled to the flow speed, however this assumption may not hold up, especially for grains of large size. Thus, it is recommended for future research that this detection method should be used in conjunction with

another technique to accurately measure the velocity of the solid particles, such as particle tracking velocimetry, as discussed in subsection 6.4.2.

References

Acquah, F. K. C., Takyi, J. P. K., & Beem, H. R. (2024). Design and characterization of a low-cost particle image velocimetry system. *HardwareX*, *19*, e00563. https://doi.org/10.1016/J.OHX.2024.E00563

Anderson, J. D. (2002). *Modern compressible flow: With historical perspective* (3rd ed.). McGraw-Hill Education.

Brown, R. H., Baines, K. H., Bellucci, G., Bibring, J. P., Buratti, B. J., Capaccioni, F., Cerroni, P., Clark, R. N., Coradini, A., Cruikshank, D. P., Drossart, P., Formisano, V., Jaumann, R., Langevin, Y., Matson, D. L., Mccord, T. B., Mennella, V., Miller, E., Nelson, R. M., … Sotin, C. (2005). The cassini visual and infrared mapping spectrometer (vims) investigation. https://doi.org/10.1007/s11214-004-1453-x

Brown, R. H., Clark, R. N., Buratti, B. J., Cruikshank, D. P., Barnes, J. W., Mastrapa, R. M., Bauer, J., Newman, S., Momary, T., Baines, K. H., Bellucci, G., Capaccioni, F., Cerroni, P., Combes, M., Coradini, A., Drossart, P., Formisano, V., Jaumann, R., Langavin, Y., … Sotin, C. (2006). Composition and physical properties of enceladus' surface. *Science*, *311*. https://doi.org/10.1126/science.1121031

Campell, J. K., & Anderson, J. D. (1989). Gravity field of the saturnian system from pioneer and voyager tracking data. *The Astronomical Journal*, *97*. https://doi.org/10.1086/115088

Cassini Imaging Team, N. J. P. L. (n.d.-a). *Enceladus*. Retrieved September 23, 2024, from https://photojournal.jpl.nasa.gov/catalog/PIA19061

Cassini Imaging Team, N. J. P. L. (n.d.-b). *Enceladus*. Retrieved September 23, 2024, from https://photojournal.jpl.nasa.gov/catalog/PIA07800

Cito, S. (2010). *Numerical and experimental study of flow and wall mass transfer rates in capillary driven flows in microfluidic channels* [Doctoral dissertation, Universitat Rovira I Virgili].

Connectivity, T. (2017). *Ldt1-028k piezo sensor*.

Czechowski, L. (2014). Some remarks on the early evolution of enceladus. *Planetary and Space Science*, *104*. https://doi.org/10.1016/j.pss.2014.09.010

Dougherty, M. K., Khurana, K. K., Neubauer, F. M., Russell, C. T., Saur, J., Leisner, J. S., & Burton, M. E. (2006). Identification of a dynamic atmosphere at enceladus with the cassini magnetometer. *Science*, *311*. https://doi.org/10.1126/science.1120985

Dracos, T. (1996). *Three-dimensional velocity and vorticity measuring and image analysis techniques. proceedings of a course, zurich, switzerland 1996* (T. Dracos, Ed.; Vol. 4). Springer, Dordrecht. https://doi.org/https://doi.org/10.1007/978-94-015-8727-3_7

Efroimsky, M. (2018). Tidal viscosity of enceladus. *Icarus*, *300*. https://doi.org/10.1016/j.icarus.2017.09.013

Epifanio, C. (2003). Lee vortices. *Encyclopedia of Atmospheric Sciences*, 1150–1160. https://doi.org/10.1016/B0-12-227090-8/00241-4

ESA. (2019). *Iss: Imaging science subsystem*. https://sci.esa.int/web/cassini-huygens/-/34954-instruments?fbodylongid=1618

Esposito, L. W., Barth, C. A., Colwell, J. E., Lawrence, G. M., McClintock, W. E., Stewart, A. I. F., Keller, H. U., Korth, A., Lauche, H., Festou, M. C., Lane, A. L., Hansen, C. J., Maki, J. N., West, R. A., Jahn, H., Reulke, R., Warlich, K., Shemansky, D. E., & Yung, Y. L. (2005). The cassini ultraviolet imaging spectrograph investigation. https://doi.org/10.1007/s11214-004-1455-8

Fontes, T. (2023). *Icy plumes on enceladus* [Master's thesis, Delft University of Technology]. https://repository.tudelft.nl/record/uuid:1b396d5a-71b3-44af-93d4-23a902c4c37d

Giordano, F. (2023). *Investigation of enceladus' plumes through laboratory experiments* [Master's thesis, Delft University of Technology]. https://repository.tudelft.nl/record/uuid:f9b4be47-678c-4a22-8efe-2766aa8a10c5

Hansen, C. J., Esposito, L. W., Colwell, J. E., Hendrix, A. R., Portyankina, G., Stewart, A. I., & West, R. A. (2020). The composition and structure of enceladus' plume from the complete set of cassini uvis occultation observations. *Icarus*, *344*. https://doi.org/10.1016/j.icarus.2019.113461

Harmand, S., Pellé, J., Poncet, S., & Shevchuk, I. V. (2013). Review of fluid flow and convective heat transfer within rotating disk cavities with impinging jet. *International Journal of Thermal Sciences*, *67*, 1–30. https://doi.org/10.1016/J.IJTHERMALSCI.2012.11.009

Hendrix, A. R., Hansen, C. J., & Holsclaw, G. M. (2010). The ultraviolet reflectance of enceladus: Implications for surface composition. *Icarus*, *206*. https://doi.org/10.1016/j.icarus.2009.11.007

Jennings, D. E., Flasar, F. M., Kunde, V. G., Nixon, C. A., Segura, M. E., Romani, P. N., Gorius, N., Albright, S., Brasunas, J. C., Carlson, R. C., Mamoutkine, A. A., Guandique, E., Kaelberer, M. S., Aslam, S., Achterberg, R. K., Bjoraker, G. L., Anderson, C. M., Cottini, V., Pearl, J. C., … Ferrari, C. (2017). Composite infrared spectrometer (cirs) on cassini. *Applied Optics*, *56*. https://doi.org/10.1364/ao.56.005274

Martin, E. S., Whitten, J. L., Kattenhorn, S. A., Collins, G. C., Southworth, B. S., Wiser, L. S., & Prindle, S. (2023). Measurements of regolith thicknesses on enceladus: Uncovering the record of plume activity. *Icarus*, *392*. https://doi.org/10.1016/j.icarus.2022.115369

Matson, D. L., Castillo-Rogez, J. C., Davies, A. G., & Johnson, T. V. (2012). Enceladus: A hypothesis for bringing both heat and chemicals to the surface. *Icarus*, *221*. https://doi.org/10.1016/j.icarus.2012.05.031

NASA/JPL-Caltech. (n.d.). *Pia08355: Exploring icy canyons*. Retrieved September 30, 2024, from https://photojournal.jpl.nasa.gov/catalog/PIA08355

Nimmo, F., Spencer, J. R., Pappalardo, R. T., & Mullen, M. E. (2007). Shear heating as the origin of the plumes and heat flux on enceladus. *Nature*, *447*. https://doi.org/10.1038/nature05783

Noto, D., Tasaka, Y., & Murai, Y. (2023). Low-cost 3d color particle tracking velocimetry: Application to thermal turbulence in water. *Experiments in Fluids*, *64*. https://doi.org/10.1007/s00348-023-03638-3

Owojaiye, G., & Sun, Y. (2013). Focal design issues affecting the deployment of wireless sensor networks for pipeline monitoring. *Ad Hoc Networks*, *11*, 1237–1253. https://doi.org/10.1016/J.ADHOC.2012.09.006

Peale, S. J. (1999). Origin and evolution of the natural satellites. *Annual Review of Astronomy and Astrophysics*, *37*. https://doi.org/10.1146/annurev.astro.37.1.533

Perry, M. E., Teolis, B. D., Hurley, D. M., Magee, B. A., Waite, J. H., Brockwell, T. G., Perryman, R. S., & McNutt, R. L. (2015). Cassini inms measurements of enceladus plume density. *Icarus*, *257*. https://doi.org/10.1016/j.icarus.2015.04.037

Porco, C. C., Helfenstein, P., Thomas, P. C., Ingersoll, A. P., Wisdom, J., West, R., Neukum, G., Denk, T., Wagner, R., Roatsch, T., Kieffer, S., Turtle, E., McEwen, A., Johnson, T. V., Rathbun, J., Veverka, J., Wilson, D., Perry, J., Spitale, J., … Squyres, S. (2006). Cassini observes the active south pole of enceladus. *Science*, *311*. https://doi.org/10.1126/science.1123013

Postberg, F., Clark, R. N., Hansen, C. J., Coates, A. J., Ore, C. M. D., Scipioni, F., Hedman, M. M., & Waite, J. H. (2018). Plume and surface composition of enceladus. https://doi.org/10.2458/azu_uapress_9780816537075-ch007

Postberg, F., Schmidt, J., Hillier, J., Kempf, S., & Srama, R. (2011). A salt-water reservoir as the source of a compositionally stratified plume on enceladus. *Nature*, *474*. https://doi.org/10.1038/nature10175

Robidel, R., Mouélic, S. L., Tobie, G., Massé, M., Seignovert, B., Sotin, C., & Rodriguez, S. (2020). Photometrically-corrected global infrared mosaics of enceladus: New implications for its spectral diversity and geological activity. *Icarus*, *349*. https://doi.org/10.1016/j.icarus.2020.113848

Rovira-Navarro, M., Katz, R. F., Liao, Y., van der Wal, W., & Nimmo, F. (2022). The tides of enceladus' porous core. *Journal of Geophysical Research: Planets*, *127*. https://doi.org/10.1029/2021JE007117

Schmidt, J., Brilliantov, N., Spahn, F., & Kempf, S. (2008). Slow dust in enceladus' plume from condensation and wall collisions in tiger stripe fractures. *Nature*, *451*. https://doi.org/10.1038/nature06491

Scholts, S. O. (2025). *Plumes of enceladus - understanding plume variability of enceladus by cfd experiments*.

Schubert, G., Anderson, J. D., Travis, B. J., & Palguta, J. (2007). Enceladus: Present internal structure and differentiation by early and long-term radiogenic heating. *Icarus*, *188*. https://doi.org/10.1016/j.icarus.2006.12.012

Seika Digital Image Corporation. (2017). Piv working principle diagram [[Image]].

Sheppard, S. S., Tholen, D. J., Alexandersen, M., & Trujillo, C. A. (2023). New jupiter and saturn satellites reveal new moon dynamical families. *Research Notes of the AAS*, *7*. https://doi.org/10.3847/2515-5172/acd766

Showalter, M. R., Cuzzi, J. N., & Larson, S. M. (1991). Structure and particle properties of saturn's e ring. *Icarus*, *94*, 451–473. https://doi.org/10.1016/0019-1035(91)90241-K

Sklavenitis, S. (2021). *Experimental simulation and assessment of the geysers of icy moons in the laboratory* [Master's thesis, Delft University of Technology]. https://repository.tudelft.nl/file/File_6a2603b2-aa4a-473a-9f0f-bc9a1d6f2a06?preview=1

Smith, H. T., Shappirio, M., Johnson, R. E., Reisenfeld, D., Sittler, E. C., Crary, F. J., McComas, D. J., & Young, D. T. (2008). Encelad us: A potential source of ammonia products and molecular nitrogen for saturn's magnetosphere. *Journal of Geophysical Research: Space Physics*, *113*. https://doi.org/10.1029/2008JA013352

Spencer, J. R., Pearl, J. C., Segura, M., Flasar, F. M., Mamoutkine, A., Romani, P., Buratti, B. J., Hendrix, A. R., Spilker, L. J., & Lopes, R. M. (2006). Cassini encounters enceladus: Background and the discovery of a south polar hot spot. *Science*, *311*. https://doi.org/10.1126/science.1121661

Srama, R., Ahrens, T. J., Altobelli, N., Auer, S., Bradley, J. G., Burton, M., Dikarev, V. V., Economou, T., Fechtig, H., Görlich, M., Grande, M., Graps, A., Grün, E., Havnes, O., Helfert, S., Horanyi, M., Igenbergs, E., Jessberger, E. K., Johnson, T. V., … Zook, H. A. (2004). The cassini cosmic dust analyzer. *Space Science Reviews*, *114*. https://doi.org/10.1007/s11214-004-1435-z

Stull, D. R. (1947). Vapor pressure of pure substances. organic and inorganic compounds. *Industrial & Engineering Chemistry*, *39*(4), 517–550. https://doi.org/10.1021/ie50448a022

Teolis, B. D., Perry, M. E., Magee, B. A., Westlake, J., & Waite, J. H. (2010). Detection and measurement of ice grains and gas distribution in the enceladus plume by cassini's ion neutral mass spectrometer. *Journal of Geophysical Research: Space Physics*, *115*. https://doi.org/10.1029/2009JA015192

Teolis, B. D., Perry, M. E., Hansen, C. J., Waite, J. H., Porco, C. C., Spencer, J. R., & Howett, C. J. (2017). Enceladus plume structure and time variability: Comparison of cassini observations. *Astrobiology*, *17*. https://doi.org/10.1089/ast.2017.1647

Thomas, P. C., Tajeddine, R., Tiscareno, M. S., Burns, J. A., Joseph, J., Loredo, T. J., Helfenstein, P., & Porco, C. (2016). Enceladus's measured physical libration requires a global subsurface ocean. *Icarus*, *264*. https://doi.org/10.1016/j.icarus.2015.08.037

Waite, J. H., Lewis, W. S., Kasprzak, W. T., Anicich, V. G., Block, B. P., Cravens, T. E., Fletcher, G. G., Ip, W. H., Luhmann, J. G., Mcnutt, R. L., Niemann, H. B., Parejko, J. K., Richards, J. E., Thorpe, R. L., Walter, E. M., & Yelle, R. V. (2004). The cassini ion and neutral mass spectrometer (inms) investigation. *Space Science Reviews*, *114*. https://doi.org/10.1007/s11214-004-1408-2

Waite, J. H., Lewis, W. S., Magee, B. A., Lunine, J. I., McKinnon, W. B., Glein, C. R., Mousis, O., Young, D. T., Brockwell, T., Westlake, J., Nguyen, M. J., Teolis, B. D., Niemann, H. B., McNutt, R. L., Perry, M., & Ip, W. H. (2009). Liquid water on enceladus from observations of ammonia and 40ar in the plume. *Nature*, *460*. https://doi.org/10.1038/nature08153

Yeoh, S. K., Chapman, T. A., Goldstein, D. B., Varghese, P. L., & Trafton, L. M. (2015). On understanding the physics of the enceladus south polar plume via numerical simulation. *Icarus*, *253*. https://doi.org/10.1016/j.icarus.2015.02.020

Zhang, Y., Liu, K., Xian, H., & Du, X. (2018). A review of methods for vortex identification in hydroturbines. *Renewable and Sustainable Energy Reviews*, *81*, 1269–1285. https://doi.org/10.1016/J.RSER.2017.05.058

A

Full Piezoelectric Sensor Reading

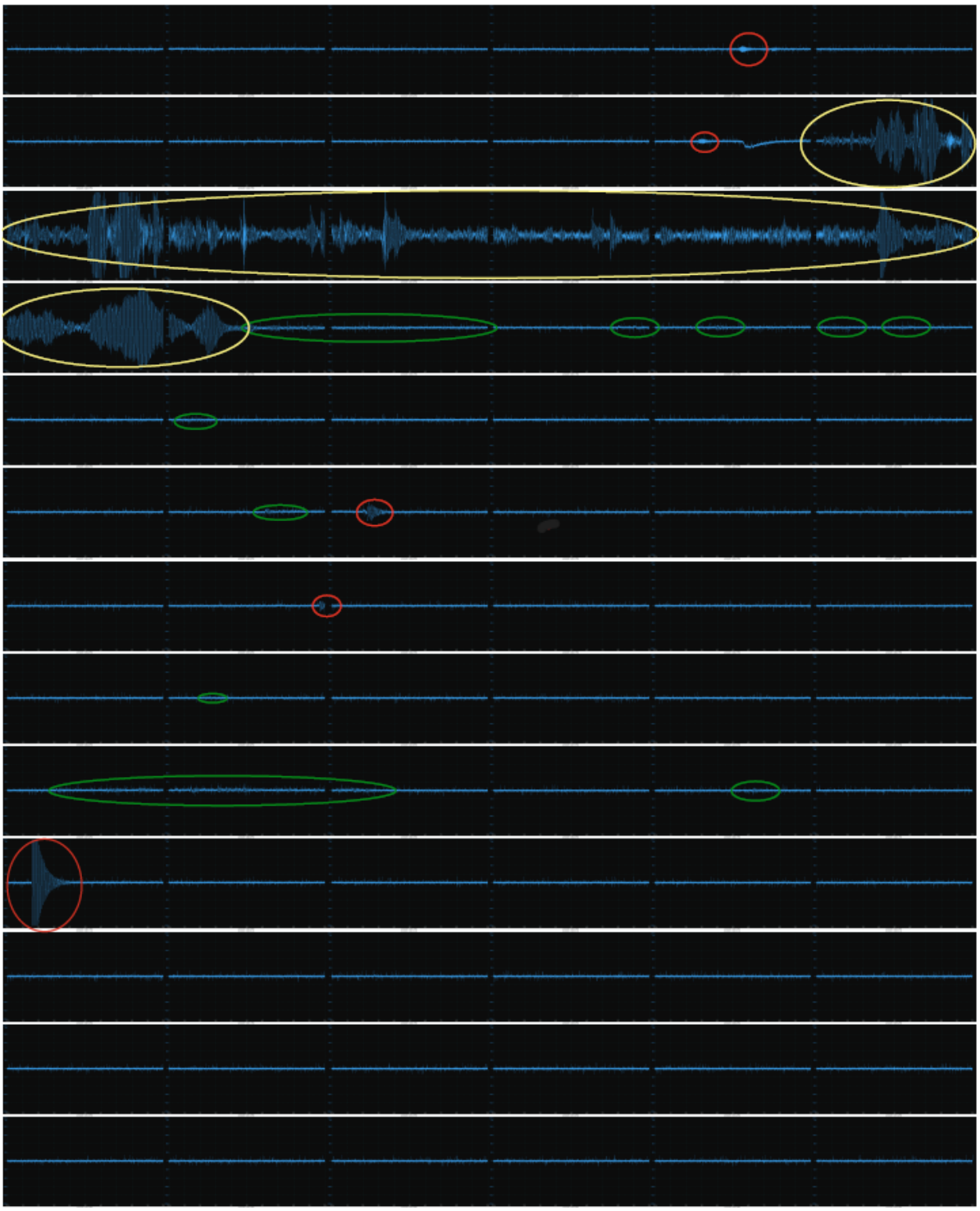

Figure A.1: Waveform generated from piezoelectric sensor reading, measured between 0 seconds and 780 seconds since t_0.

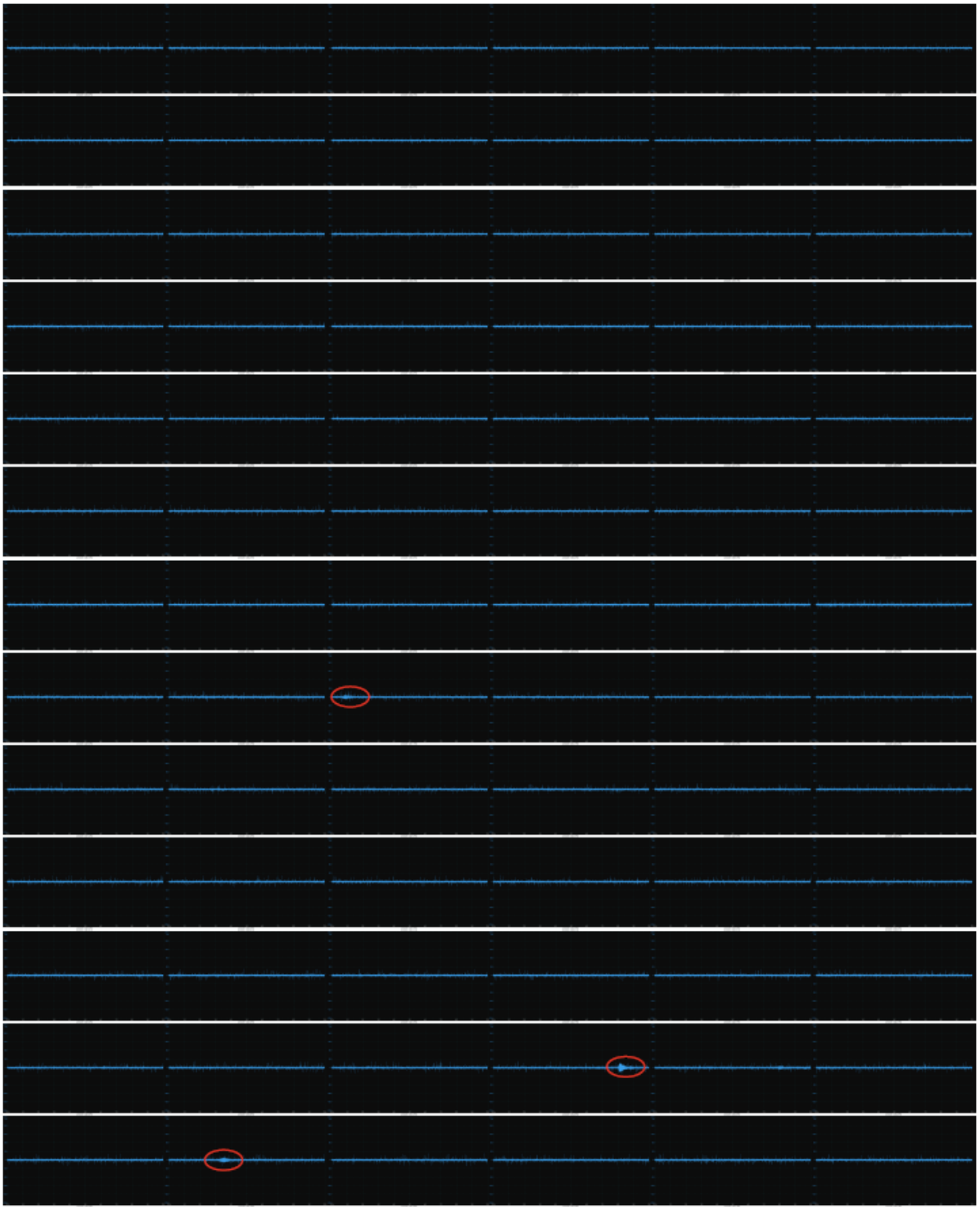

Figure A.2: Waveform generated from piezoelectric sensor reading, measured between 780 seconds and 1560 seconds since t_0.

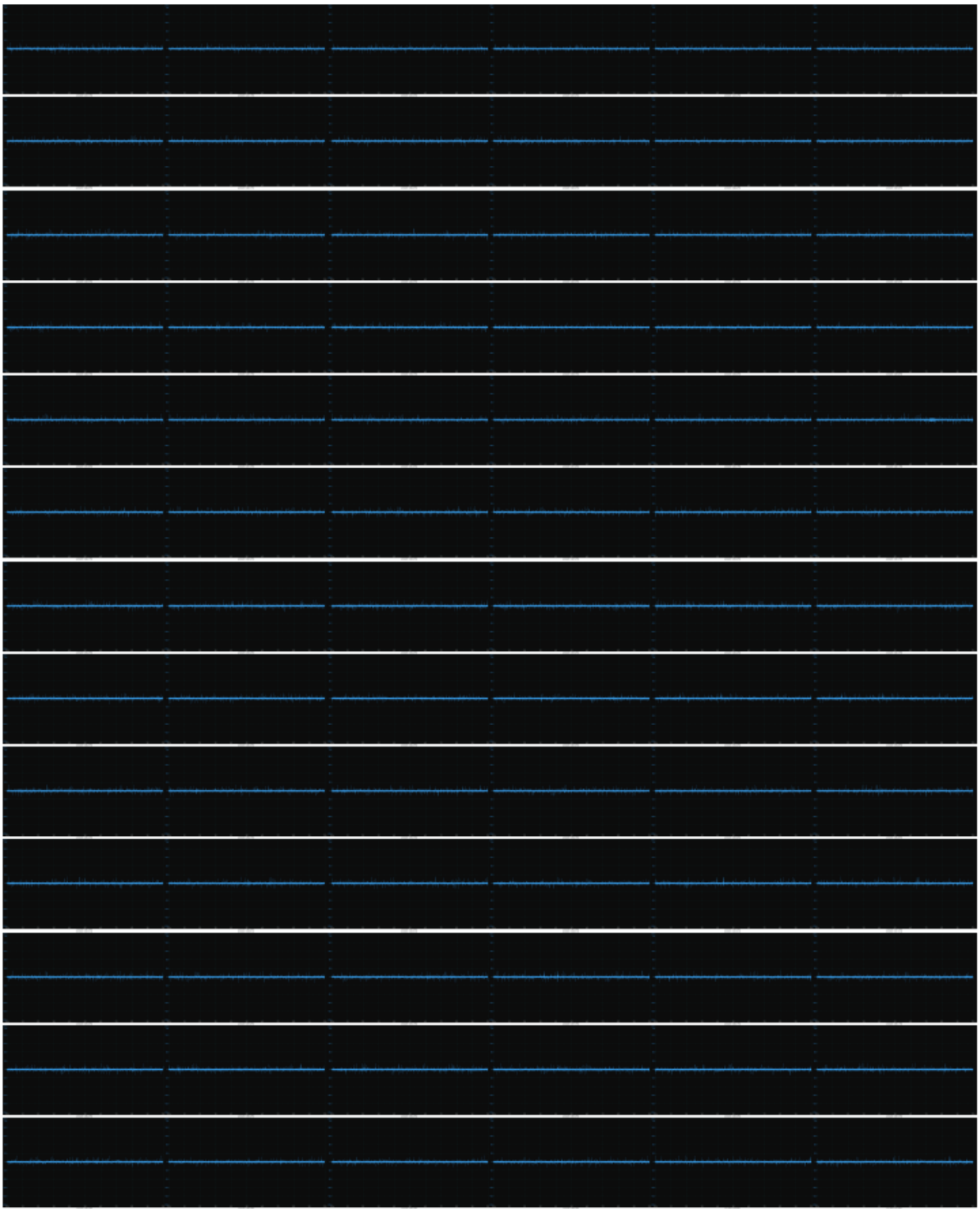

Figure A.3: Waveform generated from piezoelectric sensor reading, measured between 1560 seconds and 2340 seconds since t_0.

Figure A.4: Waveform generated from piezoelectric sensor reading, measured between 2340 seconds and 2950 seconds since t_0.